Phagocytic glia are obligatory intermediates in transmission of mutant huntingtin aggregates across neuronal synapses

Kirby M. Donnelly[1], Olivia R. DeLorenzo[2], Aprem D.A. Zaya[1], Gabrielle E. Pisano[1], Wint M. Thu[1], Liqun Luo[3,4], Ron R. Kopito[3], Margaret M. Panning Pearce[1,2,5]

[1]Department of Biological Sciences and [2]Program in Neuroscience, University of the Sciences, Philadelphia, PA 19104, USA

[3]Department of Biology, Stanford University, Stanford, CA 94305, USA

[4]Howard Hughes Medical Institute, Stanford University, Stanford, CA 94305, USA

[5]Correspondence: m.pearce@usciences.edu

ABSTRACT

Emerging evidence supports the hypothesis that pathogenic protein aggregates associated with neurodegenerative diseases spread from cell to cell through the brain in a manner akin to infectious prions. Here, we show that mutant huntingtin (mHtt) aggregates associated with Huntington disease transfer anterogradely from presynaptic to postsynaptic neurons in the adult *Drosophila* olfactory system. Trans-synaptic transmission of mHtt aggregates is inversely correlated with neuronal activity and blocked by inhibiting caspases in presynaptic neurons, implicating synaptic dysfunction and cell death in aggregate spreading. Remarkably, mHtt aggregate transmission across synapses requires the glial scavenger receptor Draper and involves a transient visit to the glial cytoplasm, indicating that phagocytic glia act as obligatory intermediates in aggregate spreading between synaptically-connected neurons. These findings expand our understanding of phagocytic glia as double-edged players in neurodegeneration—by clearing neurotoxic protein aggregates, but also providing an opportunity for prion-like seeds to evade phagolysosomal degradation and propagate further in the brain.

INTRODUCTION

Neurodegenerative diseases have emerged as one of the greatest healthcare challenges in our aging society, and thus a better understanding of the underlying pathological mechanisms is critical for development of more effective treatments or cures for these fatal disorders. A common molecular feature of many neurodegenerative diseases [e.g., Alzheimer disease (AD), frontotemporal dementias (FTD), Parkinson disease (PD), amyotrophic lateral sclerosis (ALS), and Huntington disease (HD)] is the misfolding of certain proteins, driving their accumulation into insoluble, amyloid aggregates (Knowles et al., 2014). Appearance of proteinaceous deposits in patient brains correlates closely with neuronal loss and clinical progression, and strategies to lower production or enhance clearance of pathological proteins in the degenerating brain have shown therapeutic promise in animal models and clinical trials (Boland et al., 2018; Li et al., 2019; Tabrizi et al., 2019).

Post-mortem histopathological analyses (Braak and Braak, 1991; Braak et al., 2003; Brettschneider et al., 2013) and *in vivo* imaging studies (Deng et al., 2004; Poudel et al., 2019) indicate that proteopathic lesions associated with neurodegeneration appear in highly-reproducible and disease-specific spatiotemporal patterns through the brain. Interestingly, these patterns largely follow neuroanatomical tracts (Ahmed et al., 2014; Mezias et al., 2017), suggesting a central role for synaptic connectivity in pathological aggregate spreading. Accumulating evidence supports the idea that intracellular aggregates formed by tau, α-synuclein, TDP-43, SOD1, and mutant huntingtin (mHtt) transfer from cell to cell and self-replicate by recruiting natively-folded versions of the same protein, analogous to how infectious prion protein (PrP^{Sc}) templates the conformational change of soluble PrP^{C} in prion diseases (Vaquer-Alicea and Diamond, 2019). Numerous studies have pointed to roles for endocytosis and exocytosis (Asai et al., 2015; Babcock and Ganetzky, 2015; Chen et al., 2019; Holmes et al., 2013; Lee et al., 2010; Zeineddine et al., 2015), membrane permeabilization (Chen et al., 2019; Falcon et al., 2018; Flavin et al., 2017; Zeineddine et al., 2015), tunneling nanotubes (Costanzo et al., 2013; Sharma and Subramaniam, 2019), and neuronal activity (Wu et al., 2016) in entry and/or exit of pathogenic protein assemblies from cells, but the exact mechanisms by which amyloid aggregates or

53 on-pathway intermediates cross one or more biological membranes in the highly complex central
54 nervous system (CNS) remain an enigma.

55 Glia are resident immune cells of the CNS and constantly survey the brain to maintain
56 homeostasis and respond rapidly to tissue damage or trauma. Reactive astrocytes and microglia
57 provide a first line of defense in neurodegeneration by infiltrating sites of neuronal injury, upregulating
58 immune-responsive genes, and phagocytosing dying neurons and other debris, including protein
59 aggregates (Asai et al., 2015; Grathwohl et al., 2009; Wyss-Coray et al., 2003). Prolonged activation of
60 these glial responses results in chronic inflammation, exacerbating synaptic dysfunction and neuronal
61 loss (Hammond et al., 2018). We and others have previously shown that Draper, a *Drosophila*
62 scavenger receptor that recognizes and phagocytoses cellular debris (Freeman, 2015), regulates the
63 load of mHtt (Pearce et al., 2015) and $A\beta_{1-42}$ (Ray et al., 2017) aggregate pathology in the fly CNS.
64 Remarkably, we also found that a portion of phagocytosed neuronal mHtt aggregates gain entry into
65 the glial cytoplasm and once there, nucleate the aggregation of normally-soluble wild-type Htt (wtHtt)
66 proteins, suggesting that glial phagocytosis provides a path for spreading of prion-like aggregates in
67 intact brains. Consistent with these findings, microglial ablation suppresses pathological tau
68 transmission between synaptically-connected regions of the mouse brain (Asai et al., 2015), and PrP^{Sc}
69 transfers from infected astrocytes to co-cultured neurons (Victoria et al., 2016). Thus, phagocytic glia
70 may play double-edged roles in neurodegeneration, with normally neuroprotective clearance
71 mechanisms also driving dissemination of prion-like aggregates through the brain.

72 A plethora of studies from the last decade have strengthened the prion-like hypothesis for
73 neurodegenerative diseases, but we still lack a clear understanding of how pathogenic protein
74 aggregates spread between cells in an intact CNS. In this study, we adapted our previously-described
75 *Drosophila* HD model to investigate roles for synaptic connectivity and phagocytic glia in prion-like mHtt
76 aggregate transmission in adult fly brains. HD is an autosomal dominant disorder caused by expansion
77 of a CAG repeat region in exon 1 of the Htt gene, resulting in production of highly aggregation-prone
78 mHtt proteins containing abnormally expanded polyglutamine (polyQ≥37) tracts (Bates et al., 2015;
79 MacDonald et al., 1993). By contrast, wtHtt proteins containing polyQ≤36 tracts only aggregate upon

80 nucleation by pre-formed Htt aggregate “seeds” (Chen et al., 2001; Preisinger et al., 1999). A growing
81 body of evidence from cell culture (Chen et al., 2001; Costanzo et al., 2013; Holmes et al., 2013; Ren et
82 al., 2009; Sharma and Subramaniam, 2019; Trevino et al., 2012) and *in vivo* (Ast et al., 2018; Babcock
83 and Ganetzky, 2015; Jeon et al., 2016; Masnata et al., 2019; Pearce et al., 2015; Pecho-Vrieseling et
84 al., 2014) models of HD supports the idea that pathogenic mHtt aggregates have prion-like properties—
85 they transfer from cell to cell and self-replicate by nucleating the aggregation of soluble wtHtt proteins.
86 Here, we report that mHtt aggregates formed in presynaptic olfactory receptor neuron (ORN) axons
87 effect prion-like conversion of wtHtt proteins expressed in the cytoplasm of postsynaptic partner
88 projection neurons (PNs) in the adult fly olfactory system. Remarkably, transfer of mHtt aggregates
89 from presynaptic ORNs to postsynaptic PNs was abolished in Draper-deficient animals and required
90 passage of the prion-like aggregate seeds through the cytoplasm of phagocytic glial cells. Together,
91 these findings support the conclusion that phagocytic glia are obligatory intermediates in prion-like
92 transmission of mHtt aggregates between synaptically-connected neurons *in vivo*, providing new insight
93 into key roles for glia in HD pathogenesis.

94 **RESULTS**

95 *Prion-like transfer of mHtt aggregates between synaptically-connected neurons in the adult fly olfactory*
96 *system*

97 Aggregates formed by N-terminal fragments of mHtt generated by aberrant splicing (e.g., exon
98 1; Htt_{ex1}) (Sathasivam et al., 2013) or caspase cleavage (e.g., exon 1-12; Htt_{ex1-12}) (Graham et al., 2006)
99 (Fig. 1A) accumulate in HD patient brains, are highly cytotoxic, and spread between cells in culture and
100 *in vivo* (Babcock and Ganetzky, 2015; Costanzo et al., 2013; Pearce et al., 2015; Pecho-Vrieseling et
101 al., 2014; Ren et al., 2009). We have previously established transgenic *Drosophila* that employ binary
102 expression systems [e.g., Gal4-UAS, QF-QUAS, or LexA-LexAop (Riabinina and Potter, 2016)] to
103 express fluorescent protein (FP) fusions of Htt_{ex1} in non-overlapping cell populations to monitor cell-to-
104 cell transfer of $mHtt_{ex1}$ aggregates in intact brains (Donnelly and Pearce, 2018; Pearce et al., 2015).
105 Our experimental approach (Fig. 1B) exploits the previously-reported finding that $wtHtt_{ex1}$ proteins
106 aggregate upon physically encountering $mHtt_{ex1}$ aggregate seeds (Chen et al., 2001; Preisinger et al.,
107 1999), such that transfer of $mHtt_{ex1}$ aggregates from "donor" cells is reported by conversion of
108 cytoplasmic $wtHtt_{ex1}$ from its normally soluble, diffuse state to a punctate, aggregated state in "acceptor"
109 cells (Fig. 1B-inset). To confirm that $mHtt_{ex1}$ nucleates the aggregation of $wtHtt_{ex1}$ in fly neurons, we co-
110 expressed FP-fusions of these two proteins using pan-neuronal *elav[C155]-Gal4*. In flies expressing
111 only mCherry-tagged $mHtt_{ex1}$ (Htt_{ex1}Q91-mCherry) pan-neuronally, aggregates were visible as discrete
112 mCherry+ puncta throughout adult fly brains, with enrichment in neuropil regions (Fig. 1-figure
113 supplement 1A). By contrast, GFP-tagged $wtHtt_{ex1}$ (Htt_{ex1}Q25-GFP) was expressed diffusely in the
114 same regions of age-matched adult brains (Fig. 1-figure supplement 1B). Upon co-expression with
115 Htt_{ex1}Q91-mCherry, Htt_{ex1}Q25-GFP was converted to a punctate expression pattern that almost entirely
116 overlapped with Htt_{ex1}Q91-mCherry signal (Fig. 1-figure supplement 1C and F), whereas expression
117 patterns of neither membrane-targeted GFP (mCD8-GFP) nor soluble GFP lacking a polyQ sequence
118 were affected by the presence of Htt_{ex1}Q91-mCherry aggregates in neurons (Fig. 1-figure supplement
119 1D-F). Thus, in the fly CNS, Htt_{ex1}Q91 aggregates induce prion-like conversion of normally-soluble
120 Htt_{ex1}Q25 via a homotypic nucleation reaction that requires the Htt_{ex1} sequence.

121 To examine trans-synaptic prion-like transfer of $mHtt_{ex1}$ aggregates, we coupled QF-driven
122 expression of Htt_{ex1}Q91-mCherry with Gal4-driven expression of Htt_{ex1}Q25-GFP in neuronal cell
123 populations that make well-defined synaptic connections in the adult fly olfactory system (Fig. 1B-D).
124 Htt_{ex1}Q91-mCherry was expressed using *Or67d-QF* in ~40 presynaptic ORNs ("DA1 ORNs") that
125 project axons from the antenna into the central brain, where they form synaptic connections with
126 dendrites of ~7 partner PNs ("DA1 PNs") in the DA1 glomerulus of the antennal lobe (Fig. 1B-inset, C,
127 and D) (Jefferis et al., 2001). In these same animals, Htt_{ex1}Q25-GFP was expressed in ~60% of PNs
128 using *GH146-Gal4*, which labels lateral and ventral DA1 PNs in addition to other PN types (Fig. 1C and
129 D) (Marin et al., 2002). We did not detect expression of Htt_{ex1}Q91-mCherry in DA1 ORNs until ~24 hr
130 before eclosion, consistent with activation of adult olfactory receptor gene expression during late pupal
131 development (Clyne et al., 1999), whereas Htt_{ex1}Q25-GFP was expressed in PNs via *GH146-Gal4*
132 earlier in development (Stocker et al., 1997). This genetic approach therefore enables us to monitor
133 prion-like transfer of mHtt aggregates between post-mitotic, synaptically-connected DA1 ORNs and
134 PNs in the adult fly brain.
135 Formation and prion-like transfer of $mHtt_{ex1}$ aggregates across DA1 ORN-PN synapses was
136 examined by monitoring the solubility of Htt_{ex1}Q91-mCherry and Htt_{ex1}Q25-GFP proteins in or near the
137 DA1 glomerulus (Fig. 1B-inset and E-G). Whereas Htt_{ex1}Q25-mCherry was expressed diffusely in DA1
138 ORN axons (Fig. 1C), aggregated Htt_{ex1}Q91-mCherry was visible as discrete puncta almost entirely
139 restricted to DA1 axons and axon termini in the DA1 region of the antennal lobe (Fig. 1D and E1-G1).
140 We used semi-automated 3D segmentation and reconstruction of high-magnification confocal z-stacks
141 (Fig. 1-figure supplement 2A1 and Video 1) to quantify Htt_{ex1}Q91 aggregate formation in the DA1
142 glomerulus over time. Htt_{ex1}Q91 aggregates first appeared in pharate adults and increased in number
143 as the flies aged (Fig. 1E1'-G1' and 1J). Numbers of Htt_{ex1}Q91 aggregates in males exceeded those in
144 females at each time point (Fig. 1J), consistent with known sexual dimorphism in DA1 glomerular
145 volume (Stockinger et al., 2005). In these same brains, Htt_{ex1}Q25-GFP was expressed diffusely
146 throughout GH146+ PN cell bodies and processes in young adults (Fig. 1D and E2), but bright
147 Htt_{ex1}Q25-GFP puncta began to appear and accumulate in the DA1 glomerulus as the flies aged (Fig.

148 1F2 and G2, *arrows*). Because these puncta could be difficult to distinguish from surrounding non-
149 aggregated Htt_{ex1}Q25-GFP signal, and GFP+ puncta representing normal dendritic architecture and/or
150 intracellular vesicles in the secretory pathway were visible in GH146+ PNs expressing mCD8-GFP (Fig.
151 1-figure supplement 2B2 and Fig. 1-figure supplement 3B), we defined Htt_{ex1}Q25 aggregates as GFP+
152 puncta that colocalized with Htt_{ex1}Q91 aggregates (Fig. 1-figure supplement 2A1 and C1-7, and Video
153 1). This approach reported similar results to manual quantification of the same data in 2D confocal
154 slices (Fig. 1-figure supplement 2C1-7 and D), and identical data were obtained when Htt_{ex1}Q25-GFP+
155 segmented surfaces were filtered for colocalization with Htt_{ex1}Q91-mCherry+ puncta (Fig. 1-figure
156 supplement 2A2 and D). By contrast, Htt_{ex1}Q91 aggregates in DA1 ORNs did not colocalize with
157 mCD8-GFP expressed in GH146+ PNs in control animals regardless of whether mCherry+ or GFP+
158 surfaces were initially segmented (Fig. 1-figure supplement 2B1-2). Thus, our semi-automated
159 approach to identify "Htt_{ex1}Q91+Htt_{ex1}Q25" aggregates specifically reports non-cell autonomous
160 conversion of postsynaptic wtHtt_{ex1} by presynaptic mHtt_{ex1} seeds (Fig. 1B-inset).
161 Numbers of Htt_{ex1}Q91+Htt_{ex1}Q25 aggregates increased as flies expressing Htt_{ex1}Q91-mCherry in
162 DA1 ORNs and Htt_{ex1}Q25-GFP in GH146+ PNs aged from 1 to 21 days old (Fig. 1E2'-G2' and 1J).
163 Htt_{ex1}Q91 aggregates outnumbered Htt_{ex1}Q91+Htt_{ex1}Q25 aggregates at each time point tested (Fig. 1J
164 and K), likely reflecting a higher rate of aggregate formation in "donor" ORNs expressing polyQ-
165 expanded mHtt_{ex1} than in "acceptor" PNs, where wtHtt_{ex1} proteins must be nucleated by mHtt_{ex1} seeds
166 originating in other cells. In control experiments, soluble Htt_{ex1}Q25-mCherry expressed in DA1 ORNs
167 did not colocalize with Htt_{ex1}Q25-GFP expressed in PNs (Fig. 1-figure supplement 3A, E, and F), and
168 Htt_{ex1}Q91 aggregates in DA1 ORNs did not nucleate membrane-bound mCD8-GFP in PNs (Fig. 1-
169 figure supplement 3B, E, and F). Htt_{ex1}Q91+Htt_{ex1}Q25 aggregates still formed when the Gal4 inhibitor
170 Gal80 was expressed in ORNs (Fig. 1-figure supplement 3C, E, and F) or when the QF repressor QS
171 was expressed in PNs (Fig. 1-figure supplement 3D-F), arguing strongly against co-expression of
172 Htt_{ex1}Q91-mCherry and Htt_{ex1}Q25-GFP using the highly-specific *Or67d-QF* and *GH146-Gal4* drivers.
173 Together, these findings indicate that mHtt_{ex1} aggregates formed in presynaptic ORNs induce non-cell
174 autonomous, homotypic aggregation of wtHtt_{ex1} expressed in the cytoplasm of postsynaptic PNs.

175 $Htt_{ex1}Q91$+$Htt_{ex1}Q25$ aggregates were not detected in non-synaptically-connected GH146+ PNs,
176 including in glomeruli directly adjacent to where DA1 ORNs terminate, suggesting that prion-like
177 conversion of $Htt_{ex1}Q25$ in PNs by $Htt_{ex1}Q91$ aggregates in ORNs requires synaptic connectivity. To
178 examine whether $Htt_{ex1}Q91$ aggregates can also spread retrogradely across ORN-PN synapses, we
179 expressed $Htt_{ex1}Q91$-mCherry in PNs using *GH146-QF* and $Htt_{ex1}Q25$-GFP in all ORNs using *pebbled-*
180 *Gal4*. While many $Htt_{ex1}Q91$ aggregates were visible in PN soma, dendrites, and axons in adult brains
181 (Fig. 1-figure supplement 4A-C), we did not observe colocalization of $Htt_{ex1}Q25$-GFP and $Htt_{ex1}Q91$-
182 mCherry puncta within the antennal lobe neuropil in 1, 7, and 14 day-old adults (Fig. 1-figure
183 supplement 4A, B, and D), suggesting that $Htt_{ex1}Q91$ aggregate spreading across ORN-PN synapses is
184 restricted to or much more efficient in the anterograde direction. We also found that aggregates formed
185 by $mHtt_{ex1-12}$ caspase-6 cleavage products (RFP-$Htt_{ex1-12}Q138$) (Fig. 1A) (Graham et al., 2006), which
186 have previously been shown to spread from ORN axons to more distant (non-PN) neurons in the fly
187 CNS (Babcock and Ganetzky, 2015), also transfer anterogradely across DA1 ORN-PN synapses (Fig.
188 1H and I). Together, these findings indicate that multiple pathogenic N-terminal mHtt fragments share
189 the ability to spread trans-synaptically in *Drosophila* brains, and the sequences required for prion-like
190 conversion of wtHtt reside within Htt_{ex1}.
191
192 *$wtHtt_{ex1}$ aggregates in PNs are seeded by smaller $mHtt_{ex1}$ aggregates originating in ORNs*
193 Higher magnification examination of DA1 glomeruli in flies expressing $Htt_{ex1}Q91$-mCherry (Fig.
194 2A and B) or RFP-$Htt_{ex1-12}Q138$ (Fig. 2C and D) in DA1 ORNs and $Htt_{ex1}Q25$-GFP in GH146+ PNs
195 revealed that most (>85%) $Htt_{ex1}Q25$-GFP puncta in DA1 PNs colocalized with $Htt_{ex1}Q91$-mCherry
196 aggregates. Segmentation in both the red (Fig 2A1'-D1') and green (Fig. 2A2'-D2') channels
197 demonstrated that GFP+ surfaces entirely surrounded associated mCherry+ or RFP+ surfaces in these
198 colocalized aggregates (Fig 2A3'-D3'). These data suggest that aggregated $Htt_{ex1}Q91$ or $Htt_{ex1-12}Q138$
199 proteins form the "core" of induced $Htt_{ex1}Q25$ aggregates and supports our hypothesis that $wtHtt_{ex1}$
200 solubility in PNs is altered upon direct physical interaction with pre-formed mHtt seeds. To further
201 examine molecular interactions between $Htt_{ex1}Q91$ and $Htt_{ex1}Q25$ proteins, we measured fluorescence

202 resonance energy transfer (FRET) in colocalized aggregates. Remarkably, positive FRET signal was
203 detected for all $Htt_{ex1}Q91$+$Htt_{ex1}Q25$ aggregates analyzed by this method (Fig. 2E), indicating that the
204 FP tags fused to each of these proteins were in close molecular proximity (<10 nm apart), consistent
205 with direct physical contact.

206 Comparison of volumes for all segmented $Htt_{ex1}Q91$, $Htt_{ex1-12}Q138$, $Htt_{ex1}Q91$+$Htt_{ex1}Q25$, and
207 $Htt_{ex1-12}Q138$+$Htt_{ex1}Q25$ aggregates revealed that $Htt_{ex1}Q91$ and $Htt_{ex1-12}Q138$ aggregates increased in
208 size as the flies aged, most substantially during the first week of adulthood (Fig. 2F). Interestingly, the
209 mean volume of $Htt_{ex1}Q91$ or $Htt_{ex1-12}Q138$ surfaces that colocalized with $Htt_{ex1}Q25$ aggregates (herein
210 referred to as "seeding-competent" mHtt aggregates) was less than the mean volume of all $Htt_{ex1}Q91$ or
211 $Htt_{ex1-12}Q138$ surfaces, and these differences were statistically significant in older animals. When
212 aggregate volumes were analyzed across all time points, it became apparent that seeding-competent
213 $Htt_{ex1}Q91$ or $Htt_{ex1-12}Q138$ aggregates clustered in a significantly smaller-sized subpopulation (range =
214 0.1–3.5 μm^3; mean = 1.845 $\pm$ 0.068 μm^3 for $Htt_{ex1}Q91$ aggregates, mean = 1.293 $\pm$ 0.071 μm^3 for Htt_{ex1-}
215 $_{12}Q138$ aggregates), whereas the entire population of $Htt_{ex1}Q91$ or $Htt_{ex1-12}Q138$ aggregates was more
216 heterogeneously-sized (range = 0.1–15 μm^3; mean = 2.19 $\pm$ 0.024 μm^3 for $Htt_{ex1}Q91$ aggregates, mean
217 = 2.40 $\pm$ 0.048 μm^3 for $Htt_{ex1-12}Q138$ aggregates) (Fig. 2G and H). We previously reported that
218 $Htt_{ex1}Q25$ aggregates seeded in the cytoplasm of glial cells colocalized with a similarly smaller-sized
219 subpopulation of seeding-competent $Htt_{ex1}Q91$ aggregates from DA1 ORNs (Pearce et al., 2015), and
220 smaller $mHtt_{ex1}$ aggregates are associated with increased seeding-propensity and neurotoxicity in other
221 HD models (Ast et al., 2018; Chen et al., 2001). Taken together, these findings strongly suggest that
222 $mHtt_{ex1}$ or $mHtt_{ex1-12}$ aggregates formed in presynaptic ORNs effect prion-like conversion of $wtHtt_{ex1}$ in
223 the cytoplasm of postsynaptic PNs, and that mHtt aggregate transmissibility in the fly CNS is correlated
224 with smaller aggregate size.

225

226 *$mHtt_{ex1}$ aggregate transfer is enhanced across silenced DA1 ORN-PN synapses*

227 Endocytosis, exocytosis, and neuronal activity have been previously implicated in neuron-to-
228 neuron spreading of mHtt and other pathogenic aggregates (Babcock and Ganetzky, 2015; Pecho-

229 Vrieseling et al., 2014; Wu et al., 2016), but it is not known how these processes contribute to
230 aggregate transfer across endogenous synapses *in vivo*. To examine a role for synaptic activity in DA1
231 ORN-to-PN transfer of $mHtt_{ex1}$ aggregates, we used well-established fly genetic tools that block fission
232 or fusion of synaptic vesicles at the presynaptic membrane to impair neurotransmission. First, we used
233 *shibire*^{ts1} (*shi*^{ts1}) (Kosaka and Ikeda, 1983), a temperature-sensitive mutant of the GTPase
234 Shibire/dynamin that blocks endocytic recycling of synaptic vesicles in flies raised at the restrictive
235 temperature. Co-expression of shi^{ts1} with Htt_{ex1}Q91-mCherry in DA1 ORNs in flies shifted from the
236 permissive temperature (18°C) to the restrictive temperature (31°C) in adulthood had no effect or
237 slightly decreased numbers of Htt_{ex1}Q91 aggregates in the DA1 glomerulus (Fig. 3A-C), but,
238 surprisingly, strongly enhanced formation of seeded Htt_{ex1}Q25 aggregates in DA1 PN dendrites
239 compared with control flies expressing LacZ (Fig. 3A, B, and D). Likewise, co-expression of Htt_{ex1}Q91-
240 mCherry with tetanus toxin light chain (TeTxLC), which inhibits SNARE-mediated fusion of synaptic
241 vesicles with presynaptic membranes (Sweeney et al., 1995), strongly increased numbers of seeded
242 Htt_{ex1}Q25 aggregates in the DA1 glomerulus (Fig. 3E, F, and H). At some time points, TeTxLC co-
243 expression led to increased numbers of Htt_{ex1}Q91 aggregates compared with control animals (Fig. 3E-
244 G); however, there appeared to be no correlation between numbers of Htt_{ex1}Q91 and
245 Htt_{ex1}Q91+Htt_{ex1}Q25 aggregates in the DA1 glomerulus over time, so the increased numbers of seeded
246 Htt_{ex1}Q25 aggregates were unlikely to be simply due to abundance of presynaptic Htt_{ex1}Q91 seeds. To
247 manipulate neuronal activity by an alternative approach, we co-expressed the heat-activated
248 *Drosophila* transient-receptor potential A (dTrpA) channel (Hamada et al., 2008) with Htt_{ex1}Q91-
249 mCherry to thermogenetically stimulate DA1 ORNs. In adult flies shifted from ~21°C to 31°C upon
250 eclosion, dTrpA-mediated activation of Htt_{ex1}Q91-mCherry-expressing DA1 ORNs slightly increased
251 Htt_{ex1}Q91 aggregate numbers, but decreased formation of seeded Htt_{ex1}Q25 aggregates in the DA1
252 glomerulus compared with control flies expressing LacZ (Fig. 3I-L). Together, these results indicate that
253 prion-like transmission of Htt_{ex1}Q91 aggregates from ORNs to PNs is inversely correlated with
254 presynaptic ORN activity. These findings suggest that aggregate transfer could be enhanced across

255 dysfunctional synapses, which are an early pathological finding in HD and other neurodegenerative
256 diseases.

257 Our results using shi^{ts1} and TeTxLC to block DA1 ORN activity contrast with previous reports
258 showing that spreading of Htt$_{ex1-12}$Q138 aggregates was inhibited from endocytosis- or exocytosis-
259 impaired ORNs to non-synaptically-connected neurons (Babcock and Ganetzky, 2015) or that
260 botulinum toxin inhibited spreading of mHtt$_{ex1}$ from R6/2 mouse brain slices to functionally-connected
261 human neurons (Pecho-Vrieseling et al., 2014). This discrepancy could be due to construct- or cell
262 type-specific effects or possibly different mechanisms regulating synaptic or non-synaptic aggregate
263 transmission in the brain. Thus, we wondered whether blocking Shibire-mediated endocytosis in ORNs
264 might create a more favorable environment for aggregate transfer across endogenous synapses in our
265 HD model. To test this, we first quantified Htt$_{ex1}$Q91-mCherry-expressing DA1 ORN axonal surfaces
266 using mCD8-GFP, a tool widely used to label neuronal cell bodies and processes (Lee and Luo, 1999;
267 Mosca and Luo, 2014) and to quantify neuron or neurite abundance (Burr et al., 2014; MacDonald et
268 al., 2006) in fly brains. Segmentation and 3D reconstruction of mCD8-GFP+ DA1 ORN surfaces
269 revealed that fluorescence intensity of and volume occupied by DA1 ORN axons were increased ~2-
270 fold in shi^{ts1}-expressing flies at the restrictive temperature compared with controls expressing LacZ (Fig.
271 4A-C). This effect appeared to be specific since Htt$_{ex1}$Q91 aggregate abundance in DA1 ORNs was not
272 increased by shi^{ts} co-expression (Fig. 3C), and may reflect a homeostatic compensatory response to
273 endocytic blockade (Davis, 2013; Dickman et al., 2006) that could create additional exit sites for
274 Htt$_{ex1}$Q91 aggregates.

275 To test whether inhibition of Shibire-mediated endocytosis in ORNs has similar effects on ORN-
276 to-glia transfer of Htt$_{ex1}$Q91 aggregates (Pearce et al., 2015), we co-expressed shi^{ts1} with Htt$_{ex1}$Q91-
277 mCherry in DA1 ORNs and monitored formation of seeded Htt$_{ex1}$Q25 aggregates in the glial cytoplasm.
278 Similar to effects of shi^{ts1} on trans-synaptic Htt$_{ex1}$Q91 aggregate transfer, blocking Shibire-mediate
279 endocytosis in DA1 ORNs increased seeded Htt$_{ex1}$Q25 aggregate formation in glia without affecting
280 Htt$_{ex1}$Q91 aggregate numbers (Fig. 4D-G). Together, these findings suggest that shi^{ts}-mediated
281 silencing of Htt$_{ex1}$Q91-mCherry-expressing DA1 ORNs alters axonal surface area and enhances prion-

282 like transfer of $Htt_{ex1}Q91$ aggregates from presynaptic ORN axons to the cytoplasm of both glia and
283 postsynaptic PNs.
284
285 *Glial Draper is required for ORN-to-PN transfer and alters morphology of neuronal $mHtt_{ex1}$ aggregates*
286 The parallel effects of shi^{ts1}-mediated endocytic blockade on transfer of $Htt_{ex1}Q91$ aggregates
287 from DA1 ORNs to DA1 PNs and to glia suggest that $mHtt_{ex1}$ aggregate spreading between these
288 different cell types is coordinated. Our prior work showed that ORN-to-glia transfer of $mHtt_{ex1}$
289 aggregates is strictly dependent on Draper (Pearce et al., 2015), a scavenger receptor responsible for
290 phagocytic engulfment and clearance of neuronal debris in the fly CNS and other tissues (Etchegaray
291 et al.; Han et al., 2014; Hoopfer et al., 2006; MacDonald et al., 2006). Therefore, we sought to
292 determine whether Draper-expressing phagocytic glia might play a role in transferring $mHtt_{ex1}$
293 aggregates from ORNs to PNs. To test this, we quantified numbers of $Htt_{ex1}Q91$ and seeded $Htt_{ex1}Q25$
294 aggregates in DA1 ORN axons and PN dendrites, respectively, in animals heterozygous or
295 homozygous for the *draper(drpr)*$^{\Delta 5}$ null mutation (Freeman et al., 2003). We previously reported that
296 *drpr* knockout (KO) increased steady-state numbers of $Htt_{ex1}Q91$ aggregates in DA1 ORN axons
297 (Pearce et al., 2015); however, this effect was found to not be statistically significant between *drpr*$^{\Delta 5}$
298 heterozygotes and homozygotes in this study (Fig. 5A-C). We suspect this is the case for two reasons:
299 (a) our image segmentation parameters improve identification of very small aggregates, which we show
300 are more abundant when *drpr* is expressed at normal levels (Fig. 5E-G), and (b) the $Htt_{ex1}Q91$-mCherry
301 transgene used here expresses at lower levels than the transgene used in our previous study. Thus,
302 $Htt_{ex1}Q91$ aggregates initially form more slowly in DA1 ORN axons (compare numbers of $Htt_{ex1}Q91$
303 aggregates in young females in Fig. 1J vs. Fig. 7I; the latter experiment used the same higher-
304 expressing $Htt_{ex1}Q91$-mCherry transgene as in our prior study) and may be less affected by Draper
305 depletion. Strikingly though, *drpr* KO completely blocked formation of $Htt_{ex1}Q91$+$Htt_{ex1}Q25$ aggregates
306 in postsynaptic PNs (Fig. 5A, B, and D), suggesting that Draper mediates trans-synaptic transfer of
307 $mHtt_{ex1}$ aggregates. This surprising effect of *drpr* KO on seeded $Htt_{ex1}Q25$ aggregate formation was
308 also observed when shi^{ts1} was co-expressed with $Htt_{ex1}Q91$-mCherry in ORNs (Fig. 5-figure supplement

309 1), confirming that enhanced transfer of $Htt_{ex1}Q91$ aggregates from shi^{ts1}-expressing ORNs occurs via
310 the same Draper-dependent mechanism. To rule out the possibility that *GH146-Gal4* drives expression
311 of $Htt_{ex1}Q25$-GFP in Draper+ glia, we used repo-Gal80 to inhibit Gal4 in all glia and saw no effect on
312 $Htt_{ex1}Q91$ or $Htt_{ex1}Q91$+$Htt_{ex1}Q25$ aggregate numbers (Fig. 5-figure supplement 2A, B, E, and F).
313 Moreover, expression of *drpr*-specific siRNAs in PNs did not affect formation of either $Htt_{ex1}Q91$ or
314 $Htt_{ex1}Q91$+$Htt_{ex1}Q25$ aggregates (Fig. 5-figure supplement 2C-F), consistent with glia as the sole
315 source of *drpr* expression in the fly CNS. We also did not observe significant colocalization between
316 ORN-derived $Htt_{ex1}Q91$ aggregates and GFP-fusions of Atg8a (Juhász et al., 2008) or Lamp1
317 (Pulipparacharuvil et al., 2005) in glia (Fig. 5-figure supplement 3), suggesting that neuronal $Htt_{ex1}Q91$
318 aggregates do not seed $Htt_{ex1}Q25$ in glial lysosomes or autophagosomes.
319 These results point to an unexpected but central role for glial Draper in $Htt_{ex1}Q91$ aggregate
320 transfer between multiple cell types in the fly CNS, but how phagocytic glia could mediate spreading of
321 $Htt_{ex1}Q91$ aggregates across neuronal synapses was not immediately clear. Intriguingly, mean volume
322 of $Htt_{ex1}Q91$ aggregates in DA1 ORN axons was significantly increased in *drpr* KO animals compared
323 to wild-type controls (Fig. 5E, F, and G-inset), and the relative frequency of two aggregate
324 subpopulations shifted between these genotypes: in the absence of *drpr*, the abundance of a smaller-
325 sized subpopulation (~0.1-1 μm^3) decreased while a larger-sized subpopulation (~2.5-4.0 μm^3)
326 increased in abundance (Fig. 5E-G). Intriguingly, the smaller aggregate subpopulation correlated well
327 with the size of $Htt_{ex1}Q91$ aggregates associated with converted $Htt_{ex1}Q25$ in PNs (Fig. 2G) or glia
328 (Pearce et al., 2015), suggesting that phagocytic glia could at least in part mediate formation of smaller
329 seeding-competent Htt_{ex1} aggregates. However, molecular features other than size must regulate the
330 seeding capacity of $mHtt_{ex1}$ aggregates, since smaller-sized aggregates did not completely disappear in
331 *drpr* KO animals (Fig. 5G). Taken together, these results indicate that Draper-expressing phagocytic
332 glia mediate transfer of $Htt_{ex1}Q91$ aggregates across DA1 ORN-PN synapses, perhaps in part by
333 altering morphological features of neuronal $mHtt_{ex1}$ aggregates.
334
335 *Caspase activation in ORNs is required for trans-synaptic transfer of $mHtt_{ex1}$ aggregates*

336 Phagocytic glia engulf injured or degenerating neuronal processes and apoptotic cell corpses by
337 recognizing “eat me” signals exposed on these debris (Wilton et al., 2019), and mHtt expression
338 induces caspase-dependent apoptosis in fly and mammalian models of HD (Ahmed et al., 2014). Thus,
339 we asked whether Htt_{ex1}Q91-mCherry-expressing DA1 ORNs activate pathways that could stimulate
340 Draper-dependent transfer of aggregates to DA1 PNs. In *drpr*$^{\Delta 15}$ heterozygotes, expression of Htt_{ex1}Q91-
341 GFP in all ORNs did not significantly increase cleavage of *Drosophila* caspase-1 (Dcp-1) compared to
342 flies expressing Htt_{ex1}Q25-GFP (Fig. 6A, B, and E); however, Dcp-1 cleavage was significantly
343 increased in Htt_{ex1}Q91- vs. Htt_{ex1}Q25-expressing ORNs when *drpr* was knocked out (Fig. 6C-E). These
344 data suggest that glia efficiently clear Htt_{ex1}Q91-expressing ORN axons displaying Dcp-1-dependent
345 “eat me” signals via Draper-dependent phagocytosis. In addition, co-expression of the viral effector
346 caspase inhibitor p35 (Hay et al., 1994) with Htt_{ex1}Q91-mCherry in DA1 ORNs inhibited formation of
347 Htt_{ex1}Q91+Htt_{ex1}Q25 aggregates in DA1 PNs (Fig. 6F, G, J, and K, *squares*), indicating that inhibition of
348 apoptotic caspases in presynaptic ORNs phenocopies effects of *drpr* KO on Htt_{ex1}Q91 aggregate
349 transfer from ORNs to PNs. By contrast, co-expression of p35 with Htt_{ex1}Q25-GFP in PNs did not affect
350 numbers of Htt_{ex1}Q91+Htt_{ex1}Q25 aggregates in the DA1 glomerulus (Fig. 6H-K, *circles*), suggesting that
351 caspase-dependent signaling in PNs are not required for Htt_{ex1}Q91 aggregate spreading across ORN-
352 PN synapses. Together, these results suggest that signals mediated by apoptotic caspase activation in
353 DA1 ORNs, and not DA1 PNs, promote engulfment and trans-synaptic transfer of Htt_{ex1}Q91 aggregates
354 via phagocytic glia.
355
356 *$mHtt_{ex1}$ aggregates transfer from ORNs to PNs via the glial cytoplasm*
357 The strict requirement for glial Draper in prion-like transfer of Htt_{ex1}Q91 aggregates across ORN-
358 PN synapses can be explained by two non-mutually exclusive models. In one model (Fig. 7A, *route 1*),
359 $mHtt_{ex1}$ aggregates spread from presynaptic ORNs to postsynaptic PNs via a glial cytoplasmic
360 intermediate. This model is consistent with our previous finding that phagocytosed neuronal $mHtt_{ex1}$
361 aggregates gain entry to the glial cytoplasm to effect prion-like conversion of Htt_{ex1}Q25 (Pearce et al.,
362 2015). Alternatively (Fig. 7A, *route 2*), phagocytic glia could sculpt the synaptic environment in a way

363 that promotes transfer of mHtt_{ex1} aggregates directly from ORN axons to PN dendrites. To distinguish
364 between these models, we generated transgenic flies that use three binary expression systems (i.e.,
365 QF-QUAS, Gal4-UAS, and LexA-LexAop) to independently express a uniquely-tagged Htt_{ex1} transgene
366 in each of three cell populations: Htt_{ex1}Q91-mCherry in DA1 ORNs, Htt_{ex1}Q25-3xHA in repo+ glia, and
367 Htt_{ex1}Q25-YFP in GH146+ PNs (Fig. 7A). If Htt_{ex1}Q91-mCherry aggregates formed in presynaptic ORNs
368 transfer to postsynaptic PNs via the glial cytoplasm, Htt_{ex1}Q91-mCherry aggregate seeds should
369 template the aggregation first of Htt_{ex1}Q25-3xHA in glia and then Htt_{ex1}Q25-YFP in PNs, resulting in
370 appearance of triple-labeled mCherry+/3xHA+/YFP+ puncta in the DA1 glomerulus (Fig. 7A, *route 1*). A
371 transient double-labeled mCherry+/3xHA+ aggregate subpopulation that have accessed the glial
372 cytoplasm but not yet reached PNs might also be observed in this scenario. Alternatively, if Htt_{ex1}Q91-
373 mCherry aggregates do not access the glial cytoplasm *en route* to PNs, only double-labeled
374 mCherry+/3xHA+ and mCherry+/YFP+ aggregates would appear in the DA1 glomerulus (Fig. 7A, *route*
375 *2*).

376 Brains from transgenic flies expressing these differentially-tagged Htt_{ex1} transgenes in ORNs,
377 glia, and PNs were analyzed, and expression patterns consistent with known morphologies of these cell
378 types in the antennal lobe were observed by confocal microscopy (Fig. 7B and C, and Figure 7-figure
379 supplement 1). In contrast to data in other figures, these samples required immunostaining to detect
380 expression of Htt_{ex1}Q25-3xHA and Htt_{ex1}Q25-YFP expression in glia and PNs, respectively. We found
381 that immunolabeled aggregate subtypes were not amenable to volumetric segmentation, and so we
382 instead manually quantified single-, double-, and triple-labeled Htt_{ex1} aggregates in confocal slices and
383 used line scan intensity profiling to confirm colocalization. Htt_{ex1}Q91-mCherry expression in DA1 ORNs
384 was partially diffuse and partially punctate in young (0-1 day-old) adult flies (Fig. 7B, D, E, and I), but
385 became more punctate as the flies aged (Fig. 7C, F, G, and I). mCherry+/3xHA+ puncta representing
386 Htt_{ex1}Q91 aggregates that transferred from ORNs to glia first appeared in 2 day-old adults and
387 increased in number over the next ~24 hours (Fig. 7E, F, and J, *blue bars*). Remarkably,
388 mCherry+/3xHA+/YFP+ puncta also began to appear in 2 day-old adults and increased in abundance
389 until the flies were ~4 days old (Fig. 7F, G, and J, *striped bars*). The timing of appearance of these

390 different aggregate subtypes supports our hypothesis that $Htt_{ex1}Q91$ seeds originating in DA1 ORN
391 axons transit through the glial cytoplasm before reaching the cytoplasm of DA1 PN dendrites (Fig. 7A,
392 *route 1*). mCherry+/YFP+ puncta representing aggregates that had transferred from DA1 ORNs to DA1
393 PNs without accessing the glial cytoplasm were not detected in these brains, arguing against direct
394 transfer of $Htt_{ex1}Q91$-mCherry aggregates from ORNs to PNs (Fig. 7A, *route 2*). Control animals
395 expressing $Htt_{ex1}Q25$ proteins in paired combinations of ORNs, glia, or PNs (Figure 7-figure
396 supplement 1) confirmed that $Htt_{ex1}Q25$ aggregates in glia or PNs were only detected when $Htt_{ex1}Q91$
397 was expressed in ORNs. Remarkably, when we used RNAi to specifically knockdown *drpr* in glia,
398 numbers of $Htt_{ex1}Q91$-mCherry aggregates increased (Fig. 7H and I), while mCherry+/3xHA+ and
399 mCherry+/3xHA+/YFP+ aggregates significantly decreased or were absent in 7 day-old adults (Fig. 7H
400 and J). These data confirm that glial Draper mediates $Htt_{ex1}Q91$ aggregate transmission from ORN
401 axons to glia and across ORN-PN synapses. Taken together, these findings suggest that phagocytic
402 glia act as obligatory intermediates in unidirectional prion-like spreading of $mHtt_{ex1}$ aggregates from
403 presynaptic ORNs to postsynaptic PNs in *Drosophila* brains.
404

405 **DISCUSSION**

406 The hypothesis that prion-like spreading contributes to progression of protein aggregate
407 pathology in HD and other neurodegenerative diseases is gaining considerable support, and yet we still
408 understand very little about the mechanisms that underlie cell-to-cell spreading *in vivo*, the influences of
409 cell- and tissue-specific vulnerability, and the relevance of aggregate transmission to disease
410 progression. In this study, we report that $mHtt_{ex1}$ aggregates transfer anterogradely from presynaptic
411 ORNs to postsynaptic PNs via an obligatory path through phagocytic glia in *Drosophila* brains. ORN-to-
412 PN transmission of $mHtt_{ex1}$ aggregates was enhanced by blocking endocytosis and exocytosis and
413 slowed by thermogenetically stimulating presynaptic ORNs, suggesting an inverse relationship between
414 presynaptic activity and $mHtt_{ex1}$ aggregate spreading. $mHtt_{ex1}$ aggregate transfer across synapses was
415 inhibited by blocking apoptosis in presynaptic neurons and required the Draper scavenger receptor,
416 which we have previously reported to mediate phagocytic engulfment of $mHtt_{ex1}$ aggregates from ORN
417 axons and prion-like conversion of $wtHtt_{ex1}$ in the glial cytoplasm (Pearce et al., 2015). Here, we expand
418 our understanding of the role that glia play in prion-like diseases by showing that phagocytosed
419 neuronal $mHtt_{ex1}$ aggregates transit through the cytoplasm of glia before reaching postsynaptic PNs. To
420 the best of our knowledge, these findings are the first to uncover a role for a well-conserved phagocytic
421 pathway in prion-like spreading of pathogenic aggregates between neurons *in vivo*.

422 The increased propensity of mHtt to aggregate as a result of polyQ expansion is held in check
423 by the proteostasis network, and intrinsic differences in proteostatic capacity of neuronal
424 subpopulations could underlie regional selectivity to inclusion body formation in HD brains (Margulis
425 and Finkbeiner, 2014). However, accumulating evidence that mHtt aggregates have prion-like
426 properties suggests that aggregate spreading could also contribute to this by propagating mHtt
427 pathology through networks of synaptically-connected but selectively-vulnerable neurons. We find that
428 $mHtt_{ex1}$ aggregate transmission across ORN-PN synapses occurs selectively in the anterograde
429 direction and is inversely correlated with synaptic activity. Some of the earliest changes seen in HD
430 patient brains involve loss of presynaptic cortical inputs to the striatum, where more prominent
431 pathological findings (e.g., mHtt aggregate accumulation and massive loss of medium spiny neurons)

432 appear in later stages of disease (Reiner and Deng, 2018). In addition, selective silencing of mHtt in
433 both the cortex and striatum of BACHD mice inhibited striatal degeneration and motor phenotypes to a
434 greater extent that silencing in just the striatum (Wang et al., 2014), suggesting that mHtt-induced
435 toxicity in presynaptic cortical regions could play an important role in early HD development. Thus,
436 presynaptic dysfunction may be a driving force for mHtt aggregate spreading between synaptically-
437 connected regions of the brain. While our findings do not directly address secondary consequences of
438 $mHtt_{ex1}$ aggregate spreading across synapses, we identify a novel mechanism whereby glial responses
439 to pathological changes in synapses mediate spreading of toxic aggregates between neurons. How
440 aggregate spreading via glia impacts neuronal viability and functioning at the synaptic and/or circuit
441 level are important questions for future studies.

442 Glia survey the brain to maintain homeostasis and can rapidly switch between supportive and
443 reactive states in response to perturbations in CNS microenvironments. Upon sensing neuronal insult
444 or injury, reactive microglia and astrocytes undergo dramatic morphological, metabolic, and
445 transcriptional changes and promote neuronal survival by releasing trophic factors and phagocytosing
446 debris (Hammond et al., 2018). Central roles for phagocytic glia in neurodegeneration are becoming
447 increasingly recognized as genome-wide association studies and transcriptomic analyses identify glial
448 genes associated with increased disease risk. For example, rare variants in the microglial phagocytic
449 receptor gene *TREM2* are associated with increased risk of AD, FTD, and PD, and loss of TREM2
450 function exacerbates Aβ-, tau-, and α-synuclein-associated neurotoxicity (Griciuc et al.; Guo et al.,
451 2019; Leyns et al., 2019; Zhao et al., 2018). Disruptions in key glial phagocytic functions leads to
452 accumulation of potentially toxic aggregates in the brain (Asai et al., 2015; Hong et al., 2016; Pearce et
453 al., 2015; Ray et al., 2017; Wilton et al., 2019), and administration of antibodies targeting pathological
454 Aβ, tau, or α-synuclein proteins inhibits aggregate accumulation and spreading *in vivo* (Funk et al.,
455 2015; Masliah et al., 2005; Tran et al., 2014; Yanamandra et al., 2013). However, chronically-active or
456 otherwise dysfunctional glia induce neuroinflammation and exacerbate neuronal damage. For example,
457 hyperactivate microglia excessively engulf synapses in pre-plaque AD mouse brains (Hong et al., 2016)
458 and signal for formation of neurotoxic A1 astrocytes, which accumulate in several neurodegenerative

459 diseases (Liddelow et al., 2017; Yun et al., 2018) and during aging (Clarke et al., 2018). Our findings
460 thus add new insights to recognizing glia as double-edged players in neurodegeneration and suggest
461 that rebalancing the protective and harmful effects of glial phagocytosis could be an effective new
462 therapeutic strategy.

463 We provide several lines of evidence to support a model in which glia engulf $mHtt_{ex1}$
464 aggregates, or perhaps portions of $mHtt_{ex1}$ aggregate-containing axons, from ORNs without
465 internalizing elements of PNs: (i) $mHtt_{ex1}$ aggregate transmission occurred exclusively in the
466 anterograde direction across ORN-PN synapses, (ii) neuronal $mHtt_{ex1}$ aggregates did not colocalize
467 with markers of lysosomes or autophagosomes in glia, and (iii) caspase inhibition in ORNs and not in
468 PNs inhibited aggregate transfer. Our data suggest that glia selectively target presynaptic ORNs by
469 recognizing apoptotic "eat me" signals induced by $mHtt_{ex1}$ aggregate accumulation, and this process
470 drives aggregate transfer to postsynaptic PNs. In developing mouse brains, pruned presynaptic
471 structures are engulfed by microglia largely in the absence of postsynaptic markers (Schafer et al.,
472 2012; Weinhard et al., 2018), suggesting that mammalian glia have the ability to selectively "nibble"
473 presynaptic components (a fine-tuned phagocytic process known as trogocytosis). In addition,
474 astrocytes internalize dystrophic presynaptic terminals that accumulate near amyloid plaques in
475 transgenic mouse and human AD brains (Gomez-Arboledas et al., 2018). Intriguingly, astrocytes
476 expressing the mammalian Draper homolog MEGF10 and complement-dependent microglia
477 preferentially engulf "weaker" synapses to refine neural circuits in developing and adult mouse brains
478 (Chung et al., 2013; Schafer et al., 2012), and aberrant activation of these pathways could contribute to
479 early synaptic loss in neurodegenerative disease (Hong et al., 2016). We find that cell-to-cell $mHtt_{ex1}$
480 aggregate transfer is accelerated from silenced ORN axons, suggesting that activity-impaired synapses
481 are engulfed by nearby glia, enhancing spread along the ORN-to-glia-to-PN track. Thus, while the
482 primary objective of phagocytic glia may be to eliminate toxic neuronal debris from the CNS, aberrant
483 and/or excessive activation of phagocytic pathways could paradoxically promote disease. Premature
484 elimination of live synapses could also drive network dysfunction, suggesting that attenuating glial

485 responses could be an effective early intervention to preserve neurological functions in
486 neurodegenerative disease patients (Carpanini et al., 2019).
487 The most exciting yet unexpected finding we report here is that prion-like $mHtt_{ex1}$ aggregates do
488 not directly transfer from ORNs to PNs, but instead make an obligatory detour through the phagocytic
489 glial cytoplasm. This circuitous route could explain why relatively small numbers of seeded $wtHtt_{ex1}$
490 aggregates form in glia or PNs, since seeding-competent $mHtt_{ex1}$ must escape from multiple
491 degradative systems and from the membrane-bound phagolysosomal compartment in order to access
492 cytoplasmic $wtHtt_{ex1}$. Though transfer through glia is compulsory across ORN-PN synapses, our data
493 cannot exclude the possibility that $mHtt_{ex1}$ aggregates transfer directly between neurons in other
494 regions of the brain or at later stages of disease, when neuron-glia communication and cell integrity
495 could be severely compromised. However, our findings suggest that phagocytic glia drive aggregate
496 transfer across ORN-PN synapses by altering the transmissibility of $mHtt_{ex1}$ aggregates formed in
497 presynaptic ORN axons. We previously proposed that Draper-dependent phagocytosis could provide a
498 temporary conduit for engulfed $mHtt_{ex1}$ aggregates to escape into the glial cytoplasm (Pearce et al.,
499 2015). This idea is supported by work from others showing that α-synuclein, tau, and $mHtt_{ex1}$
500 aggregates rupture cell surface or endolysosomal membranes to access the cytoplasmic compartment
501 (Chen et al., 2019; Falcon et al., 2018; Flavin et al., 2017; Ren et al., 2009; Zeineddine et al., 2015). It
502 is possible that Draper-dependent phagocytosis could modify $mHtt_{ex1}$ aggregates to increase their
503 capacity to cross biological membranes, for example by altering molecular features such as rigidity,
504 frangibility, or size. Indeed, we report here that seeding-competent $mHtt_{ex1}$ aggregates belong to a
505 smaller-sized aggregate subpopulation whose abundance is regulated by Draper, and other groups
506 have observed that the seeding propensity of $mHtt_{ex1}$ (Ast et al., 2018; Chen et al., 2001) or tau (Wu et
507 al., 2013) aggregates is strongly associated with smaller size. This raises the intriguing possibility that
508 membrane fission or fusion events that occur during dynamin-mediated engulfment or phagosome
509 maturation could directly fragment or allow for escape of partially-digested neuronal $mHtt_{ex1}$ aggregates
510 that fall below an upper size limit for entry into the cytoplasm. Indeed, aggregate fragmentation and

511 secondary nucleation events are thought to be key components of prion-like propagation in many
512 neurodegenerative diseases (Knowles et al., 2014).

513 An outstanding question raised by our study is how ORN-derived $mHtt_{ex1}$ aggregates physically
514 transfer from glia to PN cytoplasms. This could be accomplished by a number of mechanisms already
515 proposed for cell-to-cell spreading of prion-like aggregates, such as transport through extracellular
516 vesicles or tunneling nanotubes (Costanzo et al., 2013; Sharma and Subramaniam, 2019),
517 endocytosis/exocytosis (Asai et al., 2015; Babcock and Ganetzky, 2015; Chen et al., 2019; Holmes et
518 al., 2013; Lee et al., 2010; Zeineddine et al., 2015), secretion or passive release of aggregates from
519 dying cells, and direct penetration of lipid bilayers (Brundin et al., 2010; Davis et al., 2018; Vaquer-
520 Alicea and Diamond, 2019). In a mouse model of tauopathy, pathological tau is transported between
521 anatomically-connected regions of the brain via exosomes secreted by microglia (Asai et al., 2015),
522 suggesting that phagocytosed neuronal aggregates may never encounter the extracellular space during
523 transfer. It is also possible that dysfunction caused by continuous aggregate internalization, genetic
524 mutations, and/or normal aging could decrease the efficiency by which glia clear aggregates, promoting
525 their spread. In support of this, extracellular Aβ or α-synuclein fibrils accumulate inside microglia
526 (Chung et al., 1999; Frackowiak et al., 1992), and the ability of microglia to effectively degrade
527 phagocytosed material declines with age (Bliederhaeuser et al., 2016; Tremblay et al., 2012). We
528 therefore favor a mechanism by which phagocytosed aggregates resistant to degradation overwhelm
529 the glial phagolysosomal system and promote aggregate release, either through active secretion (e.g.,
530 in an act of self-preservation) or during glial cell death. While we did not observe $mHtt_{ex1}$ aggregate
531 transmission to non-partner PNs in flies up to 3 weeks old, suggesting that aggregate transfer at these
532 ages is restricted to synaptic regions ensheathed by only 1-2 glial cells (MacDonald et al., 2006; Wu et
533 al., 2017), important remaining questions are whether aggregates that have invaded the glial cytoplasm
534 can transfer to other cells in or near the DA1 glomerulus (e.g., other glia or local interneurons) or to
535 downstream neurons in the olfactory circuit.

536 In summary, our data demonstrate that phagocytic glia are active participants in the spread of
537 prion-like protein aggregates between synaptically-connected neurons *in vivo*. Since microglial

538 processes are highly motile (Hammond et al., 2018), these findings raise the intriguing possibility that
539 phagocytic glia could mediate not only trans-synaptic, but also long-range spreading of neuronal
540 aggregate pathology in the mammalian CNS. Our findings have important implications for
541 understanding complex relationships between aggregate-induced cytotoxicity and neuron-glia
542 communication in health and disease. Deciphering the mechanisms that regulate helpful vs. harmful
543 effects of phagocytic glia in the brain will help to reveal the therapeutic potential of targeting key glial
544 functions in HD and other neurodegenerative diseases.

545 **MATERIALS AND METHODS**

546 *Fly husbandry*

547 All fly stocks and crosses were raised on standard cornmeal/molasses media at 25°C, ~50%
548 relative humidity, and on a 12 hr light/12 hr dark cycle, unless otherwise noted. The following drivers
549 were used to genetically access different cell populations in the fly CNS: *elav[C155]-Gal4* (Lin and
550 Goodman, 1994), *Or67d-QF* (Liang et al., 2013), *GH146-Gal4* (Stocker et al., 1997), *GH146-QF* (Potter
551 et al., 2010), and *GH146-LexA::GAD* (Lai et al., 2008) (a kind gift from Tzumin Lee, Janelia Farms),
552 *repo-Gal4* (Sepp et al., 2001), and *Or83b-Gal4* (Kreher et al., 2005). Transgenic flies previously
553 described by our lab include *QUAS-Htt$_{ex1}$Q91-mCherry*, *QUAS-Htt$_{ex1}$Q25-mCherry*, *UAS-Htt$_{ex1}$Q91-*
554 *mCherry*, *UAS-Htt$_{ex1}$Q25-GFP*, *UAS-Htt$_{ex1}$Q25-YFP*, and *UAS-GFP* transgenes inserted at the attP3
555 (1st chromosome) and/or attP24 (2nd chromosome) ϕC31 integration sites (Pearce et al., 2015). Other
556 transgenic flies not generated in this study include: *UAS-mCD8-GFP* (BDSC #5137), *QUAS-nucLacZ*
557 lines #7 and 44 (BDSC #30006 and 30007), *QUAS-shi^{ts1}* lines #2, 5, and 7 (BDSC #30010 and 30012;
558 kind gift from C. Potter, Johns Hopkins School of Medicine), *QUAS-TeTxLC* lines #4c and 9c and
559 *QUAS-dTrpA* lines #5, 6, and 7 (kind gifts from O. Riabinina and C. Potter, Johns Hopkins), *QUAS-*
560 *mCD8-GFP* line #5J (BDSC #30002), *QUAS-p35* (a kind gift from H. Steller, Rockefeller University),
561 *UAS-LacZ* (BDSC #8529), *UAS-p35* (BDSC #5072), *QUAS-Gal80* (BDSC #51948), *UAS-QS* (BDSC
562 #30033), *repo-Gal80* (a kind gift from T. Clandinin, Stanford University), *UAS-FFLuc.VALIUM1* (BDSC
563 #35789), *UAS-GFP-Lamp1* (BDSC #42714), *UAS-Atg8a-GFP* (BDSC #52005), and *UAS-Draper^{RNAi}*
564 and *drpr$^{\Delta 5}$* mutant flies (kind gifts from M. Freeman, Vollum Institute). Genotypes for all flies used in this
565 study are listed in Table 1.

566

567 *Cloning and transgenesis*

568 pUASTattB(Htt$_{ex1}$Q25-GFP) and pUASTattB(Htt$_{ex1}$Q25-3xHA) plasmids were generated by PCR
569 amplification of tagged Htt$_{ex1}$ cDNAs from the pcDNA3 vector backbone and cloned into pUASTattB via
570 XhoI and XbaI restriction sites. cDNA for mRFP-Htt$_{ex1-12}$Q138 (a kind gift from T. Littleton, MIT) (Weiss
571 et al., 2012) was subcloned into the pQUASTattB plasmid (Riabinina et al., 2015) using EcoRI and XbaI

572 restriction sites. Htt_{ex1}Q25-YFP cDNA was amplified by PCR from the pUASTattB(Htt_{ex1}Q25-YFP)
573 plasmid (Pearce et al., 2015) and subcloned into the EcoRI site in pLOT downstream of LexA-
574 responsive LexAop DNA sequences. Plasmids were microinjected into embryos containing the attP3 X
575 chromosome (for UAS-Htt_{ex1}Q25-GFP), attP3B or attP8 X chromosome (for QUAS-mRFP-Htt_{ex1-}
576 $_{12}$Q138), or attP24 2nd chromosome (for UAS-Htt_{ex1}Q25-3xHA or LexAop-Htt_{ex1}Q25-YFP) ϕC31
577 integration sites either in-house or at BestGene, Inc (Chino Hills, CA).
578
579 *Drosophila brain dissection and sample preparation*
580 Adult fly brains were dissected, fixed, and stained and/or imaged as previously described
581 (Pearce et al., 2015). Briefly, brains were dissected in ice-cold phosphate-buffered saline containing
582 either 0.03% Triton X-100 (PBS/0.03T, when intrinsic fluorescence of FP-fusions was imaged) or 0.3%
583 Triton X-100 (PBS/0.3T, when indirect immunofluorescence was used to detect protein expression).
584 Where possible, we imaged using intrinsic GFP/YFP/mCherry fluorescence when Htt-FP fusions
585 expression levels were high enough to detect on the confocal. Dissected brains were transferred to
586 microfuge tubes containing PBS/T + 4% paraformaldehyde fixative solution on ice and then fixed in the
587 dark at room temperature (RT) for 5 min (when imaging intrinsic fluorescence) or 20 min (when using
588 immunofluorescence). For direct fluorescence imaging, brains were washed in PBS/0.03T buffer
589 several times before incubation in Slowfade Gold Antifade Mountant (Invitrogen, Carlsbad, CA) for at
590 least 1 hr at 4°C in the dark. For immunostaining, brains were washed several times in PBS/0.3T, and
591 then blocked in PBS/0.3T containing 5% normal goat serum (Lampire Biological Laboratories,
592 Pipersville, PA) for 30min at RT, followed by incubation in primary antibodies diluted in blocking solution
593 and incubation for 24-72 hr at 4°C in the dark. Brains were then washed in PBS/0.3T several times at
594 RT and incubated in secondary antibodies diluted in blocking solution for 20-24 hr at 4°C in the dark.
595 Following another set of washes in PBS/0.3T at RT, the brains were incubated in Slowfade mountant
596 for at least 16 hr at 4°C in the dark. Brains were then bridge-mounted in Slowfade mountant on glass
597 microscopy slides overlayed with #1.5 coverglass (22 x 22 mm), and edges were sealed using clear
598 nail polish.

599 Primary antibodies used in this study include rabbit anti-DsRed (1:2000; #632496; Takara Bio
600 USA, Inc., Mountain View, CA), rabbit anti-mCherry (1:500; #PA5-34974; Invitrogen, Carlsbad, CA),
601 chicken anti-GFP (1:500; #GFP-1020; Aves Labs, Tigard, OR), chicken anti-GFP (1:1000; #ab13970;
602 Abcam, Cambridge, UK), chicken anti-GFP (1:500; #A10262; Invitrogen, Carlsbad, CA), rat anti-HA
603 (1:100; clone 3F10; #11867423001; Roche, Basel, Switzerland), rabbit anti-cleaved Dcp-1 (1:100;
604 #9578S; Cell Signaling Technology, Danvers, MA), and mouse anti-Bruchpilot (1:100; clone nc82;
605 Developmental Studies Hybridoma Bank, Iowa City, IA). Secondary antibodies used include FITC-
606 conjugated donkey anti-chicken (1:200; #703-095-155; Jackson Immuno Research Labs, West Grove,
607 PA) and AlexaFluor 488, 568, or 647-conjugated goat anti-chicken, anti-mouse, anti-rabbit, or anti-rat
608 IgGs (1:250 each; Invitrogen, Carlsbad, CA).
609
610 *Image acquisition*
611 All data were collected on a Leica SP8 laser-scanning confocal system equipped with 405 nm,
612 488 nm, 561 nm, and 633 nm lasers and 40X 1.3NA or 63X 1.4NA oil objective lenses. Leica LAS X
613 software was used to establish optimal settings during each microscopy session and to collect optical z-
614 slices of whole-mounted brain samples with Nyquist sampling criteria. Optical zoom was used to further
615 magnify and establish regions of interest in each sample. For most images, confocal data were
616 collected from ~60 x 60 x 25 μm (*xyz*) stacks centered on a single DA1 glomerulus, which was located
617 using fluorescent signal from Htt_{ex1} protein expressed in DA1 ORN terminals. Exceptions to this are
618 shown in Fig. 1-figure supplement 1A-E [250 x 250 x ~60 μm (*xyz*) stacks capturing fluorescence signal
619 in the anterior central brain] and Fig. 1C-D, Fig. 1-figure supplement 4A-B, and Fig. 6A-D [~150 x 150 x
620 30 μm (*xyz*) stacks of the anterior portion of a single antennal lobe].
621
622 *Post-imaging analysis*
623 Raw confocal data were analyzed in 2D using ImageJ/FIJI (NIH, Bethesda, MD) or in 3D using
624 Imaris (Bitplane, Zürich, Switzerland), and all quantitative data were analyzed independently by two
625 researchers blinded to the experimental conditions. For semi-automated quantification of aggregates in

626 DA1 glomeruli, raw confocal data were deconvolved to reduce blur, rendered in 3D, and cropped if
627 necessary to establish the region of interest for further analysis. mHtt fluorescence was segmented in
628 3D stacks using the “Surfaces” algorithm (surface detail set to 0.25 μm and background subtraction at
629 0.75 μm), with the “split touching objects” option selected, and seed point diameter was set to 0.85 μm.
630 Background thresholding and seed point classification were adjusted manually for each image to
631 optimize segmentation of heterogeneously-sized Htt_{ex1}Q91-mCherry puncta (“aggregates”) and
632 minimize capturing of diffuse signal. These settings differed <5-10% among individual samples in the
633 same experiment. In rare cases (<5% of aggregates in each image), some larger aggregates were
634 aberrantly split or smaller aggregates in close proximity were incorrectly merged; in these cases, the
635 objects were manually unified or split using the software program. To quantify seeded $wtHtt_{ex1}$
636 aggregates, red mHtt surfaces that colocalized with Htt_{ex1}Q25-GFP were identified by applying a filter
637 for mean intensity in the green channel. Colocalizing aggregates were selected by adjusting the
638 threshold to capture discrete Htt_{ex1}Q25 puncta with high contrast compared to surrounding diffuse
639 signal. Segmentation of Htt_{ex1}Q25 fluorescence in Fig. 1-figure supplement 2, Fig. 2A-D, and Video 1
640 was carried out using the same settings described above in the green channel. To measure DA1 ORN
641 axon volume and intensity in Fig. 4A-C, mCD8-GFP fluorescence was segmented using the “Surfaces”
642 function in Imaris, with surface detail set to 0.2 μm and background subtraction at 3 μm. Detailed
643 surface measurements (e.g. volume or intensity) were calculated in Imaris, and the data were exported
644 to Excel (Microsoft Corporation, Redmond, WA) or Prism (GraphPad Software, San Diego, CA) for
645 further analysis.

646 For data shown in Fig. 7 and Fig. 7-figure supplement 1, indirect immunofluorescence was used
647 to detect Htt_{ex1}Q25-3xHA expression in glia and amplify low Htt_{ex1}Q25-YFP signal in PNs. We found
648 that semi-automated image segmentation as described above reported fewer than half of
649 immunolabeled colocalized aggregates identified by manual counting, likely because of poor antibody
650 penetration into the aggregate core and Htt_{ex1}Q25-YFP aggregates with low contrast that made these
651 data less amenable to 3D segmentation. Instead, we manually counted aggregates in these samples by
652 scanning individual z-slices and scoring discrete puncta with increased signal relative to adjacent

653 diffuse signal in one, two, or all three channels. Line scans confirmed colocalization of signals from the
654 different Htt_{ex1} proteins, as shown in Fig. 7D-H.
655
656 *FRET analysis*
657 $Htt_{ex1}Q25$+$Htt_{ex1}Q91$ colocalized aggregates were analyzed for FRET using the acceptor
658 photobleaching method as previously described (Pearce et al., 2015). Briefly, 28 individual aggregates
659 were analyzed by photobleaching the mCherry acceptor appended to $Htt_{ex1}Q91$ using a 561nm laser
660 set at 100% intensity and scanning until fluorescence was no longer detectable. Donor fluorescence
661 dequenching was measured by exciting GFP fused to $Htt_{ex1}Q25$ using a 488 nm laser set at 1%
662 intensity before and after acceptor photobleaching. mCherry fluorescence was also excited before and
663 after photobleaching with a 561 nm laser set at 1% intensity. Fluorescence emission was collected
664 between 500 and 550 nm for GFP and 610 and 700 nm for mCherry to generate before and after
665 images as shown in Fig. 2E. FRET efficiencies ($FRET_{eff}$) were calculated after background correction
666 using the equation $(GFP_{after}-GFP_{before})/(GFP_{after}) \times 100$ and represented by a pixel-by-pixel $FRET_{eff}$
667 image generated using the FRETcalc plugin (Stepensky, 2007) in FIJI/ImageJ.
668
669 *Statistical analyses*
670 All quantified data were organized and analyzed in Excel or Prism 8. Quantifications in graphical
671 form are shown as mean $\pm$ SEM, except for frequency analyses, which are displayed in histograms.
672 Results of all statistical analyses are described in each Figure Legend. Sample size (*n*) for each figure
673 is indicated in Table 1 and was selected to yield sufficient statistical power ($\geq$ 5 biological replicates
674 from $\geq$ 3 brains for each condition; a single DA1 glomerulus represents one biological replicate).
675 Multiple statistical comparisons were performed using the following tests and post-hoc corrections
676 where appropriate: Student's *t*-tests for pairwise comparisons, or one-way or two-way ANOVA followed
677 by Sidak's or Tukey's multiple comparison tests for experiments involving $\geq$3 genotypes. Results of
678 these statistical tests are shown on each graph, and symbols used to indicate statistical significance
679 are defined in the Figure Legends.

ACKNOWLEDGMENTS

The authors would like to thank K. Chao, D. Luginbuhl, V. Reed, B. Temsamrit, and M. Warkala for technical assistance, G. Panning for help with analyzing detailed aggregate measurements, T.R. Clandinin, M.R. Freeman, H. Krämer, T. Lee, J.T. Littleton, C.J. Potter, and O. Riabinina for kindly sharing reagents, and members of the Kopito, Luo, and Pearce labs for many valuable discussions. This work was supported by grants from the NIH (R01-DC005982 to L.L., R01-NS042842 to R.R.K, and R03-AG063295 to M.M.P.P.), the W.W. Smith Charitable Trusts (to M.M.P.P.), the Pittsburgh Foundation (UN2018-98318 to M.M.P.P.), and start-up funds from University of the Sciences (to M.M.P.P.).

AUTHOR CONTRIBUTIONS

K.M.D., O.R.D., A.D.A.Z., G.E.P., and W.M.T. – Investigation, Validation, Visualization, Writing – review & editing. L.L. and R.R.K. – Conceptualization, Resources, Supervision, Writing – review & editing, Funding Acquisition. M.M.P.P. – Conceptualization, Methodology, Investigation, Validation, Formal Analysis, Visualization, Writing – original draft preparation, Writing – review & editing, Resources, Supervision, Project Administration, Funding Acquisition.

DECLARATION OF INTERESTS

The authors declare no competing interests.

701 **REFERENCES**

702 Ahmed, Z., Cooper, J., Murray, T.K., Garn, K., McNaughton, E., Clarke, H., Parhizkar, S., Ward, M.A.,
703 Cavallini, A., Jackson, S.*, et al.* (2014). A novel in vivo model of tau propagation with rapid and
704 progressive neurofibrillary tangle pathology: the pattern of spread is determined by connectivity,
705 not proximity. Acta neuropathologica *127*, 667-683.

706 Asai, H., Ikezu, S., Tsunoda, S., Medalla, M., Luebke, J., Haydar, T., Wolozin, B., Butovsky, O., Kügler,
707 S., and Ikezu, T. (2015). Depletion of microglia and inhibition of exosome synthesis halt tau
708 propagation. Nature neuroscience *18*, 1584.

709 Ast, A., Buntru, A., Schindler, F., Hasenkopf, R., Schulz, A., Brusendorf, L., Klockmeier, K., Grelle, G.,
710 McMahon, B., Niederlechner, H.*, et al.* (2018). mHTT Seeding Activity: A Marker of Disease
711 Progression and Neurotoxicity in Models of Huntington's Disease. Molecular cell *71*, 675-
712 688.e676.

713 Babcock, D.T., and Ganetzky, B. (2015). Transcellular spreading of huntingtin aggregates in the
714 Drosophila brain. Proceedings of the National Academy of Sciences of the United States of
715 America *112*, E5427-5433.

716 Baron, O., Boudi, A., Dias, C., Schilling, M., Nolle, A., Vizcay-Barrena, G., Rattray, I., Jungbluth, H.,
717 Scheper, W., Fleck, R.A.*, et al.* (2017). Stall in Canonical Autophagy-Lysosome Pathways
718 Prompts Nucleophagy-Based Nuclear Breakdown in Neurodegeneration. Current biology *27*,
719 3626-3642.e3626.

720 Bates, G.P., Dorsey, R., Gusella, J.F., Hayden, M.R., Kay, C., Leavitt, B.R., Nance, M., Ross, C.A.,
721 Scahill, R.I., Wetzel, R.*, et al.* (2015). Huntington disease. Nature reviews Disease primers *1*,
722 15005.

723 Bliederhaeuser, C., Grozdanov, V., Speidel, A., Zondler, L., Ruf, W.P., Bayer, H., Kiechle, M., Feiler,
724 M.S., Freischmidt, A., Brenner, D.*, et al.* (2016). Age-dependent defects of alpha-synuclein
725 oligomer uptake in microglia and monocytes. Acta neuropathologica *131*, 379-391.

726 Boland, B., Yu, W.H., Corti, O., Mollereau, B., Henriques, A., Bezard, E., Pastores, G.M., Rubinsztein,
727 D.C., Nixon, R.A., Duchen, M.R.*, et al.* (2018). Promoting the clearance of neurotoxic proteins in
728 neurodegenerative disorders of ageing. Nature reviews Drug discovery *17*, 660-688.
729 Braak, H., and Braak, E. (1991). Neuropathological stageing of Alzheimer-related changes. Acta
730 neuropathologica *82*, 239-259.
731 Braak, H., Del Tredici, K., Rub, U., de Vos, R.A., Jansen Steur, E.N., and Braak, E. (2003). Staging of
732 brain pathology related to sporadic Parkinson's disease. Neurobiology of aging *24*, 197-211.
733 Brettschneider, J., Del Tredici, K., Toledo, J.B., Robinson, J.L., Irwin, D.J., Grossman, M., Suh, E., Van
734 Deerlin, V.M., Wood, E.M., Baek, Y.*, et al.* (2013). Stages of pTDP-43 pathology in amyotrophic
735 lateral sclerosis. Annals of neurology *74*, 20-38.
736 Brundin, P., Melki, R., and Kopito, R. (2010). Prion-like transmission of protein aggregates in
737 neurodegenerative diseases. Nature reviews Molecular cell biology *11*, 301-307.
738 Burr, A.A., Tsou, W.-L., Ristic, G., and Todi, S.V. (2014). Using Membrane-Targeted Green Fluorescent
739 Protein To Monitor Neurotoxic Protein-Dependent Degeneration of Drosophila Eyes. Journal of
740 neuroscience research *92*, 1100-1109.
741 Carpanini, S.M., Torvell, M., Morgan, B.P. (2019). Therapeutic inhibition of the complement system in
742 diseases of the central nervous system. Frontiers in Immunology *10*, 362.
743 Chen, J.J., Nathaniel, D.L., Raghavan, P., Nelson, M., Tian, R., Tse, E., Hong, J.Y., See, S.K., Mok,
744 S.A., Hein, M.Y.*, et al.* (2019). Compromised function of the ESCRT pathway promotes
745 endolysosomal escape of tau seeds and propagation of tau aggregation. The Journal of
746 biological chemistry. Pii: jbc.RA119.009432.
747 Chen, S., Berthelier, V., Yang, W., and Wetzel, R. (2001). Polyglutamine aggregation behavior in vitro
748 supports a recruitment mechanism of cytotoxicity. Journal of molecular biology *311*, 173-182.
749 Chung, H., Brazil, M.I., Soe, T.T., and Maxfield, F.R. (1999). Uptake, degradation, and release of
750 fibrillar and soluble forms of Alzheimer's amyloid beta-peptide by microglial cells. The Journal of
751 biological chemistry *274*, 32301-32308.

752 Chung, W.-S., Clarke, L.E., Wang, G.X., Stafford, B.K., Sher, A., Chakraborty, C., Joung, J., Foo, L.C.,
753 Thompson, A., Chen, C.*, et al.* (2013). Astrocytes mediate synapse elimination through
754 MEGF10 and MERTK pathways. Nature *504*, 394-400.
755 Clarke, L.E., Liddelow, S.A., Chakraborty, C., Munch, A.E., Heiman, M., and Barres, B.A. (2018).
756 Normal aging induces A1-like astrocyte reactivity. Proceedings of the National Academy of
757 Sciences of the United States of America *115*, E1896-e1905.
758 Clyne, P.J., Warr, C.G., Freeman, M.R., Lessing, D., Kim, J., and Carlson, J.R. (1999). A novel family
759 of divergent seven-transmembrane proteins: candidate odorant receptors in Drosophila. Neuron
760 *22*, 327-338.
761 Costanzo, M., Abounit, S., Marzo, L., Danckaert, A., Chamoun, Z., Roux, P., and Zurzolo, C. (2013).
762 Transfer of polyglutamine aggregates in neuronal cells occurs in tunneling nanotubes. Journal
763 of cell science *126*, 3678-3685.
764 Davis, G.W. (2013) Homeostatic signaling and the stabilization of neural function. Neuron *80*, 718-728.
765 Davis, A.A., Leyns, C.E.G., and Holtzman, D.M. (2018). Intercellular Spread of Protein Aggregates in
766 Neurodegenerative Disease. Annual review of cell and developmental biology *34*, 545-568.
767 Deng, Y.P., Albin, R.L., Penney, J.B., Young, A.B., Anderson, K.D., and Reiner, A. (2004). Differential
768 loss of striatal projection systems in Huntington's disease: a quantitative immunohistochemical
769 study. Journal of chemical neuroanatomy *27*, 143-164.
770 Dickman D.K., Lu, Z., Meinertzhagen, I.A., and Schwarz, T.L. (2006). Altered synaptic development
771 and active zone spacing in endocytosis mutants. Current biology *16*, 591-598.
772 Donnelly, K.M., and Pearce, M.M.P. (2018). Monitoring Cell-to-cell Transmission of Prion-like Protein
773 Aggregates in Drosophila Melanogaster. Journal of visualized experiments *12*, 133.
774 Etchegaray, J.I., Elguero, E.J., Tran, J.A., Sinatra, V., Feany, M.B., and McCall, K. (2016). Defective
775 Phagocytic Corpse Processing Results in Neurodegeneration and Can Be Rescued by TORC1
776 Activation. The Journal of neuroscience : the official journal of the Society for Neuroscience *36*,
777 3170-3183.

778 Falcon, B., Noad, J., McMahon, H., Randow, F., and Goedert, M. (2018). Galectin-8-mediated selective
779 autophagy protects against seeded tau aggregation. The Journal of biological chemistry *293*,
780 2438-2451.
781 Flavin, W.P., Bousset, L., Green, Z.C., Chu, Y., Skarpathiotis, S., Chaney, M.J., Kordower, J.H., Melki,
782 R., and Campbell, E.M. (2017). Endocytic vesicle rupture is a conserved mechanism of cellular
783 invasion by amyloid proteins. Acta neuropathologica *134*, 629-653.
784 Frackowiak, J., Wisniewski, H.M., Wegiel, J., Merz, G.S., Iqbal, K., and Wang, K.C. (1992).
785 Ultrastructure of the microglia that phagocytose amyloid and the microglia that produce beta-
786 amyloid fibrils. Acta neuropathologica *84*, 225-233.
787 Freeman, M.R. (2015). Drosophila Central Nervous System Glia. Cold Spring Harbor perspectives in
788 biology *7*, a020552.
789 Freeman, M.R., Delrow, J., Kim, J., Johnson, E., and Doe, C.Q. (2003). Unwrapping glial biology: Gcm
790 target genes regulating glial development, diversification, and function. Neuron *38*, 567-580.
791 Funk, K.E., Mirbaha, H., Jiang, H., Holtzman, D.M., and Diamond, M.I. (2015). Distinct Therapeutic
792 Mechanisms of Tau Antibodies: Promoting Microglial Clearance Versus Blocking Neuronal
793 Uptake. The Journal of biological chemistry *290*, 21652-21662.
794 Gomez-Arboledas, A., Davila, J.C., Sanchez-Mejias, E., Navarro, V., Nuñez-Diaz, C., Sanchez-Varo,
795 R., Sanchez-Mico, M.V., Trujillo-Estrada, L., Fernandez-Valenzuela, J.J., Vizuete, M., *et al.*
796 (2018). Phagocytic clearance of presynaptic dystrophies by reactive astrocytes in Alzheimer's
797 disease. Glia *66*, 637-653.
798 Graham, R.K., Deng, Y., Slow, E.J., Haigh, B., Bissada, N., Lu, G., Pearson, J., Shehadeh, J., Bertram,
799 L., Murphy, Z.*, et al.* (2006). Cleavage at the caspase-6 site is required for neuronal dysfunction
800 and degeneration due to mutant huntingtin. Cell *125*, 1179-1191.
801 Grathwohl, S.A., Kalin, R.E., Bolmont, T., Prokop, S., Winkelmann, G., Kaeser, S.A., Odenthal, J.,
802 Radde, R., Eldh, T., Gandy, S.*, et al.* (2009). Formation and maintenance of Alzheimer's
803 disease beta-amyloid plaques in the absence of microglia. Nature neuroscience *12*, 1361-1363.

804 Griciuc, A., Patel, S., Federico, A.N., Choi, S.H., Innes, B.J., Oram, M.K., Cereghetti, G., McGinty, D.,
805 Anselmo, A., Sadreyev, R.I.*, et al.* (2019). TREM2 Acts Downstream of CD33 in Modulating
806 Microglial Pathology in Alzheimer's Disease. Neuron *103*, 820-835.e827.
807 Guo, Y., Wei, X., Yan, H., Qin, Y., Yan, S., Liu, J., Zhao, Y., Jiang, F., and Lou, H. (2019). TREM2
808 deficiency aggravates alpha-synuclein-induced neurodegeneration and neuroinflammation in
809 Parkinson's disease models. FASEB journal *33*, 12164-12174.
810 Hamada, F.N., Rosenzweig, M., Kang, K., Pulver, S.R., Ghezzi, A., Jegla, T.J., and Garrity, P.A.
811 (2008). An internal thermal sensor controlling temperature preference in Drosophila. Nature
812 *454*, 217-220.
813 Hammond, T.R., Robinton, D., and Stevens, B. (2018). Microglia and the Brain: Complementary
814 Partners in Development and Disease. Annual review of cell and developmental biology *34*,
815 523-544.
816 Han, C., Song, Y., Xiao, H., Wang, D., Franc, N.C., Jan, L.Y., and Jan, Y.N. (2014). Epidermal cells are
817 the primary phagocytes in the fragmentation and clearance of degenerating dendrites in
818 Drosophila. Neuron *81*, 544-560.
819 Hay, B.A., Wolff, T., and Rubin, G.M. (1994). Expression of baculovirus P35 prevents cell death in
820 Drosophila. Development *120*, 2121-2129.
821 Holmes, B.B., DeVos, S.L., Kfoury, N., Li, M., Jacks, R., Yanamandra, K., Ouidja, M.O., Brodsky, F.M.,
822 Marasa, J., Bagchi, D.P.*, et al.* (2013). Heparan sulfate proteoglycans mediate internalization
823 and propagation of specific proteopathic seeds. Proceedings of the National Academy of
824 Sciences of the United States of America *110*, E3138-3147.
825 Hong, S., Beja-Glasser, V.F., Nfonoyim, B.M., Frouin, A., Li, S., Ramakrishnan, S., Merry, K.M., Shi,
826 Q., Rosenthal, A., Barres, B.A.*, et al.* (2016). Complement and microglia mediate early synapse
827 loss in Alzheimer mouse models. Science *352*, 712-716.
828 Hoopfer, E.D., McLaughlin, T., Watts, R.J., Schuldiner, O., O'Leary, D.D., and Luo, L. (2006). Wlds
829 protection distinguishes axon degeneration following injury from naturally occurring
830 developmental pruning. Neuron *50*, 883-895.

831 Jefferis, G.S., Marin, E.C., Stocker, R.F., and Luo, L. (2001). Target neuron prespecification in the
832 olfactory map of Drosophila. Nature *414*, 204-208.
833 Jeon, I., Cicchetti, F., Cisbani, G., Lee, S., Li, E., Bae, J., Lee, N., Li, L., Im, W., Kim, M.*, et al.* (2016).
834 Human-to-mouse prion-like propagation of mutant huntingtin protein. Acta neuropathologica
835 *132*, 577-592.
836 Juhász, G., Hill, J.H., Yan, Y., Sass, M., Baehrecke, E.H., Backer, J.M., and Neufeld, T.P. (2008). The
837 class III PI(3)K Vps34 promotes autophagy and endocytosis but not TOR signaling in
838 Drosophila. The Journal of cell biology *181*, 655-666.
839 Knowles, T.P., Vendruscolo, M., and Dobson, C.M. (2014). The amyloid state and its association with
840 protein misfolding diseases. Nature reviews Molecular cell biology *15*, 384-396.
841 Kosaka, T., and Ikeda, K. (1983). Possible temperature-dependent blockage of synaptic vesicle
842 recycling induced by a single gene mutation in Drosophila. Journal of neurobiology *14*, 207-225.
843 Kreher, S.A., Kwon, J.Y., and Carlson, J.R. (2005). The molecular basis of odor coding in the
844 Drosophila larva. Neuron *46*, 445-456.
845 Lai, S.-L., Awasaki, T., Ito, K., and Lee, T. (2008). Clonal analysis of Drosophila antennal
846 lobe neurons: diverse neuronal architectures in the lateral neuroblast lineage. Development
847 *135*, 2883-2893.
848 Lee, H.-J., Suk, J.-E., Patrick, C., Bae, E.-J., Cho, J.-H., Rho, S., Hwang, D., Masliah, E., and Lee, S.-J.
849 (2010). Direct Transfer of α-Synuclein from Neuron to Astroglia Causes Inflammatory
850 Responses in Synucleinopathies. Journal of Biological Chemistry *285*, 9262-9272.
851 Lee, T., and Luo, L. (1999). Mosaic analysis with a repressible cell marker for studies of gene function
852 in neuronal morphogenesis. Neuron *22*, 451-461.
853 Leyns, C.E.G., Gratuze, M., Narasimhan, S., Jain, N., Koscal, L.J., Jiang, H., Manis, M., Colonna, M.,
854 Lee, V.M.Y., Ulrich, J.D.*, et al.* (2019). TREM2 function impedes tau seeding in neuritic plaques.
855 Nature neuroscience *22*, 1217-1222.

856 Li, Z., Wang, C., Wang, Z., Zhu, C., Li, J., Sha, T., Ma, L., Gao, C., Yang, Y., Sun, Y.*, et al.* (2019).
857 Allele-selective lowering of mutant HTT protein by HTT–LC3 linker compounds. Nature *575*,
858 203-209.
859 Liang, L., Li, Y., Potter, C.J., Yizhar, O., Deisseroth, K., Tsien, R.W., and Luo, L. (2013). GABAergic
860 projection neurons route selective olfactory inputs to specific higher-order neurons. Neuron *79*,
861 917-931.
862 Liddelow, S.A., Guttenplan, K.A., Clarke, L.E., Bennett, F.C., Bohlen, C.J., Schirmer, L., Bennett, M.L.,
863 Munch, A.E., Chung, W.S., Peterson, T.C.*, et al.* (2017). Neurotoxic reactive astrocytes are
864 induced by activated microglia. Nature *541*, 481-487.
865 Lin, D.M., and Goodman, C.S. (1994). Ectopic and increased expression of Fasciclin II alters
866 motoneuron growth cone guidance. Neuron *13*, 507-523.
867 MacDonald, J.M., Beach, M.G., Porpiglia, E., Sheehan, A.E., Watts, R.J., and Freeman, M.R. (2006).
868 The Drosophila cell corpse engulfment receptor Draper mediates glial clearance of severed
869 axons. Neuron *50*, 869-881.
870 MacDonald, M.E., Ambrose, C.M., Duyao, M.P., Myers, R.H., Lin, C., Srinidhi, L., Barnes, G., Taylor,
871 S.A., James, M., Groot, N.*, et al.* (1993). A novel gene containing a trinucleotide repeat that is
872 expanded and unstable on Huntington's disease chromosomes. Cell *72*, 971-983.
873 Margulis, J. and Finkbeiner, S. (2014). Proteostasis in striatal cells and selective neurodegeneration in
874 Huntington’s disease. Frontiers in Cellular Neuroscience *8*, 218.
875 Marin, E.C., Jefferis, G.S., Komiyama, T., Zhu, H., and Luo, L. (2002). Representation of the glomerular
876 olfactory map in the Drosophila brain. Cell *109*, 243-255.
877 Masliah, E., Rockenstein, E., Adame, A., Alford, M., Crews, L., Hashimoto, M., Seubert, P., Lee, M.,
878 Goldstein, J., Chilcote, T.*, et al.* (2005). Effects of alpha-synuclein immunization in a mouse
879 model of Parkinson's disease. Neuron *46*, 857-868.
880 Masnata, M., Sciacca, G., Maxan, A., Bousset, L., Denis, H.L., Lauruol, F., David, L., Saint-Pierre, M.,
881 Kordower, J.H., Melki, R.*, et al.* (2019). Demonstration of prion-like properties of mutant
882 huntingtin fibrils in both in vitro and in vivo paradigms. Acta neuropathologica *137*, 981-1001.

883 Mezias, C., LoCastro, E., Xia, C., and Raj, A. (2017). Connectivity, not region-intrinsic properties,
884 predicts regional vulnerability to progressive tau pathology in mouse models of disease. Acta
885 neuropathologica communications *5*, 61.
886 Mosca, T.J., and Luo, L. (2014). Synaptic organization of the Drosophila antennal lobe and its
887 regulation by the Teneurins. Elife *3*, e03726.
888 Pearce, M.M., Spartz, E.J., Hong, W., Luo, L., and Kopito, R.R. (2015). Prion-like transmission of
889 neuronal huntingtin aggregates to phagocytic glia in the Drosophila brain. Nature
890 communications *6*, 6768.
891 Pecho-Vrieseling, E., Rieker, C., Fuchs, S., Bleckmann, D., Esposito, M.S., Botta, P., Goldstein, C.,
892 Bernhard, M., Galimberti, I., Muller, M.*, et al.* (2014). Transneuronal propagation of mutant
893 huntingtin contributes to non-cell autonomous pathology in neurons. Nature neuroscience *17*,
894 1064-1072.
895 Potter, C.J., Tasic, B., Russler, E.V., Liang, L., and Luo, L. (2010). The Q system: a repressible binary
896 system for transgene expression, lineage tracing, and mosaic analysis. Cell *141*, 536-548.
897 Poudel, G.R., Harding, I.H., Egan, G.F., and Georgiou-Karistianis, N. (2019). Network spread
898 determines severity of degeneration and disconnection in Huntington's disease. Human brain
899 mapping *40*, 4192-4201.
900 Preisinger, E., Jordan, B.M., Kazantsev, A., and Housman, D. (1999). Evidence for a recruitment and
901 sequestration mechanism in Huntington's disease. Philosophical transactions of the Royal
902 Society of London Series B, Biological sciences *354*, 1029-1034.
903 Pulipparacharuvil, S., Akbar, M.A., Ray, S., Sevrioukov, E.A., Haberman, A.S., Rohrer, J., and Krämer,
904 H. (2005). Drosophila Vps16A is required for trafficking to lysosomes and
905 biogenesis of pigment granules. Journal of cell science *118*, 3663-3673.
906 Ray, A., Speese, S.D., and Logan, M.A. (2017). Glial Draper Rescues Abeta Toxicity in a Drosophila
907 Model of Alzheimer's Disease. The Journal of neuroscience : the official journal of the Society
908 for Neuroscience *37*, 11881-11893.

909 Reiner, A., and Deng, Y.P. (2018). Disrupted striatal neuron inputs and outputs in Huntington's disease.
910 CNS neuroscience & therapeutics *24*, 250-280.
911 Ren, P.H., Lauckner, J.E., Kachirskaia, I., Heuser, J.E., Melki, R., and Kopito, R.R. (2009). Cytoplasmic
912 penetration and persistent infection of mammalian cells by polyglutamine aggregates. Nature
913 cell biology *11*, 219-225.
914 Riabinina, O., Luginbuhl, D., Marr, E., Liu, S., Wu, M.N., Luo, L., and Potter, C.J. (2015). Improved and
915 expanded Q-system reagents for genetic manipulations. Nature methods *12*, 219-222.
916 Riabinina, O., and Potter, C.J. (2016). The Q-System: A Versatile Expression System for Drosophila.
917 Methods in molecular biology *1478*, 53-78.
918 Sathasivam, K., Neueder, A., Gipson, T.A., Landles, C., Benjamin, A.C., Bondulich, M.K., Smith, D.L.,
919 Faull, R.L., Roos, R.A., Howland, D.*, et al.* (2013). Aberrant splicing of HTT generates the
920 pathogenic exon 1 protein in Huntington disease. Proceedings of the National Academy of
921 Sciences of the United States of America *110*, 2366-2370.
922 Schafer, D.P., Lehrman, E.K., Kautzman, A.G., Koyama, R., Mardinly, A.R., Yamasaki, R., Ransohoff,
923 R.M., Greenberg, M.E., Barres, B.A., and Stevens, B. (2012). Microglia sculpt postnatal neural
924 circuits in an activity and complement-dependent manner. Neuron *74*, 691-705.
925 Sepp, K.J., Schulte, J., and Auld, V.J. (2001). Peripheral glia direct axon guidance across the
926 CNS/PNS transition zone. Developmental biology *238*, 47-63.
927 Sharma, M., and Subramaniam, S. (2019). Rhes travels from cell to cell and transports Huntington
928 disease protein via TNT-like protrusion. The Journal of cell biology *218*, 1972-1993.
929 Stepensky, D. (2007). FRETcalc plugin for calculation of FRET in non-continuous intracellular
930 compartments. Biochemical and biophysical research communications *359*, 752-758.
931 Stocker, R.F., Heimbeck, G., Gendre, N., and de Belle, J.S. (1997). Neuroblast ablation in Drosophila
932 P[GAL4] lines reveals origins of olfactory interneurons. Journal of neurobiology *32*, 443-456.
933 Stockinger, P., Kvitsiani, D., Rotkopf, S., Tirian, L., and Dickson, B.J. (2005). Neural circuitry that
934 governs Drosophila male courtship behavior. Cell *121*, 795-807.

935 Sweeney, S.T., Broadie, K., Keane, J., Niemann, H., and O'Kane, C.J. (1995). Targeted expression of
936 tetanus toxin light chain in Drosophila specifically eliminates synaptic transmission and causes
937 behavioral defects. Neuron *14*, 341-351.
938 Tabrizi, S.J., Leavitt, B.R., Landwehrmeyer, G.B., Wild, E.J., Saft, C., Barker, R.A., Blair, N.F.,
939 Craufurd, D., Priller, J., Rickards, H.*, et al.* (2019). Targeting Huntingtin Expression in Patients
940 with Huntington's Disease. The New England journal of medicine *380*, 2307-2316.
941 Tran, H.T., Chung, C.H., Iba, M., Zhang, B., Trojanowski, J.Q., Luk, K.C., and Lee, V.M. (2014). Alpha-
942 synuclein immunotherapy blocks uptake and templated propagation of misfolded alpha-
943 synuclein and neurodegeneration. Cell reports *7*, 2054-2065.
944 Tremblay, M.E., Zettel, M.L., Ison, J.R., Allen, P.D., and Majewska, A.K. (2012). Effects of aging and
945 sensory loss on glial cells in mouse visual and auditory cortices. Glia *60*, 541-558.
946 Trevino, R.S., Lauckner, J.E., Sourigues, Y., Pearce, M.M., Bousset, L., Melki, R., and Kopito, R.R.
947 (2012). Fibrillar structure and charge determine the interaction of polyglutamine protein
948 aggregates with the cell surface. The Journal of biological chemistry *287*, 29722-29728.
949 Vaquer-Alicea, J., and Diamond, M.I. (2019). Propagation of Protein Aggregation in Neurodegenerative
950 Diseases. Annual review of biochemistry *88*, 785-810.
951 Victoria, G.S., Arkhipenko, A., Zhu, S., Syan, S., and Zurzolo, C. (2016). Astrocyte-to-neuron
952 intercellular prion transfer is mediated by cell-cell contact. Scientific reports *6*, 20762.
953 Wang, N., Gray, M., Lu, X.-H., Cantle, J.P., Holley, S.M., Greiner, E., Gu, X., Shirasaki, D., Cepeda, C.,
954 Li, Y.*, et al.* (2014). Neuronal targets for reducing mutant huntingtin expression to ameliorate
955 disease in a mouse model of Huntington's disease. Nature medicine *20*, 536-541.
956 Weinhard, L., di Bartolomei, G., Bolasco, G., Machado, P., Schieber, N.L., Neniskyte, U., Exiga, M.,
957 Vadisiute, A., Raggioli, A., Schertel, A.*, et al.* (2018). Microglia remodel synapses by
958 presynaptic trogocytosis and spine head filopodia induction. Nature communications *9*, 1228.
959 Weiss, K.R., Kimura, Y., Lee, W.C., and Littleton, J.T. (2012). Huntingtin aggregation kinetics and their
960 pathological role in a Drosophila Huntington's disease model. Genetics *190*, 581-600.

961 Wilton, D.K., Dissing-Olesen, L., and Stevens, B. (2019). Neuron-Glia Signaling in Synapse Elimination.
962 Annual review of neuroscience *42*, 107-127.
963 Wu, J.W., Herman, M., Liu, L., Simoes, S., Acker, C.M., Figueroa, H., Steinberg, J.I., Margittai, M.,
964 Kayed, R., Zurzolo, C., Di Paolo, G., and Duff, K.E. (2013). Small misfolded tau species are
965 internalized via bulk endocytosis and anterogradely and retrogradely transported in neurons.
966 Journal of biological chemistry *288*, 1856-1870.
967 Wu, J.W., Hussaini, S.A., Bastille, I.M., Rodriguez, G.A., Mrejeru, A., Rilett, K., Sanders, D.W., Cook,
968 C., Fu, H., Boonen, R.A.*, et al.* (2016). Neuronal activity enhances tau propagation and tau
969 pathology in vivo. Nature neuroscience *19*, 1085-1092.
970 Wu, B., Li, J., Chou, Y-H., Luginbuhl, D., and Luo, L. (2017) Fibroblast growth factor signaling instructs
971 ensheathing glia wrapping of *Drosophila* olfactory glomeruli. Proceedings of the National
972 Academy of Sciences of the United States of America *114*, 7505-7512.
973 Wyss-Coray, T., Loike, J.D., Brionne, T.C., Lu, E., Anankov, R., Yan, F., Silverstein, S.C., and
974 Husemann, J. (2003). Adult mouse astrocytes degrade amyloid-beta in vitro and in situ. Nature
975 medicine *9*, 453-457.
976 Yanamandra, K., Kfoury, N., Jiang, H., Mahan, T.E., Ma, S., Maloney, S.E., Wozniak, D.F., Diamond,
977 M.I., and Holtzman, D.M. (2013). Anti-tau antibodies that block tau aggregate seeding in vitro
978 markedly decrease pathology and improve cognition in vivo. Neuron *80*, 402-414.
979 Yun, S.P., Kam, T.I., Panicker, N., Kim, S., Oh, Y., Park, J.S., Kwon, S.H., Park, Y.J., Karuppagounder,
980 S.S., Park, H.*, et al.* (2018). Block of A1 astrocyte conversion by microglia is neuroprotective in
981 models of Parkinson's disease. Nature medicine *24*, 931-938.
982 Zeineddine, R., Pundavela, J.F., Corcoran, L., Stewart, E.M., Do-Ha, D., Bax, M., Guillemin, G., Vine,
983 K.L., Hatters, D.M., Ecroyd, H.*, et al.* (2015). SOD1 protein aggregates stimulate
984 macropinocytosis in neurons to facilitate their propagation. Molecular neurodegeneration *10*, 57.
985 Zhao, Y., Wu, X., Li, X., Jiang, L.L., Gui, X., Liu, Y., Sun, Y., Zhu, B., Pina-Crespo, J.C., Zhang, M.*, et*
986 *al.* (2018). TREM2 Is a Receptor for beta-Amyloid that Mediates Microglial Function. Neuron *97*,
987 1023-1031.

988

989 **FIGURE LEGENDS**

990 **Figure 1. mHtt$_{ex1}$ or mHtt$_{ex1-12}$ aggregates formed in presynaptic ORNs induce the aggregation of**
991 **wtHtt$_{ex1}$ expressed in postsynaptic PNs.** (A) Primary structure of full-length human Htt (3144 amino
992 acids), including HEAT repeats (HR, *gray regions*) and the N-terminal variable-length polyQ region
993 (*green/red box*), with the pathogenic threshold (~Q37) indicated by a white dotted line. C-termini of two
994 N-terminal mHtt fragments used in this study (Htt$_{ex1}$ and Htt$_{ex1-12}$) are indicated. (B) Overall experimental
995 approach. In the fly olfactory system, ORNs synapse with PNs in discrete regions of the antennal lobe
996 known as glomeruli (*gray circles*). PNs send axons into higher brain centers (i.e., mushroom body
997 and/or lateral horn). Draper-expressing glial cells project processes in the antennal lobe, where they
998 ensheath individual glomeruli. To monitor spreading of mHtt aggregates between synaptically-
999 connected ORNs and PNs, we generated transgenic flies that express mHtt$_{ex1}$ or mHtt$_{ex1-12}$ fragments in
1000 DA1 ORNs and wtHtt$_{ex1}$ in DA1 PNs. Inset: Transfer of mHtt$_{ex1}$ or mHtt$_{ex1-12}$ aggregates between ORNs
1001 and PNs was assessed by monitoring the solubility and colocalization of mHtt and wtHtt fluorescent
1002 signals. (C and D) Maximum intensity z-projections of antennal lobes from 7 day-old adult males
1003 expressing either Htt$_{ex1}$Q25-mCherry (C) or Htt$_{ex1}$Q91-mCherry (D) in DA1 ORNs using *Or67d-QF* and
1004 Htt$_{ex1}$Q25-GFP in GH146+ PNs using *GH146-Gal4*. Raw data are shown in grayscale for individual
1005 channels and pseudocolored in merged images. Merged images include Bruchpilot
1006 immunofluorescence in blue to mark neuropil, which was used to approximate the boundaries of the
1007 DA1 glomerulus (white dotted lines). Scale bars = 20 μm. (E-G) High-magnification confocal z-stacks of
1008 DA1 glomeruli from 1 day-old (E), 14 day-old (F), and 21 day-old (G) adult males expressing Htt$_{ex1}$Q91-
1009 mCherry in DA1 ORNs and Htt$_{ex1}$Q25-GFP in GH146+ PNs. Boxed regions in (F and G) are shown at
1010 higher magnification in insets. Raw data are shown in grayscale in individual channels (Htt$_{ex1}$Q91: E1,
1011 F1, G1; Htt$_{ex1}$Q25: E2, F2, G2) and pseudocolored in merged images (E3, F3, G3). mCherry+
1012 "Htt$_{ex1}$Q91 surfaces" (E1', F1', G1') and "Htt$_{ex1}$Q91+Htt$_{ex1}$Q25 surfaces" (E2', F2', G2') identified by
1013 semi-automated image segmentation are shown adjacent to raw data and pseudocolored red and
1014 yellow, respectively, in the "merged surfaces" images (E3', F3', G3'). Arrows (*yellow* on grayscale
1015 images, *white* on merged images) indicate Htt$_{ex1}$Q91+Htt$_{ex1}$Q25 surfaces. Scale bars = 10 μm. (H and I)

1016 Confocal z-stacks from 1 day-old (H) and 21 day-old (I) adult females expressing RFP-Htt_{ex1-12}Q138 in
1017 DA1 ORNs and Htt_{ex1}Q25-GFP in GH146+ PNs. Boxed region in (I) is shown at higher magnification in
1018 insets. RFP+ surfaces identified by semi-automated image segmentation are shown in the last column,
1019 with Htt_{ex1-12}Q138-only surfaces in red and Htt_{ex1-12}Q138+Htt_{ex1}Q25 surfaces in yellow. Scale bars = 10
1020 μm. (J) and (K) Numbers of Htt_{ex1}Q91 or Htt_{ex1-12}Q138 ("mHtt") surfaces (J) and Htt_{ex1}Q91+Htt_{ex1}Q25 or
1021 Htt_{ex1-12}Q138+Htt_{ex1}Q25 ("mHtt+wtHtt") surfaces (K) identified in adult males (*open bars*) or females
1022 (*solid bars*) expressing Htt_{ex1}Q91-mCherry in DA1 ORNs or adult females expressing RFP-Htt_{ex1-12}Q138
1023 in DA1 ORNs (*striped bars*) at the indicated ages. Data are shown as mean ± SEM; *p < 0.05, **p <
1024 0.01, ***p < 0.001, or ****p < 0.0001 by two-way ANOVA followed by Tukey's multiple comparisons
1025 tests. *s indicate statistical significance comparing flies of the same genotype and sex at different ages
1026 (black *s compare males or females expressing Htt_{ex1}Q91, and gray *s compare females expressing
1027 Htt_{ex1-12}Q138 over time). #s indicate statistical significance comparing different genotypes at the same
1028 age (black #s compare males vs females expressing Htt_{ex1}Q91, and gray #s compare females
1029 expressing Htt_{ex1}Q91 vs. females expressing Htt_{ex1-12}Q138).
1030
1031 **Figure 1 – figure supplement 1. mHtt_{ex1} nucleates prion-like conversion of wtHtt_{ex1} in fly**
1032 **neurons.** (A-E) Confocal z-stacks of 14 day-old adult female brains expressing (A) Htt_{ex1}Q91-mCherry
1033 or (B) Htt_{ex1}Q25-GFP alone, or co-expressing Htt_{ex1}Q91-mCherry with (C) Htt_{ex1}Q25-GFP, (D)
1034 membrane-targeted mCD8-GFP, or (E) soluble GFP in all neurons using *elav[C155]-Gal4*. Dimensions
1035 of each confocal stack are 250 x 250 x ~60 (*xyz*) μm. Merged images include DAPI signal (*blue*) to
1036 label nuclei. Scale bars = 20 μm. (F) Colocalization of mCherry and GFP fluorescent signals calculated
1037 as Pearson's correlation coefficients for genotypes shown in (A-E). Data are shown as mean ± SEM;
1038 ****p < 0.0001 by one-way ANOVA with Tukey's multiple comparisons test.
1039
1040 **Figure 1 – figure supplement 2. Semi-automatic quantification of seeded wtHtt_{ex1} aggregates.** (A
1041 and B) Semi-automatic image processing workflow for high-magnification confocal z-stacks of DA1
1042 glomeruli from 14 day-old adult males expressing Htt_{ex1}Q91-mCherry in DA1 ORNs and either (A1,2)

1043 Htt_{ex1}Q25-GFP or (B1,2) mCD8-GFP in GH146+ PNs. Raw data were preprocessed by deconvolution
1044 to reduce noise (*top panels*), segmented in the mCherry (A1 and B1) or GFP (A2 and B2) channels
1045 (*middle panels*), and filtered for co-localizing fluorescence signal in the other channel (*bottom panels*).
1046 Arrows in (A1 and A2) indicate seven Htt_{ex1}Q91+Htt_{ex1}Q25 puncta identified by this method. Scale bars
1047 = 10 μm. (C1-7) Selected single 0.35 μm confocal z-slices from the same confocal stack shown in (A1
1048 and A2). Slice number is indicated at the top right of each image. Individual Htt_{ex1}Q91+Htt_{ex1}Q25 puncta
1049 identified by semi-automated image segmentation in (A) are indicated with arrows (*yellow* in individual
1050 channels, *white* on merged images) in each slice. Two additional co-localized Htt_{ex1}Q91+Htt_{ex1}Q25
1051 puncta identified by manual counting are indicated with asterisks in (A2). Scale bars = 10 μm. Insets
1052 show Htt_{ex1}Q91+Htt_{ex1}Q25 puncta at higher zoom (inset dimensions = 9.12 μm x 9.12 μm). Htt_{ex1}Q91-
1053 mCherry (*red*) and Htt_{ex1}Q25-GFP (*green*) fluorescence intensity profiles for lines indicated in merged
1054 insets are shown below images. Lines were scanned from leftmost to rightmost point. (D) Comparison
1055 of manual quantification (C) vs semi-automated segmentation approaches (A1 and A2) for 14 day-old
1056 males with the same genotype in (A and C). Data are shown as mean ± SEM; n.s. = not significant by
1057 one-way ANOVA followed by Tukey's multiple comparisons test.
1058
1059 **Figure 1 – figure supplement 3. Controls for prion-like transmission of $mHtt_{ex1}$ aggregates from**
1060 **presynaptic DA1 ORNs to postsynaptic PNs.** (A-D) Confocal z-stacks of DA1 glomeruli from 10 day-
1061 old adults expressing (A) Htt_{ex1}Q25-mCherry in DA1 ORNs and Htt_{ex1}Q25-GFP in GH146+ PNs, (B)
1062 Htt_{ex1}Q91-mCherry in DA1 ORNs and mCD8-GFP in GH146+ PNs, (C) Htt_{ex1}Q91-mCherry together
1063 with Gal80 in DA1 ORNs and Htt_{ex1}Q25-GFP in GH146+ PNs, and (D) Htt_{ex1}Q91-mCherry in DA1
1064 ORNs and Htt_{ex1}Q25-GFP together with QS in GH146+ PNs. mCherry+ surfaces identified by semi-
1065 automated image segmentation are shown in the last panels, with Htt_{ex1}Q91-only surfaces in red and
1066 Htt_{ex1}Q91+Htt_{ex1}Q25 surfaces in yellow. Scale bars = 10 μm. (E and F) Quantification of (E) Httex1Q91
1067 and (F) Htt_{ex1}Q91+Htt_{ex1}Q25 aggregates in the DA1 glomeruli of flies with genotypes shown in (A-D).
1068 Data are shown as mean ± SEM. *$p < 0.05$, ****$p < 0.0001$ by one-way ANOVA with Tukey's multiple
1069 comparisons test.

1070

1071 **Figure 1 – figure supplement 4. mHtt$_{ex1}$ aggregates do not transfer retrogradely from PN**
1072 **dendrites to ORN axons.** Single confocal slices (A1-3 and B1-3) and confocal z-stacks (A4 and B4) of
1073 the antennal lobe from 7 (A) and 14 (B) day-old adult females expressing Htt$_{ex1}$Q91-mCherry in ~60%
1074 of PNs using *GH146-QF* and Htt$_{ex1}$Q25-GFP in all ORNs using *pebbled-Gal4*. Dissected brains were
1075 immunostained with antibodies against mCherry (*red*), GFP (*green*), and the neuropil marker Bruchpilot
1076 (*blue*, shown in merged images). GFP+ puncta identified in single slices are indicated by open
1077 arrowheads; none of these were found to be mCherry+. Semi-automated segmentation of the
1078 Htt$_{ex1}$Q91-mCherry fluorescent signal ("merge surfaces" in A4 and B4) identified numerous Htt$_{ex1}$Q91
1079 aggregates (graphed in C) throughout the antennal lobe neuropil and surrounding region. A small
1080 number of Htt$_{ex1}$Q91+Htt$_{ex1}$Q25 surfaces (graphed in D) were identified in these brains (arrows in A4
1081 and B4); however, none of these were located within the boundaries of the antennal lobe. Scale bars =
1082 10 μm; slice numbers are indicated at the top right in (A1-3 and B1-3). Quantified data in (C and D) are
1083 shown as mean ± SEM; n.s. = not significant by one-way ANOVA with Tukey's multiple comparisons
1084 test.

1085

1086 **Figure 2. wtHtt$_{ex1}$ aggregates in postsynaptic PNs are nucleated by mHtt$_{ex1}$ or mHtt$_{ex1-12}$**
1087 **aggregates from presynaptic ORNs.** (A-D) High-magnification confocal z-stacks of DA1 glomeruli
1088 from adult flies expressing Htt$_{ex1}$Q91-mCherry (A and B) or RFP-Htt$_{ex1-12}$Q138 (C and D) in DA1 ORNs
1089 and Htt$_{ex1}$Q25-GFP in GH146+ PNs. Raw data (A1-3, B1-3, C1-3, D1-3) are shown adjacent to
1090 surfaces identified by 3D segmentation of the red (A1', B1', C1', D1') or green (A2', B2', C2', D2')
1091 channels. Htt$_{ex1}$Q25-GFP surfaces are shown at 50% transparency in "merged surfaces" images (A3',
1092 B3', C3', D3') for visibility of co-localized Htt$_{ex1}$Q91-mCherry or RFP-Htt$_{ex1-12}$Q138 surfaces. Scale bars
1093 = 1 μm. (E1-4) A single confocal slice through the center of a Htt$_{ex1}$Q91+Htt$_{ex1}$Q25 aggregate before
1094 (E1, E2) and after (E1', E2') mCherry acceptor photobleaching. Data are shown as a heat map to
1095 highlight changes in fluorescence intensities after photobleaching. Scale bar = 1 μm. FRET efficiency
1096 (FRET$_{eff}$) for this aggregate is shown in (E4), and average FRET$_{eff}$ values for all Htt$_{ex1}$Q91+Htt$_{ex1}$Q25

1097 aggregates tested are shown in (E3). (F) Volumes of $Htt_{ex1}Q91$ (*solid red boxes*), $Htt_{ex1}Q91$+$Htt_{ex1}Q25$
1098 (*solid green boxes*), $Htt_{ex1-12}Q138$ (*striped red boxes*), and $Htt_{ex1-12}Q138$+$Htt_{ex1}Q25$ (*striped green*
1099 *boxes*) aggregates identified in the DA1 glomerulus at the indicated ages. Box widths indicate
1100 interquartile ranges, vertical lines inside each box indicate medians, whiskers indicate
1101 minimums/maximums, and "+"s indicate means for each data set. *$p < 0.05$, **$p < 0.01$, ***$p < 0.001$,
1102 ****$p < 0.0001$ by one-way ANOVA followed by Tukey's multiple comparisons test. Statistical
1103 significance is indicated by "*"s when comparing the same aggregate sub-population at different ages
1104 ($Htt_{ex1}Q91$ surfaces in *black* and $Htt_{ex1-12}Q138$ surfaces in *gray*), by "#"s when comparing $Htt_{ex1}Q91$ vs
1105 $Htt_{ex1}Q91$+$Htt_{ex1}Q25$ (*black*) or $Htt_{ex1-12}Q138$ vs $Htt_{ex1-12}Q138$+$Htt_{ex1}Q25$ (*gray*) aggregates at the same
1106 ages, and by "^"s when comparing $Htt_{ex1}Q91$ vs $Htt_{ex1-12}Q138$ aggregates at the same ages. (G and H)
1107 Distribution of volumes for (G) $Htt_{ex1}Q91$ (*light gray bars*) and $Htt_{ex1}Q91$+$Htt_{ex1}Q25$ (*dark gray bars*) or
1108 (H) $Htt_{ex1-12}Q138$ (*light gray bars*) and $Htt_{ex1-12}Q138$+$Htt_{ex1}Q25$ (*dark gray bars*) aggregates, combined
1109 from 7, 14, and 21 day-old flies. Mean volume of $Htt_{ex1}Q91$ or $Htt_{ex1-12}Q138$ aggregates and
1110 $Htt_{ex1}Q91$+$Htt_{ex1}Q25$ or $Htt_{ex1-12}Q138$+$Htt_{ex1}Q25$ aggregates are indicated by black and white dotted
1111 lines, respectively, on each histogram.
1112
1113 **Figure 3. $mHtt_{ex1}$ aggregate transfer from ORNs to synaptically-connected PNs is inversely**
1114 **correlated with presynaptic activity.** (A, B, E, F, I, and J) Confocal z-stacks of DA1 glomeruli from 10
1115 day-old males (A and B, and E and F) or 7 day-old females (I and J) co-expressing $Htt_{ex1}Q91$-mCherry
1116 with either LacZ (A, E, and I), shi^{ts1} (B), TeTxLC (F), or dTrpA (J) in DA1 ORNs and $Htt_{ex1}Q25$-GFP in
1117 GH146+ PNs. In (A-B), flies were raised at the permissive temperature (18°C) and shifted to the
1118 restrictive temperature (31°C) upon eclosion, and in (I-J), flies were raised at room temperature (~21°C)
1119 and shifted to 31°C upon eclosion. mCherry+ surfaces identified by semi-automated image
1120 segmentation are shown in the last panels, with $Htt_{ex1}Q91$-only surfaces in red and $Htt_{ex1}Q91$+$Htt_{ex1}Q25$
1121 surfaces in yellow. Scale bars = 10 μm. (C and D, G and H, and K and L) Quantification of $Htt_{ex1}Q91$ (C,
1122 G, and K) and $Htt_{ex1}Q91$+$Htt_{ex1}Q25$ (D, H, and L) aggregates identified in DA1 glomeruli from adult
1123 males of the indicated ages co-expressing $Htt_{ex1}Q91$-mCherry with LacZ or shi^{ts1} using two independent

1124 *QUAS-shi^{ts1}* lines in DA1 ORNs and Htt$_{ex1}$Q25-GFP in GH146+ PNs (C and D), adult males of the
1125 indicated ages co-expressing Htt$_{ex1}$Q91-mCherry with LacZ or TeTxLC using two independent *QUAS-*
1126 *TeTxLC* lines in DA1 ORNs and Htt$_{ex1}$Q25-GFP in GH146+ PNs (G and H), and 7 day-old females
1127 expressing Htt$_{ex1}$Q91-mCherry with either LacZ or dTrpA using three independent *QUAS-dTrpA* lines in
1128 DA1 ORNs and Htt$_{ex1}$Q25-GFP in GH146+ PNs (K and L). Data are shown as mean ± SEM; *$p < 0.05$,
1129 **$p < 0.01$, ***$p < 0.001$, ****$p < 0.0001$, n.s. = not significant by one- or two-way ANOVA with Tukey's
1130 multiple comparisons test comparing shi^{ts1}-, TeTxLC-, or dTrpA-expressing flies to their respective
1131 controls expressing LacZ.
1132
1133 **Figure 4. Inhibiting Shibire-mediated endocytosis increases mHttex1-expressing ORN axon**
1134 **volume and enhances transfer of mHtt$_{ex1}$ aggregates from DA1 ORN axons to glia.** (A and B)
1135 Confocal z-stacks of DA1 glomeruli from 10 day-old females co-expressing Htt$_{ex1}$Q91-mCherry, mCD8-
1136 GFP, and either LacZ (A) or shi^{ts1} (B) in DA1 ORNs. Flies were shifted from the permissive temperature
1137 (18°C) to the restrictive temperature (31°C) upon eclosion. Raw data are shown in grayscale, and 3D
1138 segmented surfaces are shown in red for Htt$_{ex1}$Q91 and as a heat map for mCD8-GFP to highlight
1139 differences in intensity between the genotypes. Scale bars = 10 μm. (C) Quantification of mCD8-GFP
1140 intensity (left y-axis, *green*) and volume (right y-axis, *black*) of DA1 glomeruli from 10 day-old adult
1141 females co-expressing LacZ or shi^{ts1} with Htt$_{ex1}$Q91-mCherry and mCD8-GFP in DA1 ORNs. a.u. =
1142 arbitrary units. Data are shown as mean ± SEM; ****$p < 0.0001$ by Student's t-test. (D and E) Confocal
1143 z-stacks of DA1 glomeruli from 5-6 day-old males expressing Htt$_{ex1}$Q91-mCherry with either LacZ (D) or
1144 shi^{ts1} (E) in DA1 ORNs and Htt$_{ex1}$Q25-YFP in repo+ glia. Adult flies were shifted from 18°C to 31°C
1145 upon eclosion. mCherry+ surfaces identified by semi-automated image segmentation are shown in the
1146 last panels, with Htt$_{ex1}$Q91-only surfaces in red and Htt$_{ex1}$Q91+Htt$_{ex1}$Q25 surfaces in yellow. Scale bars
1147 = 10 μm. (F and G) Quantification of Htt$_{ex1}$Q91 (F) and Htt$_{ex1}$Q91+Htt$_{ex1}$Q25 (G) aggregates in DA1
1148 glomeruli of 5-6 day-old males expressing LacZ or shi^{ts1} using two independent *QUAS-shi^{ts1}* lines. Data
1149 are shown as mean ± SEM; *$p < 0.05$, ****$p < 0.0001$ by one-way ANOVA with Tukey's multiple
1150 comparisons test comparing shi^{ts1}-expressing flies to control flies expressing LacZ.

1151

1152 **Figure 5. Draper mediates mHtt$_{ex1}$ aggregate transfer from presynaptic DA1 ORNs to**
1153 **postsynaptic PNs and regulates neuronal mHtt$_{ex1}$ aggregate size.** (A and B) Confocal z-stacks of
1154 DA1 glomeruli from 13 day-old adult females expressing Htt$_{ex1}$Q91-mCherry in DA1 ORNs and
1155 Htt$_{ex1}$Q25-GFP in GH146+ PNs, either heterozygous (A; *drpr*$^{+/-}$) or homozygous (B; *drpr*$^{-/-}$) for the *drpr*$^{\Delta 5}$
1156 null allele. mCherry+ surfaces identified by semi-automated image segmentation are shown in the last
1157 row, with Htt$_{ex1}$Q91-only surfaces in red and Htt$_{ex1}$Q91+Htt$_{ex1}$Q25 surfaces in yellow. Scale bars = 10
1158 µm. (C and D) Quantification of Htt$_{ex1}$Q91 (C) and Htt$_{ex1}$Q91+Htt$_{ex1}$Q25 (D) aggregates in DA1 glomeruli
1159 from female or male *drpr*$^{+/-}$ or *drpr*$^{-/-}$ flies at the indicated ages. Data are shown as mean ± SEM; *p <
1160 0.05, **p < 0.01, ****p < 0.0001 by two-way ANOVA with Sidak's multiple comparisons test for *drpr*$^{+/-}$
1161 vs. *drpr*$^{-/-}$ flies at the same ages. "n.d." = not determined; 13 day-old *drpr*$^{-/-}$ flies were not viable. (E and
1162 F) Htt$_{ex1}$Q91 surfaces identified in DA1 glomeruli from 7 day-old *drpr*$^{+/-}$ or *drpr*$^{-/-}$ females expressing
1163 Htt$_{ex1}$Q91-mCherry in DA1 ORNs. mCherry+ surfaces are color-coded according to the following
1164 volume ranges: cyan = 0-1.0 µm^3; gray = 1.01-2.49 µm^3; magenta = 2.5-9.0 µm^3. Gray and magenta
1165 surfaces were set to 70% transparency to improve visibility of smaller cyan surfaces. Scale bars = 10
1166 µm. (G) Relative frequency of volumes for all Htt$_{ex1}$Q91 aggregates identified in 7 day-old *drpr*$^{+/+}$ (*solid*
1167 *line*) or *drpr*$^{-/-}$ (*dotted line; gray shading*) males and females. The inset graph shows mean Htt$_{ex1}$Q91
1168 aggregate volume ± SEM for the two genotypes. ****p < 0.0001 by unpaired Student's t-test.

1169

1170 **Figure 5 – figure supplement 1. Draper is required for enhanced transfer of mHtt$_{ex1}$ from shi^{ts1}-**
1171 **expressing DA1 ORNs to GH146+ PNs.** (A and B) Confocal stacks of DA1 glomeruli from 7 day-old
1172 *drpr*$^{+/+}$ (A) or *drpr*$^{-/-}$ (B) adult females co-expressing Htt$_{ex1}$Q91-mCherry with shi^{ts1} in DA1 ORNs and
1173 Htt$_{ex1}$Q25-GFP in GH146+ PNs. Adult flies were shifted from 18°C to 31°C upon eclosion. mCherry+
1174 surfaces identified by semi-automated image segmentation are shown in the last panels, with
1175 Htt$_{ex1}$Q91-only surfaces in red and Htt$_{ex1}$Q91+Htt$_{ex1}$Q25 surfaces in yellow. Scale bars = 10 µm. (C and
1176 D) Quantification of Htt$_{ex1}$Q91 (C) and Htt$_{ex1}$Q91+Htt$_{ex1}$Q25 (D) aggregates for the same genotypes

1177 shown in (A and B). Data are shown as mean ± SEM; ****$p < 0.0001$ by Student's t-test comparing *drpr*
1178 $^{+/+}$ vs *drpr*$^{-/-}$ flies.
1179
1180 **Figure 5 – figure supplement 2. Gal80-mediated repression of Gal4 in glia or RNAi knockdown of**
1181 **drpr in PNs do not alter ORN-to-PN prion-like transfer of mHtt$_{ex1}$ aggregates.** (A and B) Confocal
1182 stacks of DA1 glomeruli from 10-14 day-old adult males expressing Htt$_{ex1}$Q91-mCherry in DA1 ORNs
1183 and Htt$_{ex1}$Q25-GFP in GH146+ PNs with (A) no additional transgenes ("control") or (B) repo-Gal80 to
1184 inhibit Gal4-mediated expression of Htt$_{ex1}$Q25-GFP in glia. (C and D) Confocal z-stacks of DA1
1185 glomeruli from 14 day-old adult males expressing Htt$_{ex1}$Q91-mCherry in DA1 ORNs and co-expressing
1186 Htt$_{ex1}$Q25-GFP together with firefly luciferase (FFLuc; C) or dsRNA targeting draper (Drpr^{RNAi}; D) in
1187 GH146+ PNs. In (A-D), mCherry+ surfaces identified by semi-automated image segmentation are
1188 shown in the last panels, with Htt$_{ex1}$Q91-only surfaces in red and Htt$_{ex1}$Q91+Htt$_{ex1}$Q25 surfaces in
1189 yellow. Scale bars = 10 μm. (E and F) Quantification of Htt$_{ex1}$Q91 (E) and Htt$_{ex1}$Q91+Htt$_{ex1}$Q25 (F)
1190 aggregates for genotypes shown in (A-D). Data are shown as mean ± SEM; n.s. = not significant by
1191 one-way ANOVA with Tukey's multiple comparisons tests.
1192
1193 **Figure 5 – figure supplement 3. mHtt$_{ex1}$ aggregates generated in ORNs do not co-localize with**
1194 **markers of lysosomes or autophagosomes in glia.** (A1-2 and B1-2) Single confocal slices from DA1
1195 glomeruli of 4-5 day-old adult males expressing Htt$_{ex1}$Q91-mCherry in DA1 ORNs and either the
1196 autophagosomal marker Atg8a-GFP (A1 and A2) or the lysosomal marker GFP-Lamp1 (B1 and B2) in
1197 repo+ glia. Scale bars = 10 μm. Htt$_{ex1}$Q91-mCherry (red) and Atg8a- or Lamp1-GFP (green)
1198 fluorescence intensity profiles for lines indicated in (A1-2 and B1-2) are shown below images; a.u. =
1199 arbitrary units. Lines were scanned from leftmost to rightmost point. (C and D) Confocal stacks of DA1
1200 glomeruli from 4-5 day-old adult males expressing Htt$_{ex1}$Q91-mCherry in DA1 ORNs and either Atg8a-
1201 GFP (C) or GFP-Lamp1 (D) in repo+ glia. mCherry+ surfaces identified by semi-automated image
1202 segmentation are shown in the last panels, with Htt$_{ex1}$Q91-only surfaces in red and Htt$_{ex1}$Q91+GFP
1203 surfaces in yellow. Scale bars = 10 μm. (E and F) Quantification of Htt$_{ex1}$Q91 (E) and Htt$_{ex1}$Q91+GFP

1204 (F) surfaces for the same genotypes as in (C and D) and for control animals expressing mCD8-GFP in
1205 glia. Data are shown as mean ± SEM; n.s. = not significant by one-way ANOVA with Tukey's multiple
1206 comparisons test.
1207
1208 **Figure 6. Caspase activation in ORNs mediates mHtt$_{ex1}$ aggregate transfer from ORNs to PNs.**
1209 (A-D) Maximum-intensity projections of antennal lobes from 8 day-old adult males expressing
1210 Htt$_{ex1}$Q25-GFP (A and C) or Htt$_{ex1}$Q91-GFP (B and D) in most ORNs using *Or83b-Gal4* in *drpr*$^{\Delta 5}$
1211 heterozygotes (*drpr*$^{+/-}$; A and B) or homozygotes (*drpr*$^{-/-}$; C and D). Brains were immunostained for
1212 GFP (left panels) or cleaved Dcp-1 (right panels). Scale bars = 20 μm. (E) Quantification of cDcp-1
1213 immunofluorescence from 8 day-old adult males with the same genotypes as in (A-D). Data are shown
1214 as mean ± SEM; **p < 0.01, ***p < 0.001, n.s. = not significant by one-way ANOVA with Tukey's
1215 multiple comparisons test. (F-I) Confocal z-stacks of DA1 glomeruli from 14 day-old males expressing
1216 Htt$_{ex1}$Q91-mCherry with LacZ (F) or p35 (G) in DA1 ORNs and Htt$_{ex1}$Q25-GFP in GH146+ PNs, or
1217 Htt$_{ex1}$Q91-mCherry in DA1 ORNs and Htt$_{ex1}$Q25-GFP with LacZ (H) or p35 (I) in GH146+ PNs.
1218 mCherry+ surfaces identified by 3D segmentation are shown in the last panels, with Htt$_{ex1}$Q91-only
1219 surfaces in red and Htt$_{ex1}$Q91+Htt$_{ex1}$Q25 surfaces in yellow. Scale bars = 10 μm. (J and K)
1220 Quantification of Htt$_{ex1}$Q91 (J) or Htt$_{ex1}$Q91+Htt$_{ex1}$Q25 (K) aggregates in DA1 glomeruli of flies with the
1221 same genotypes in (F and G) (*squares*) or (H and I) (*circles*). Numbers of aggregates in flies expressing
1222 LacZ or p35 are indicated by solid or open shapes, respectively. Data are shown as mean ± SEM; *p <
1223 0.05, n.s. = not significant by one-way ANOVA with Tukey's multiple comparisons test.
1224
1225 **Figure 7. mHtt$_{ex1}$ aggregates transfer from presynaptic ORNs to postsynaptic PNs via the**
1226 **cytoplasm of phagocytic glia.** (A) Diagram illustrating our experimental approach for examining a role
1227 for Draper-expressing glia in mHtt$_{ex1}$ aggregate transfer from DA1 ORNs to DA1 PNs. Flies that
1228 combined *Or67d-QF*-, *repo-Gal4*-, and *GH146-LexA:GAD*-driven expression of Htt$_{ex1}$Q91-mCherry in
1229 DA1 ORNs, Htt$_{ex1}$Q25-3xHA in all glia, and Htt$_{ex1}$Q25-YFP in ~60% of PNs, respectively, were
1230 generated and analyzed by confocal microscopy of immunostained brains. If Htt$_{ex1}$Q91-mCherry

1231 aggregates travel to PNs via the glial cytoplasm (route 1), triple-labeled (mCherry+/3xHA+/YFP+)
1232 aggregates should be observed. By contrast, if Htt_{ex1}Q91-mCherry aggregates transfer directly to PNs
1233 without accessing the glial cytoplasm (route 2), then only double-labeled (mCherry+/3xHA+ and
1234 mCherry+/YFP+) aggregates would be detected. (B-C) Confocal z-stacks of DA1 glomeruli from adult
1235 females of the indicated ages expressing Htt_{ex1}Q91-mCherry in DA1 ORNs (red), Htt_{ex1}Q25-3xHA in
1236 glia (blue), and Htt_{ex1}Q25-YFP in PNs (green) at the indicated ages. Brains were immunostained with
1237 antibodies against the mCherry, 3xHA, and YFP tags unique to each Htt protein. Scale bars = 10 μm.
1238 (D-H) Single 0.35 μm confocal z-slices from females of the indicated ages with (D-G) the same
1239 genotype as in (B and C) or (H) also expressing dsRNAs targeting *drpr* (+$Drpr^{RNAi}$). Colocalizing
1240 mCherry+/3xHA+ or mCherry+/3xHA+/YFP+ aggregates are indicated by open arrowheads or arrows,
1241 respectively, shown in yellow on grayscale and white on merged images for increased visibility. Scale
1242 bars = 5 μm. Htt_{ex1}Q91-mCherry (red), Htt_{ex1}Q25-3xHA (blue), and Htt_{ex1}Q25-YFP (green) fluorescence
1243 intensity profiles for lines “a” and “b” are shown to the right of each merged image. Lines were scanned
1244 from leftmost to rightmost point. Arrowheads and arrows on graphs indicate peak mCherry fluorescence
1245 in colocalized mCherry+/3xHA+ and mCherry+/3xHA+/YFP+ aggregates, respectively. (I and J)
1246 Quantification of (I) mCherry-only or (J) mCherry+/3xHA+ and mCherry+/3xHA+/YFP+ aggregates
1247 identified in control (*solid bars*) or $Drpr^{RNAi}$-expressing (*open bars*) animals over time. +$Drpr^{RNAi}$ animals
1248 were only analyzed at 7 days-old. Data are shown as mean ± SEM; *$p < 0.05$, **$p < 0.01$, ***$p < 0.001$,
1249 or ****$p < 0.0001$ by one- or two-way ANOVA followed by Tukey’s multiple comparisons test. *s indicate
1250 statistical significance comparing control flies at different ages [black *s compare mCherry-only
1251 aggregates in (I) and mCherry+/3xHA+/YFP+ aggregates in (J), and blue *s compare mCherry+/3xHA+
1252 aggregates in (J)], and #s indicate statistical significance comparing mCherry+/3xHA+ and
1253 mCherry+/3xHA+/YFP+ aggregates, respectively, in control vs $Drpr^{RNAi}$-expressing flies at the same
1254 age.
1255
1256 **Figure 7 - figure supplement 1. Controls for monitoring transmission of $mHtt_{ex1}$ aggregates from**
1257 **presynaptic DA1 ORNs to postsynaptic PNs via a glial intermediate.** (A-C) Confocal z-stacks (A1,

1258 B1, and C1) and single 0.35 μm z-slices (A2, B2, and C2) of DA1 glomeruli from 4-6 day-old adult
1259 females expressing (A1-2) Htt_{ex1}Q25-mCherry in DA1 ORNs and Ht_{tex1}Q25-3xHA in repo+ glia, (B1-2)
1260 Htt_{ex1}Q25-mCherry in DA1 ORNs and Htt_{ex1}Q25-YFP in GH146+ PNs, or (C1-2) Htt_{ex1}Q25-3xHA in
1261 repo+ glia and Htt_{ex1}Q25-YFP in GH146+ PNs. All brains were immunostained with antibodies against
1262 all three epitope tags (i.e., mCherry, YFP, and 3xHA) to show specific staining. Scale bars = 10 μm in
1263 (A1, B1, and C1) and 5 μm in (A2, B2, and C2). Htt_{ex1}Q25-mCherry (red), Htt_{ex1}Q25-3xHA (blue), and
1264 Htt_{ex1}Q25-YFP (green) fluorescence intensity profiles for lines "a" and "b" shown in merged slices (A2,
1265 B2, and C2) are shown below images. Lines were scanned from leftmost to rightmost point.
1266
1267 **Video 1. Semi-automated quantification of mHtt_{ex1} and seeded wtHtt_{ex1} aggregates in the DA1**
1268 **glomerulus**. Animation illustrating semi-automated approach for quantifying mHtt_{ex1} and wtHtt_{ex1}
1269 aggregates in brains expressing Htt_{ex1}Q91-mCherry in DA1 ORNs and Htt_{ex1}Q25-GFP in GH146+ PNs.
1270 Data shown in video is the same as in Fig. 1-figure supplement 2A1-2 and C1-7. Segmentation of raw
1271 high-magnification 3D confocal data (0:00) in the red channel (0:07) identified distinct Htt_{ex1}Q91-
1272 mCherry surfaces (0:09), which were filtered for those that co-localize with high-intensity GFP signal to
1273 isolate the subpopulation associated with Htt_{ex1}Q25-GFP puncta (0:13). Volumetric surfaces
1274 representing Htt_{ex1}Q91 (*red*) and Htt_{ex1}Q91+Htt_{ex1}Q25 (*yellow*) aggregates (0:18) are shown for each
1275 data set analyzed by this method. The animation also illustrates segmentation of raw data in the green
1276 channel (0:28) to identify the brightest Htt_{ex1}Q25-GFP objects in each data set (0:29). Overlap of
1277 mCherry+ and GFP+ surfaces, with GFP+ surfaces set at 50% transparency (0:30), highlights co-
1278 localization of smaller Htt_{ex1}Q91 "seeds" surrounded by Htt_{ex1}Q25 signal in these aggregates.

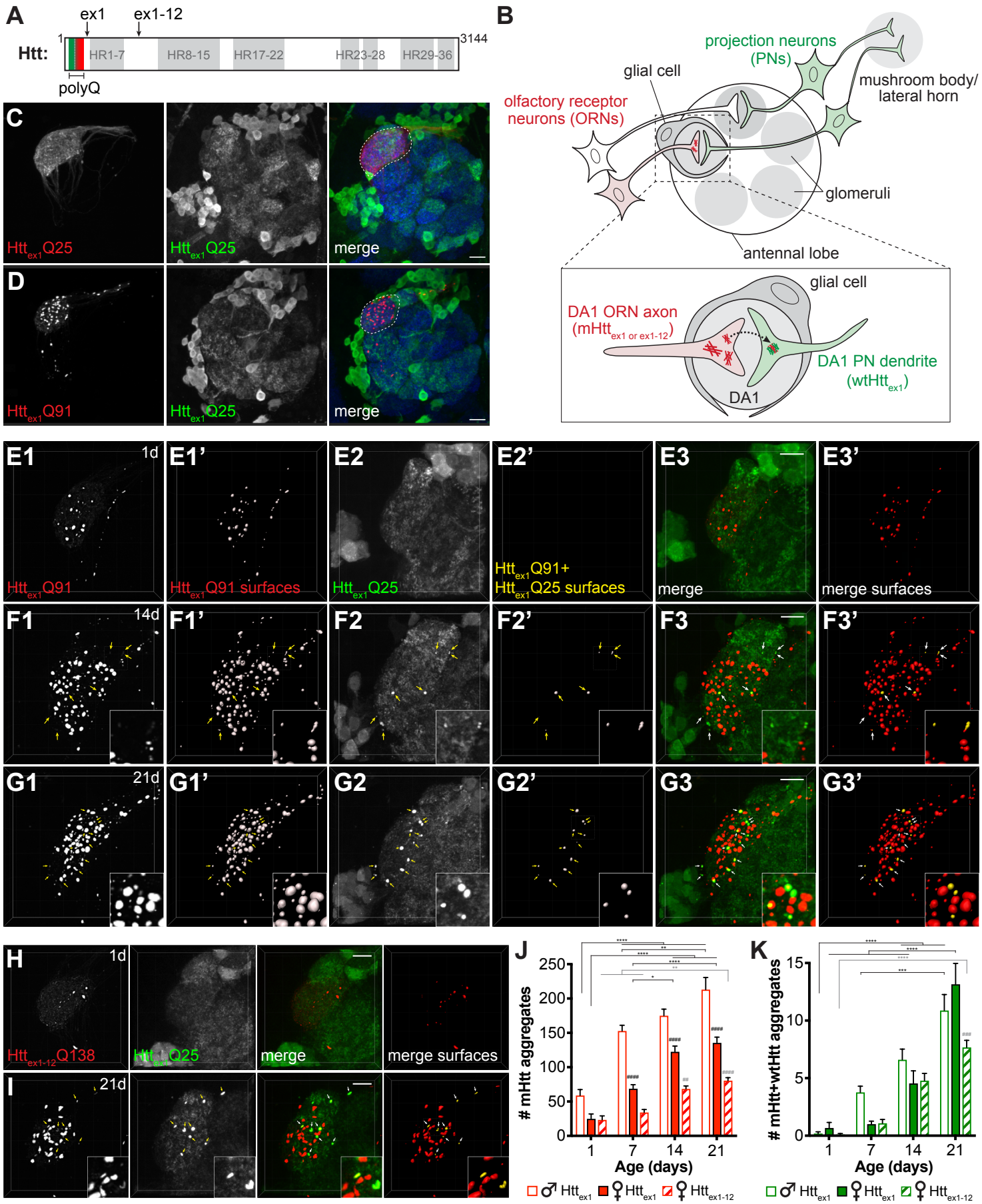
A
ex1
ex1-12
Htt:
1
3144
HR1-7
HR8-15
HR17-22
HR23-28
HR29-36
polyQ
B
projection neurons (PNs)
glial cell
mushroom body/ lateral horn
olfactory receptor neurons (ORNs)
glomeruli
antennal lobe
glial cell
DA1 ORN axon (mHtt ex1 or ex1-12)
DA1 PN dendrite (wtHtt ex1)
DA1
C
Htt ex1 Q25
Htt ex1 Q25
merge
D
Htt ex1 Q91
Htt ex1 Q25
merge
E1
1d
Htt ex1 Q91
E1'
Htt ex1 Q91 surfaces
E2
Htt ex1 Q25
E2'
Htt ex1 Q91+ Htt ex1 Q25 surfaces
E3
merge
E3'
merge surfaces
F1
14d
F1'
F2
F2'
F3
F3'
G1
21d
G1'
G2
G2'
G3
G3'
H
1d
Htt ex1-12 Q138
Htt ex1 Q25
merge
merge surfaces
I
21d
J
mHtt aggregates
Age (days)
Htt ex1
Htt ex1
Htt ex1-12
K
mHtt+wtHtt aggregates
Age (days)
Htt ex1
Htt ex1
Htt ex1-12

Figure 1. $mHtt_{ex1}$ or $mHtt_{ex1-12}$ aggregates formed in presynaptic ORNs induce the aggregation of $wtHtt_{ex1}$ expressed in postsynaptic PNs. (A) Primary structure of full-length human Htt (3144 amino acids), including HEAT repeats (HR, *gray regions*) and the N-terminal variable-length polyQ region (*green/red box*), with the pathogenic threshold (~Q37) indicated by a white dotted line. The C-termini of two N-terminal mHtt fragments used in this study (ex1 and ex1-12) are indicated. (B) Overall experimental approach. In the fly olfactory system, ORNs synapse with PNs in discrete regions of the antennal lobe known as glomeruli (*gray circles*). PNs send axons into higher brain centers (i.e., mushroom body and/or lateral horn). Draper-expressing glial cells project processes in the antennal lobe, where they ensheath individual glomeruli. To monitor spreading of mHtt aggregates between synaptically-connected ORNs and PNs, we generated transgenic flies that express $mHtt_{ex1}$ or $mHtt_{ex1-12}$ fragments in DA1 ORNs and $wtHtt_{ex1}$ in DA1 PNs. Inset: Transfer of $mHtt_{ex1}$ or $mHtt_{ex1-12}$ aggregates between ORNs and PNs was assessed by monitoring the solubility and co-localization of mHtt and wtHtt fluorescent signals. (C and D) Maximum intensity z-projections of antennal lobes from 7 day-old adult males expressing either Htt_{ex1}Q25-mCherry (C) or Htt_{ex1}Q91-mCherry (D) in DA1 ORNs and Htt_{ex1}Q25-GFP in GH146+ PNs. Raw data are shown in grayscale for individual channels and pseudocolored in merged images. Merged images include Bruchpilot immunofluorescence in blue to mark neuropil, which was used to approximate the boundaries of the DA1 glomerulus (*white dotted lines*). Scale bars = 20 μm. (E-G) High-magnification confocal z-stacks of DA1 glomeruli from 1 day-old (E), 14 day-old (F), and 21 day-old (G) adult males expressing Htt_{ex1}Q91-mCherry in DA1 ORNs and Htt_{ex1}Q25-GFP in GH146+ PNs. Boxed regions in (F and G) are shown at higher magnification in insets. Raw data are shown in grayscale in individual channels (Htt_{ex1}Q91: E1, F1, G1; Htt_{ex1}Q25: E2, F2, G2) and pseudocolored in merged images (E3, F3, G3). mCherry+ "Htt_{ex1}Q91 surfaces" (E1', F1', G1') and "Htt_{ex1}Q91+Htt_{ex1}Q25 surfaces" (E2', F2', G2') identified by semi-automated image segmentation are shown adjacent to raw data and pseudocolored red and yellow, respectively, in the "merged surfaces" images (E3', F3', G3'). Arrows (yellow on grayscale images, white on merged images) indicate Htt_{ex1}Q91+Htt_{ex1}Q25 surfaces. Scale bars = 10 μm. (H and I) Confocal z-stacks from 1 day-old (H) and 21 day-old (I) adult females expressing RFP-Htt_{ex1-12}Q138 in DA1 ORNs and Htt_{ex1}Q25-GFP in GH146+ PNs. Boxed region in (I) is shown at higher magnification in insets. RFP+ surfaces identified by semi-automated image segmentation are shown in the last column, with Htt_{ex1-12}Q138-only surfaces in red and Htt_{ex1-12}Q138+Htt_{ex1}Q25 surfaces in yellow. Scale bars = 10 μm. (J) and (K) Numbers of Htt_{ex1}Q91 or Htt_{ex1-12}Q138 ("mHtt") surfaces (J) and Htt_{ex1}Q91+Htt_{ex1}Q25 or Htt_{ex1-12}Q138+Htt_{ex1}Q25 ("mHtt+wtHtt") surfaces (K) identified in adult males (*open bars*) or females (*solid bars*) expressing Htt_{ex1}Q91-mCherry in DA1 ORNs or adult females expressing RFP-Htt_{ex1-12}Q138 in DA1 ORNs (*striped bars*) at the indicated ages. Data are shown as mean ± SEM; *$p < 0.05$, **$p < 0.01$, ***$p < 0.001$, or ****$p < 0.0001$ by two-way ANOVA followed by Tukey's multiple comparisons tests. *s indicate statistical significance comparing flies of the same genotype and sex at different ages (black *s compare males or females expressing Htt_{ex1}Q91, and gray *s compare females expressing Htt_{ex1-12}Q138 over time). #s indicate statistical significance comparing different genotypes at the same age (black #s compare males vs females expressing Htt_{ex1}Q91, and gray #s compare females expressing Htt_{ex1}Q91 vs. females expressing Htt_{ex1-12}Q138).

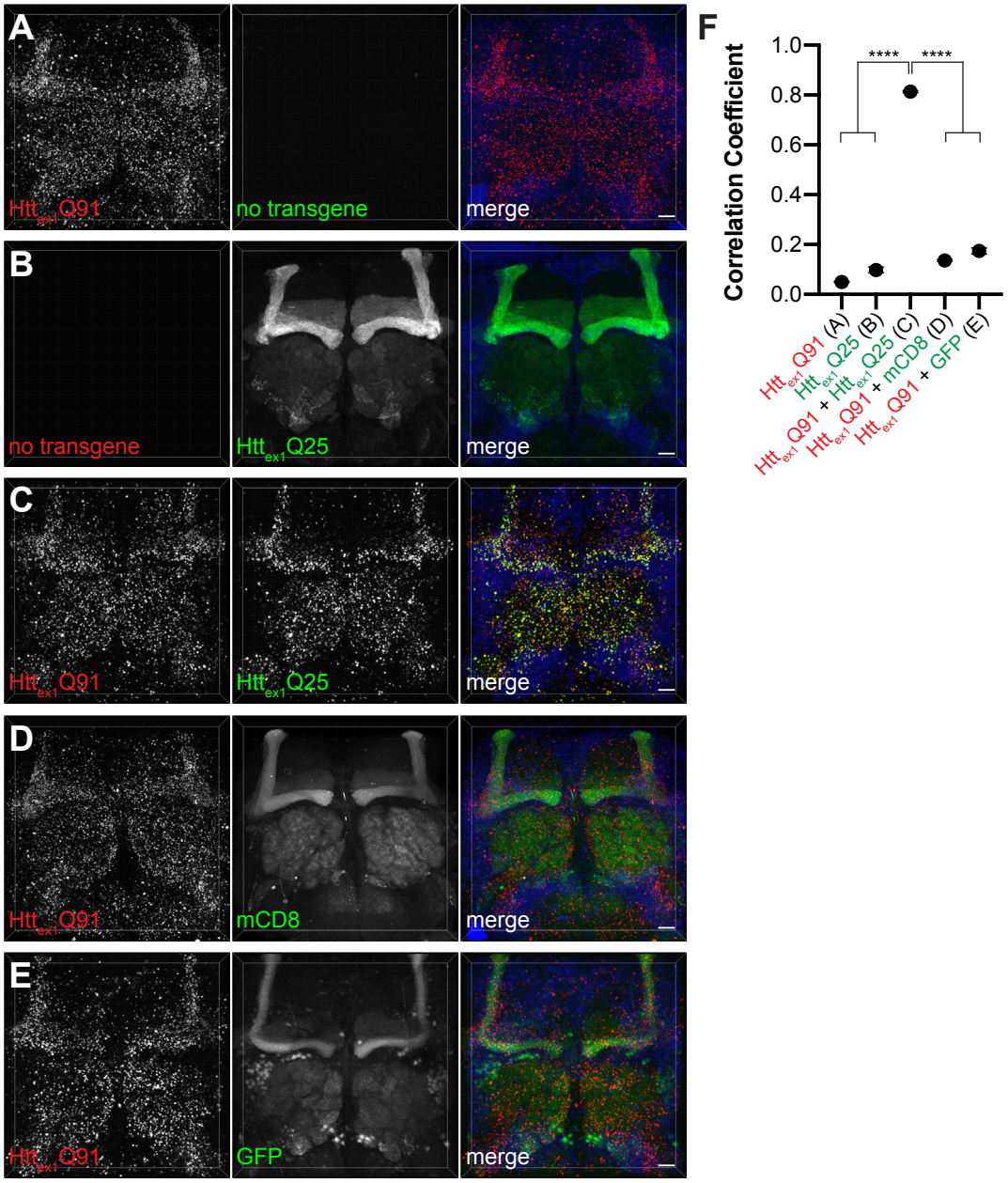

Figure 1 – figure supplement 1. mHtt$_{ex1}$ nucleates prion-like conversion of wtHtt$_{ex1}$ in fly neurons. (A-E) Confocal z-stacks of 14 day-old adult female brains expressing (A) Htt$_{ex1}$Q91-mCherry or (B) Htt$_{ex1}$Q25-GFP alone, or co-expressing Htt$_{ex1}$Q91-mCherry with (C) Htt$_{ex1}$Q25-GFP, (D) membrane-targeted mCD8-GFP, or (E) soluble GFP in all neurons using *elav[C155]-Gal4*. Dimensions of each confocal stack are 250 x 250 x ~60 (*xyz*) μm. Merged images include DAPI signal (*blue*) to label nuclei. Scale bars = 20 μm. (F) Co-localization of mCherry and GFP fluorescent signals calculated as Pearson's correlation coefficients for genotypes shown in (A-E). Data are shown as mean ± SEM; ****$p < 0.0001$ by one-way ANOVA with Tukey's multiple comparisons test.

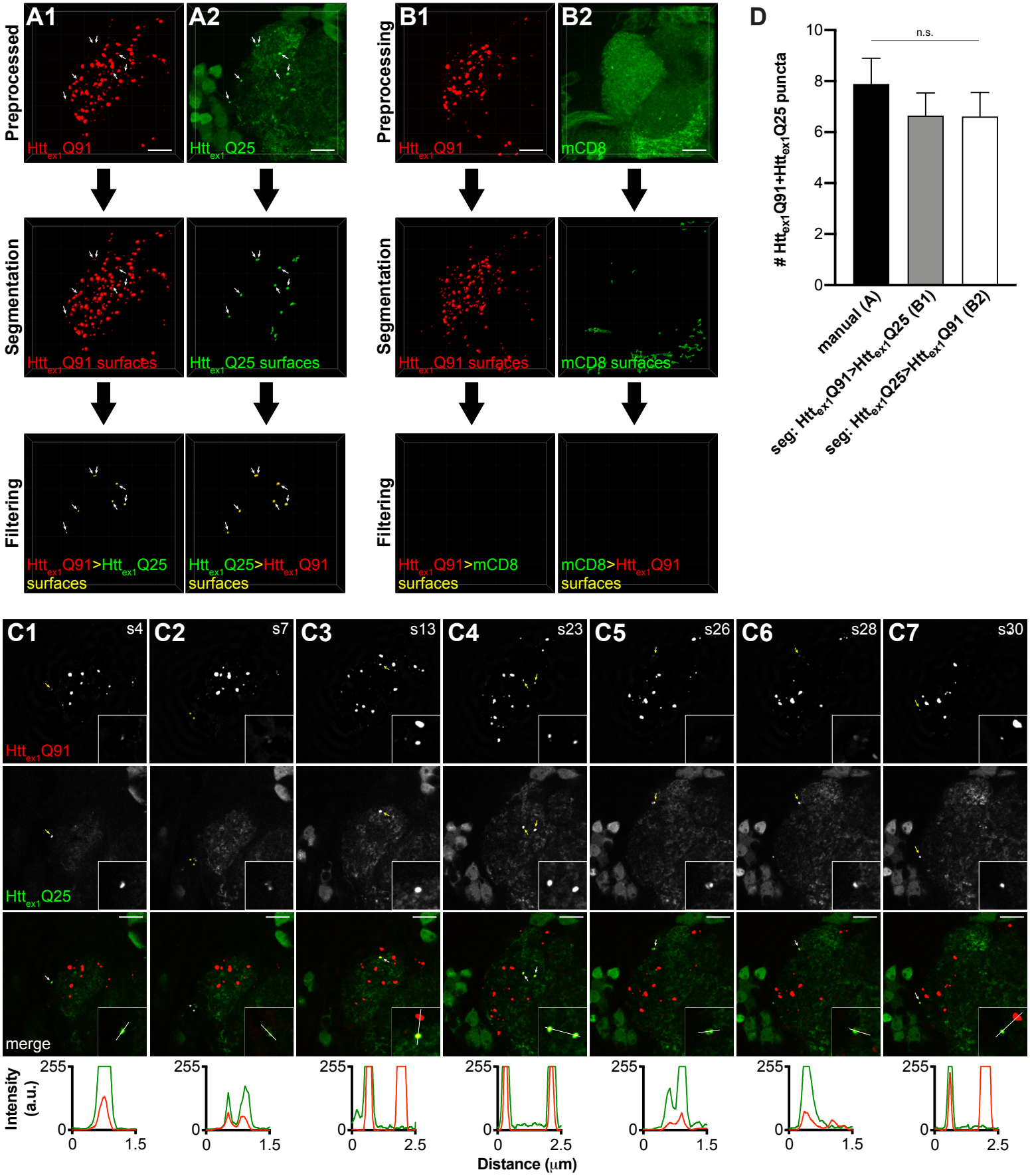
A1
A2
B1
B2
Preprocessed
Preprocessing
Segmentation
Filtering
Htt$_{ex1}$Q91
Htt$_{ex1}$Q25
mCD8
Htt$_{ex1}$Q91 surfaces
Htt$_{ex1}$Q25 surfaces
mCD8 surfaces
Htt$_{ex1}$Q91>Htt$_{ex1}$Q25 surfaces
Htt$_{ex1}$Q25>Htt$_{ex1}$Q91 surfaces
Htt$_{ex1}$Q91>mCD8 surfaces
mCD8>Htt$_{ex1}$Q91 surfaces
D
n.s.
Htt$_{ex1}$Q91+Htt$_{ex1}$Q25 puncta
manual (A)
seg: Htt$_{ex1}$Q91>Htt$_{ex1}$Q25 (B1)
seg: Htt$_{ex1}$Q25>Htt$_{ex1}$Q91 (B2)
C1 s4
C2 s7
C3 s13
C4 s23
C5 s26
C6 s28
C7 s30
Htt$_{ex1}$Q91
Htt$_{ex1}$Q25
merge
Intensity (a.u.)
Distance (μm)

Figure 1 – figure supplement 2. Semi-automatic quantification of seeded wtHtt$_{ex1}$ aggregates. (A and B) Semi-automatic image processing workflow for high-magnification confocal z-stacks of DA1 glomeruli from 14 day-old adult males expressing Htt$_{ex1}$Q91-mCherry in DA1 ORNs and either (A1,2) Htt$_{ex1}$Q25-GFP or (B1,2) mCD8-GFP in GH146+ PNs. Raw data were preprocessed by deconvolution to reduce noise (*top panels*), segmented in the mCherry (A1 and B1) or GFP (A2 and B2) channels (*middle panels*), and filtered for co-localizing fluorescence signal in the other channel (*bottom panels*). Arrows in (A1 and A2) indicate seven Htt$_{ex1}$Q91+Htt$_{ex1}$Q25 puncta identified by this method. Scale bars = 10 μm. (C1-7) Selected single 0.35 μm confocal z-slices from the same confocal stack shown in (A1 and A2). Slice number is indicated at the top right of each image. Individual Htt$_{ex1}$Q91+Htt$_{ex1}$Q25 puncta identified by semi-automated image segmentation in (A) are indicated with arrows (yellow in individual channels, white on merged images) in each slice. Two additional co-localized Htt$_{ex1}$Q91+Htt$_{ex1}$Q25 puncta identified by manual counting are indicated with asterisks in (A2). Scale bars = 10 μm. Insets show Htt$_{ex1}$Q91+Htt$_{ex1}$Q25 puncta at higher zoom (inset dimensions = 9.12 μm x 9.12 μm). Htt$_{ex1}$Q91-mCherry (*red*) and Htt$_{ex1}$Q25-GFP (*green*) fluorescence intensity profiles for lines indicated in merged insets are shown below images. Lines were scanned from leftmost to rightmost point. (D) Comparison of manual quantification (C) vs semi-automated segmentation approaches (A1 and A2) for 14 day-old males with the same genotype in (A and C). Data are shown as mean ± SEM; n.s. = not significant by one-way ANOVA followed by Tukey's multiple comparisons test.

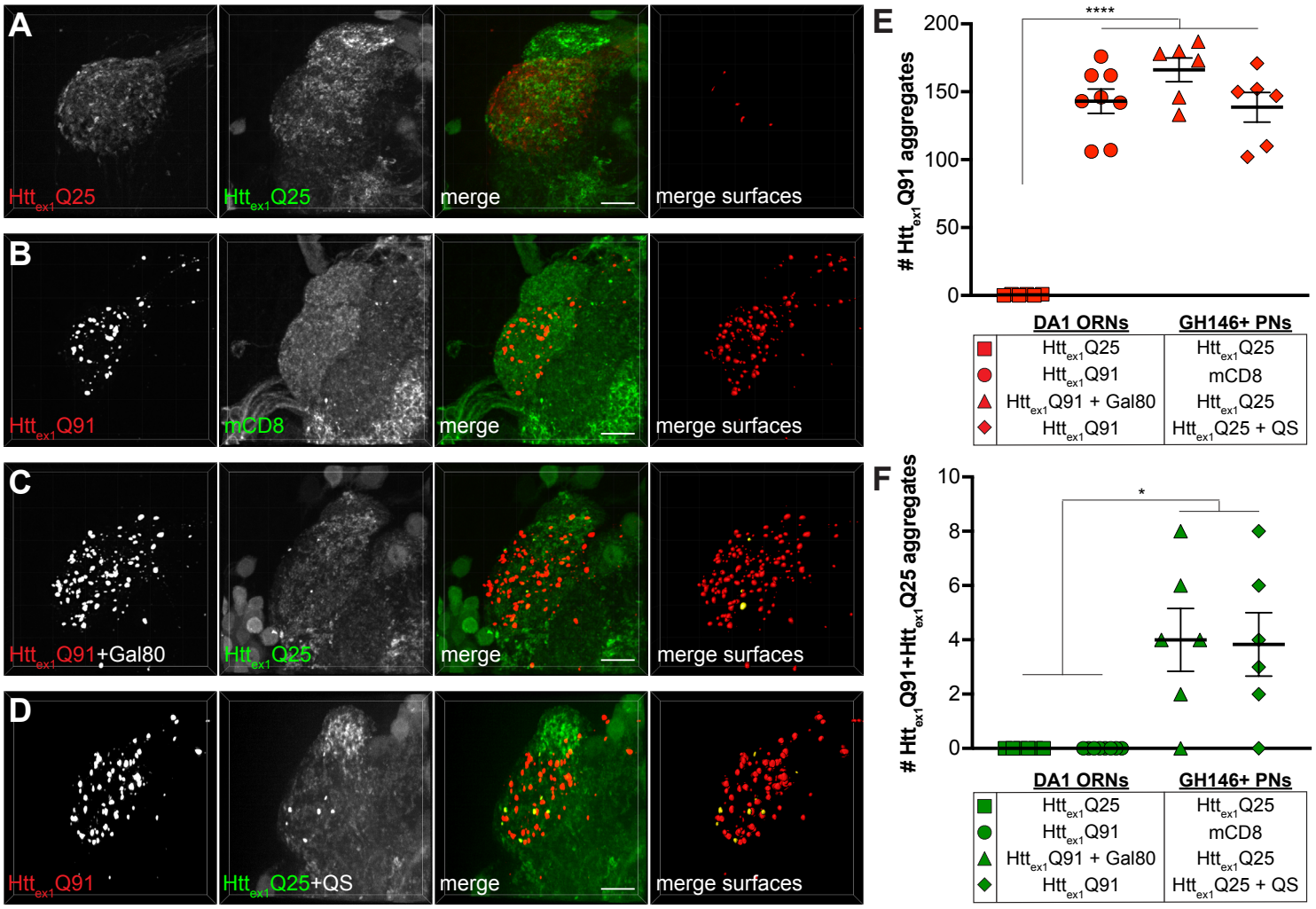

Figure 1 – figure supplement 3. Controls for prion-like transmission of mHtt$_{ex1}$ aggregates from presynaptic DA1 ORNs to postsynaptic PNs. (A-D) Confocal z-stacks of DA1 glomeruli from 10 day-old adults expressing (A) Htt$_{ex1}$Q25-mCherry in DA1 ORNs and Htt$_{ex1}$Q25-GFP in GH146+ PNs, (B) Htt$_{ex1}$Q91-mCherry in DA1 ORNs and mCD8-GFP in GH146+ PNs, (C) Htt$_{ex1}$Q91-mCherry together with Gal80 in DA1 ORNs and Htt$_{ex1}$Q25-GFP in GH146+ PNs, and (D) Htt$_{ex1}$Q91-mCherry in DA1 ORNs and Htt$_{ex1}$Q25-GFP together with QS in GH146+ PNs. mCherry+ surfaces identified by semi-automated image segmentation are shown in the last panels, with Htt$_{ex1}$Q91-only surfaces in red and Htt$_{ex1}$Q91+Htt$_{ex1}$Q25 surfaces in yellow. Scale bars = 10 μm. (E and F) Quantification of (E) Htt$_{ex1}$Q91 and (F) Htt$_{ex1}$Q91+Htt$_{ex1}$Q25 aggregates in the DA1 glomeruli of flies with genotypes shown in (A-D). Data are shown as mean ± SEM. *$p < 0.05$, ****$p < 0.0001$ by one-way ANOVA with Tukey's multiple comparisons test.

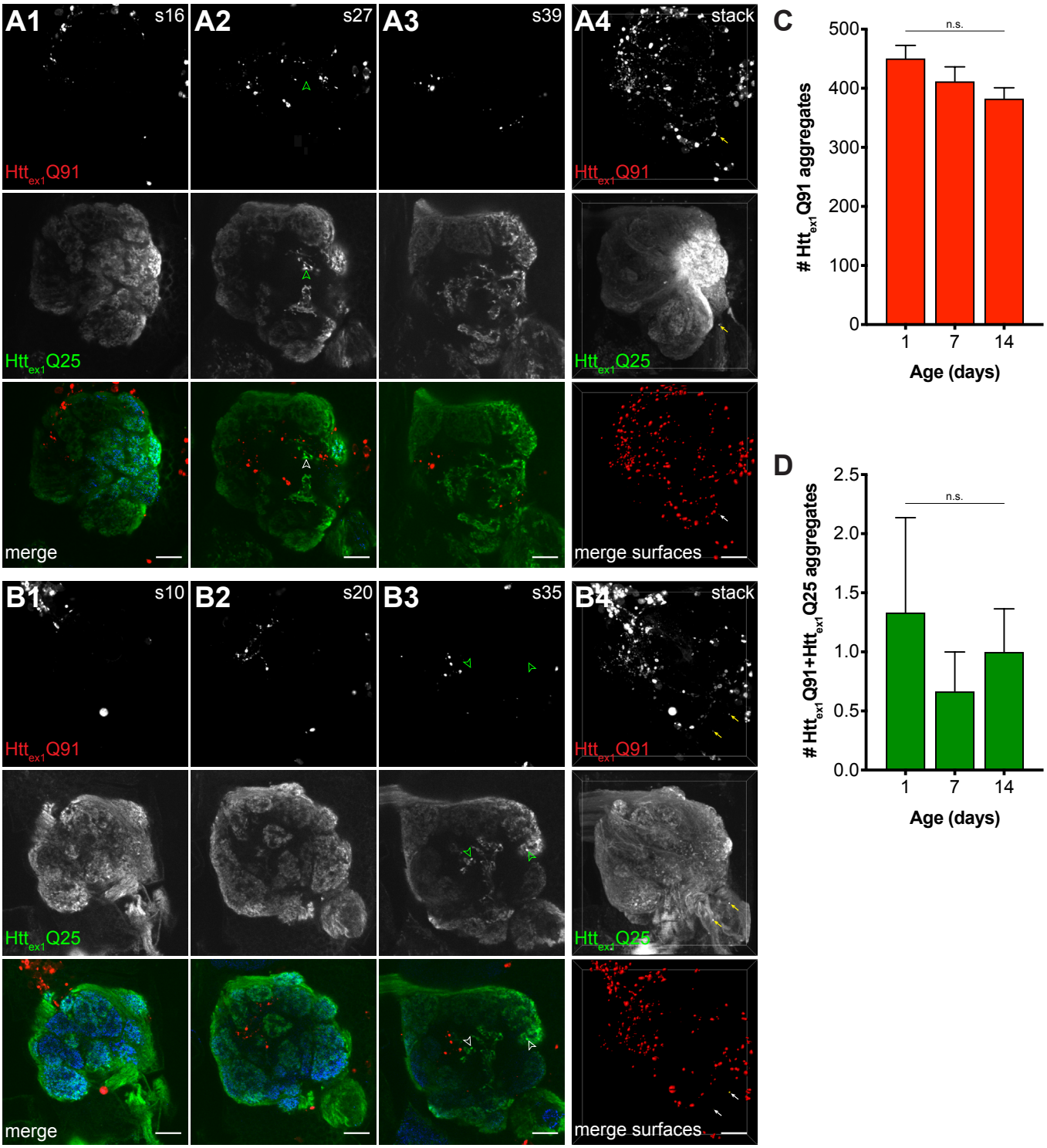

Figure 1 – figure supplement 4. mHtt$_{ex1}$ aggregates do not transfer retrogradely from PN dendrites to ORN axons. Single confocal slices (A1-3 and B1-3) and confocal z-stacks (A4 and B4) of the antennal lobe from 7 (A) and 14 (B) day-old adult females expressing Htt$_{ex1}$Q91-mCherry in ~60% of PNs using *GH146-QF* and Htt$_{ex1}$Q25-GFP in all ORNs using *pebbled-Gal4*. Dissected brains were immunostained with antibodies against mCherry (*red*), GFP (*green*), and the neuropil marker Bruchpilot (*blue*, shown in merged images). GFP+ puncta identified in single slices are indicated by open arrowheads; none of these were found to be mCherry+. Semi-automated segmentation of the Htt$_{ex1}$Q91-mCherry fluorescent signal ("merge surfaces" in A4 and B4) identified numerous Htt$_{ex1}$Q91 aggregates (graphed in C) throughout the antennal lobe neuropil and surrounding region. A small number of Htt$_{ex1}$Q91+Htt$_{ex1}$Q25 surfaces (graphed in D) were identified in these brains (arrows in A4 and B4); however, none of these were located within the boundaries of the antennal lobe. Scale bars = 10 μm; slice numbers are indicated at the top right in (A1-3 and B1-3). Quantified data in (C and D) are shown as mean ± SEM; n.s. = not significant by one-way ANOVA with Tukey's multiple comparisons test.

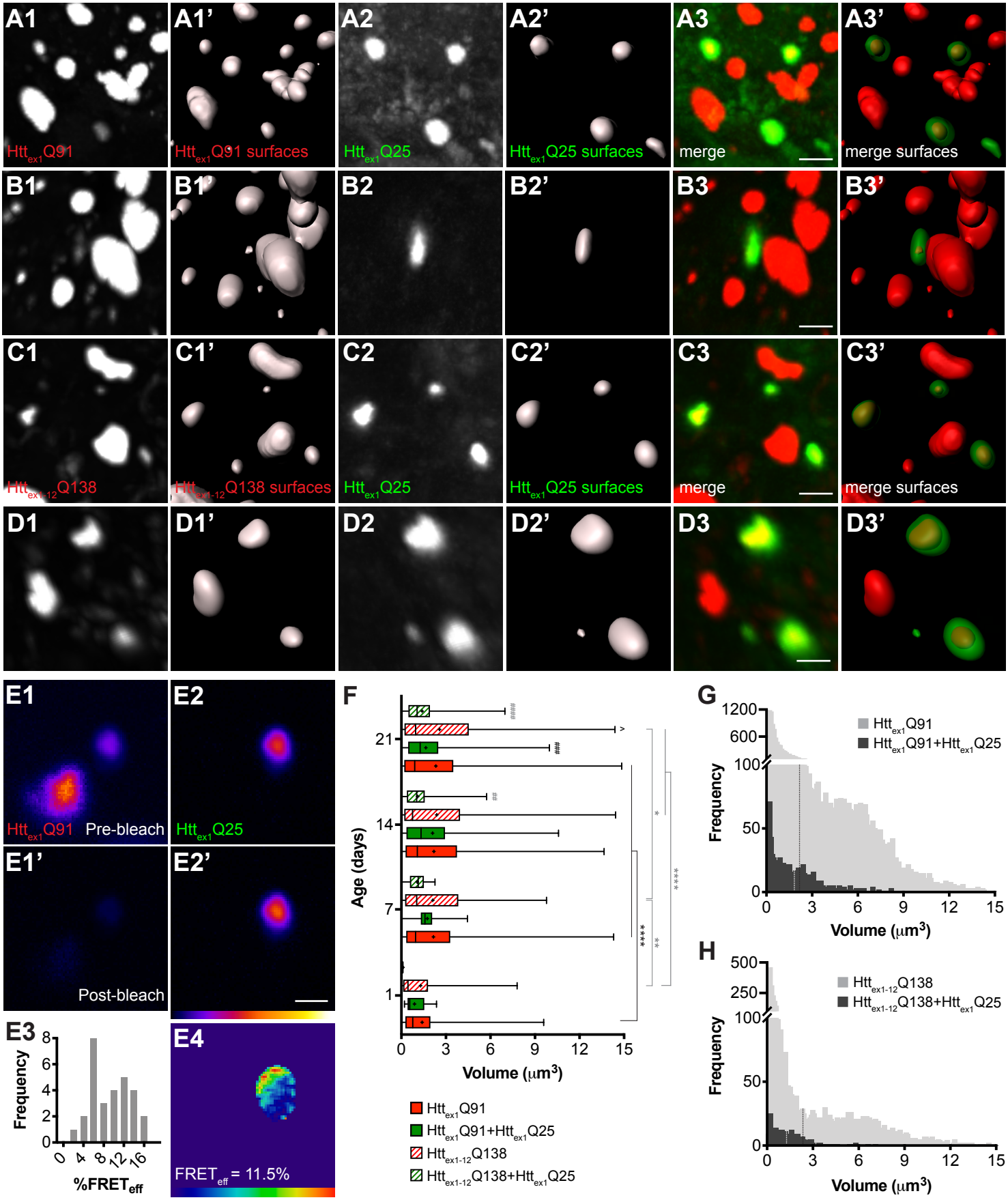
A1
Htt$_{ex1}$Q91
A1'
Htt$_{ex1}$Q91 surfaces
A2
Htt$_{ex1}$Q25
A2'
Htt$_{ex1}$Q25 surfaces
A3
merge
A3'
merge surfaces
B1
B1'
B2
B2'
B3
B3'
C1
Htt$_{ex1-12}$Q138
C1'
Htt$_{ex1-12}$Q138 surfaces
C2
Htt$_{ex1}$Q25
C2'
Htt$_{ex1}$Q25 surfaces
C3
merge
C3'
merge surfaces
D1
D1'
D2
D2'
D3
D3'
E1
Htt$_{ex1}$Q91 Pre-bleach
E2
Htt$_{ex1}$Q25
E1'
Post-bleach
E2'
E3
Frequency
%FRET$_{eff}$
E4
FRET$_{eff}$ = 11.5%
F
Age (days)
Volume (µm^3)
Htt$_{ex1}$Q91
Htt$_{ex1}$Q91+Htt$_{ex1}$Q25
Htt$_{ex1-12}$Q138
Htt$_{ex1-12}$Q138+Htt$_{ex1}$Q25
G
Frequency
Volume (µm^3)
Htt$_{ex1}$Q91
Htt$_{ex1}$Q91+Htt$_{ex1}$Q25
H
Frequency
Volume (µm^3)
Htt$_{ex1-12}$Q138
Htt$_{ex1-12}$Q138+Htt$_{ex1}$Q25

Figure 2. wtHtt$_{ex1}$ aggregates in postsynaptic PNs are nucleated by mHtt$_{ex1}$ or mHtt$_{ex1-12}$ aggregates from presynaptic ORNs. (A-D) High-magnification confocal z-stacks of DA1 glomeruli from adult flies expressing Htt$_{ex1}$Q91-mCherry (A and B) or RFP-Htt$_{ex1-12}$Q138 (C and D) in DA1 ORNs and Htt$_{ex1}$Q25-GFP in GH146+ PNs. Raw data (A1-3, B1-3, C1-3, D1-3) are shown adjacent to surfaces identified by 3D segmentation of the red (A1', B1', C1', D1') or green (A2', B2', C2', D2') channels. Htt$_{ex1}$Q25-GFP surfaces are shown at 50% transparency in "merged surfaces" images (A3', B3', C3', D3') for visibility of co-localized Htt$_{ex1}$Q91-mCherry or RFP-Htt$_{ex1-12}$Q138 surfaces. Scale bars = 1 μm. (E1-4) A single confocal slice through the center of a Htt$_{ex1}$Q91+Htt$_{ex1}$Q25 aggregate before (E1, E2) and after (E1', E2') mCherry acceptor photobleaching. Data are shown as a heat map to highlight changes in fluorescence intensities after photobleaching. Scale bar = 1 μm. FRET efficiency (FRET$_{eff}$) for this aggregate is shown in (E4), and average FRET$_{eff}$ values for all Htt$_{ex1}$Q91+Htt$_{ex1}$Q25 aggregates tested are shown in (E3). (F) Volumes of Htt$_{ex1}$Q91 (*solid red boxes*), Htt$_{ex1}$Q91+Htt$_{ex1}$Q25 (*solid green boxes*), Htt$_{ex1-12}$Q138 (*striped red boxes*), and Htt$_{ex1-12}$Q138+Htt$_{ex1}$Q25 (*striped green boxes*) aggregates identified in the DA1 glomerulus at the indicated ages. Box widths indicate interquartile ranges, vertical lines inside each box indicate medians, whiskers indicate minimums/maximums, and "+"s indicate means for each data set. *$p < 0.05$, **$p < 0.01$, ***$p < 0.001$, ****$p < 0.0001$ by one-way ANOVA followed by Tukey's multiple comparisons test. Statistical significance is indicated by "*"s when comparing the same aggregate sub-population at different ages (Htt$_{ex1}$Q91 surfaces in black and Htt$_{ex1-12}$Q138 surfaces in gray), by "#"s when comparing Htt$_{ex1}$Q91 vs Htt$_{ex1}$Q91+Htt$_{ex1}$Q25 (black) or Htt$_{ex1-12}$Q138 vs Htt$_{ex1-12}$Q138+Htt$_{ex1}$Q25 (gray) aggregates at the same ages, and by "^"s when comparing Htt$_{ex1}$Q91 vs Htt$_{ex1-12}$Q138 aggregates at the same ages. (G and H) Distribution of volumes for (G) Htt$_{ex1}$Q91 (*light gray bars*) and Htt$_{ex1}$Q91+Htt$_{ex1}$Q25 (*dark gray bars*) or (H) Htt$_{ex1-12}$Q138 (*light gray bars*) and Htt$_{ex1-12}$Q138+Htt$_{ex1}$Q25 (*dark gray bars*) aggregates, combined from 7, 14, and 21 day-old flies. Mean volume of Htt$_{ex1}$Q91 or Htt$_{ex1-12}$Q138 aggregates and Htt$_{ex1}$Q91+Htt$_{ex1}$Q25 or Htt$_{ex1-12}$Q138+Htt$_{ex1}$Q25 aggregates are indicated by black and white dotted lines, respectively, on each histogram.

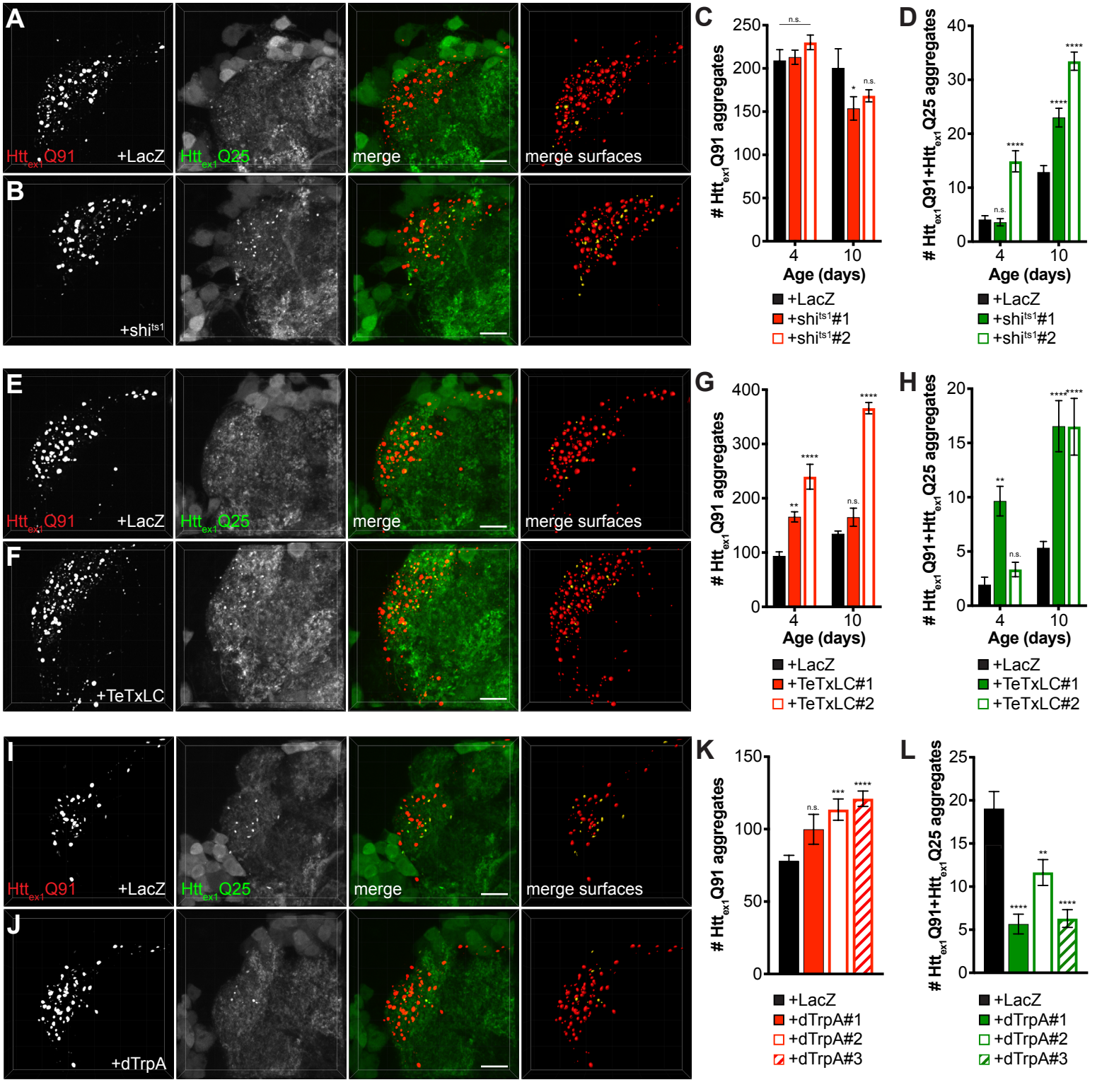
A
Htt$_{ex1}$Q91
+LacZ
Htt$_{ex1}$Q25
merge
merge surfaces
B
+shi^{ts1}
C
Htt$_{ex1}$Q91 aggregates
Age (days)
+LacZ
+shi^{ts1}#1
+shi^{ts1}#2
D
Htt$_{ex1}$Q91+Htt$_{ex1}$Q25 aggregates
E
F
+TeTxLC
G
+TeTxLC#1
+TeTxLC#2
H
I
J
+dTrpA
K
+dTrpA#1
+dTrpA#2
+dTrpA#3
L

Figure 3. $mHtt_{ex1}$ aggregate transfer from ORNs to synaptically-connected PNs is inversely correlated with presynaptic activity. (A-B, E-F, and I-J) Confocal z-stacks of DA1 glomeruli from 10 day-old males (A-B and E-F) or 7 day-old females (I-J) co-expressing Htt_{ex1}Q91-mCherry with either LacZ (A, E, and I), shi^{ts1} (B), TeTxLC (F), or dTrpA (J) in DA1 ORNs and Htt_{ex1}Q25-GFP in GH146+ PNs. In (A-B), flies were raised at the permissive temperature (18°C) and shifted to the restrictive temperature (31°C) upon eclosion, and in (I-J), flies were raised at room temperature (~21°C) and shifted to 31°C upon eclosion. mCherry+ surfaces identified by semi-automated image segmentation are shown in the last panels, with Htt_{ex1}Q91-only surfaces in red and Htt_{ex1}Q91+Htt_{ex1}Q25 surfaces in yellow. Scale bars = 10 μm. (C-D, G-H, and K-L) Quantification of Htt_{ex1}Q91 (C, G, and K) and Htt_{ex1}Q91+Htt_{ex1}Q25 (D, H, and L) aggregates identified in DA1 glomeruli from adult males of the indicated ages co-expressing Htt_{ex1}Q91-mCherry with LacZ or shi^{ts1} using two independent *QUAS-shi^{ts1}* lines in DA1 ORNs and Htt_{ex1}Q25-GFP in GH146+ PNs (C-D), adult males of the indicated ages co-expressing Htt_{ex1}Q91-mCherry with LacZ or TeTxLC using two independent *QUAS-TeTxLC* lines in DA1 ORNs and Htt_{ex1}Q25-GFP in GH146+ PNs (G-H), and 7 day-old females expressing Htt_{ex1}Q91-mCherry with either LacZ or dTrpA using three independent *QUAS-dTrpA* lines in DA1 ORNs and Htt_{ex1}Q25-GFP in GH146+ PNs (K-L). Data are shown as mean ± SEM; *$p < 0.05$, **$p < 0.01$, ***$p < 0.001$, ****$p < 0.0001$, n.s. = not significant by one- or two-way ANOVA with Tukey's multiple comparisons test comparing shi^{ts1}-, TeTxLC-, or dTrpA-expressing flies to their respective controls expressing LacZ.

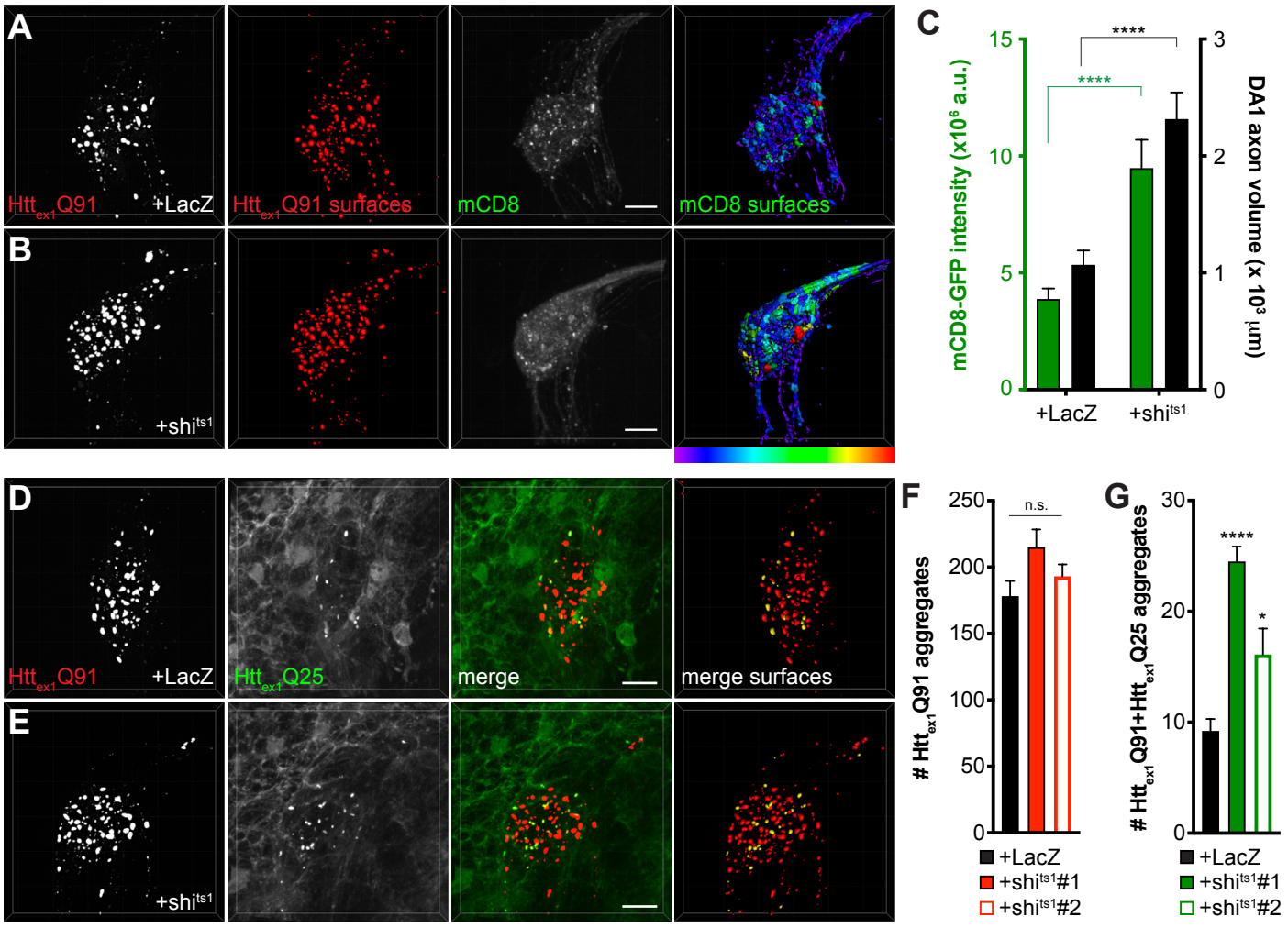

Figure 4. Inhibiting Shibire-mediated endocytosis increases mHtt$_{ex1}$-expressing ORN axon volume and enhances transfer of mHtt$_{ex1}$ aggregates from DA1 ORN axons to glia. (A and B) Confocal z-stacks of DA1 glomeruli from 10 day-old females co-expressing Htt$_{ex1}$Q91-mCherry, mCD8-GFP, and either LacZ (A) or shi^{ts1} (B) in DA1 ORNs. Flies were shifted from the permissive temperature (18°C) to the restrictive temperature (31°C) upon eclosion. Raw data are shown in grayscale, and 3D segmented surfaces are shown in red for Htt$_{ex1}$Q91 and as a heat map for mCD8-GFP to highlight differences in intensity between the genotypes. Scale bars = 10 μm. (C) Quantification of mCD8-GFP intensity (*left y-axis, green*) and volume (*right y-axis, black*) of DA1 glomeruli from 10 day-old adult females co-expressing LacZ or shi^{ts1} with Htt$_{ex1}$Q91-mCherry and mCD8-GFP in DA1 ORNs. a.u. = arbitrary units. Data are shown as mean ± SEM; ****$p < 0.0001$ by Student's *t*-test. (D and E) Confocal z-stacks of DA1 glomeruli from 5-6 day-old males expressing Htt$_{ex1}$Q91-mCherry with either LacZ (D) or shi^{ts1} (E) in DA1 ORNs and Htt$_{ex1}$Q25-YFP in repo+ glia. Adult flies were shifted from 18°C to 31°C upon eclosion. mCherry+ surfaces identified by semi-automated image segmentation are shown in the last panels, with Htt$_{ex1}$Q91-only surfaces in red and Htt$_{ex1}$Q91+Htt$_{ex1}$Q25 surfaces in yellow. Scale bars = 10 μm. (F and G) Quantification of Htt$_{ex1}$Q91 (F) and Htt$_{ex1}$Q91+Htt$_{ex1}$Q25 (G) aggregates in DA1 glomeruli of 5-6 day-old males expressing LacZ or shi^{ts1} using two independent *QUAS-shi^{ts1}* lines. Data are shown as mean ± SEM; *$p < 0.05$, ****$p < 0.0001$ by one-way ANOVA with Tukey's multiple comparisons test comparing shi^{ts1}-expressing flies to control flies expressing LacZ.

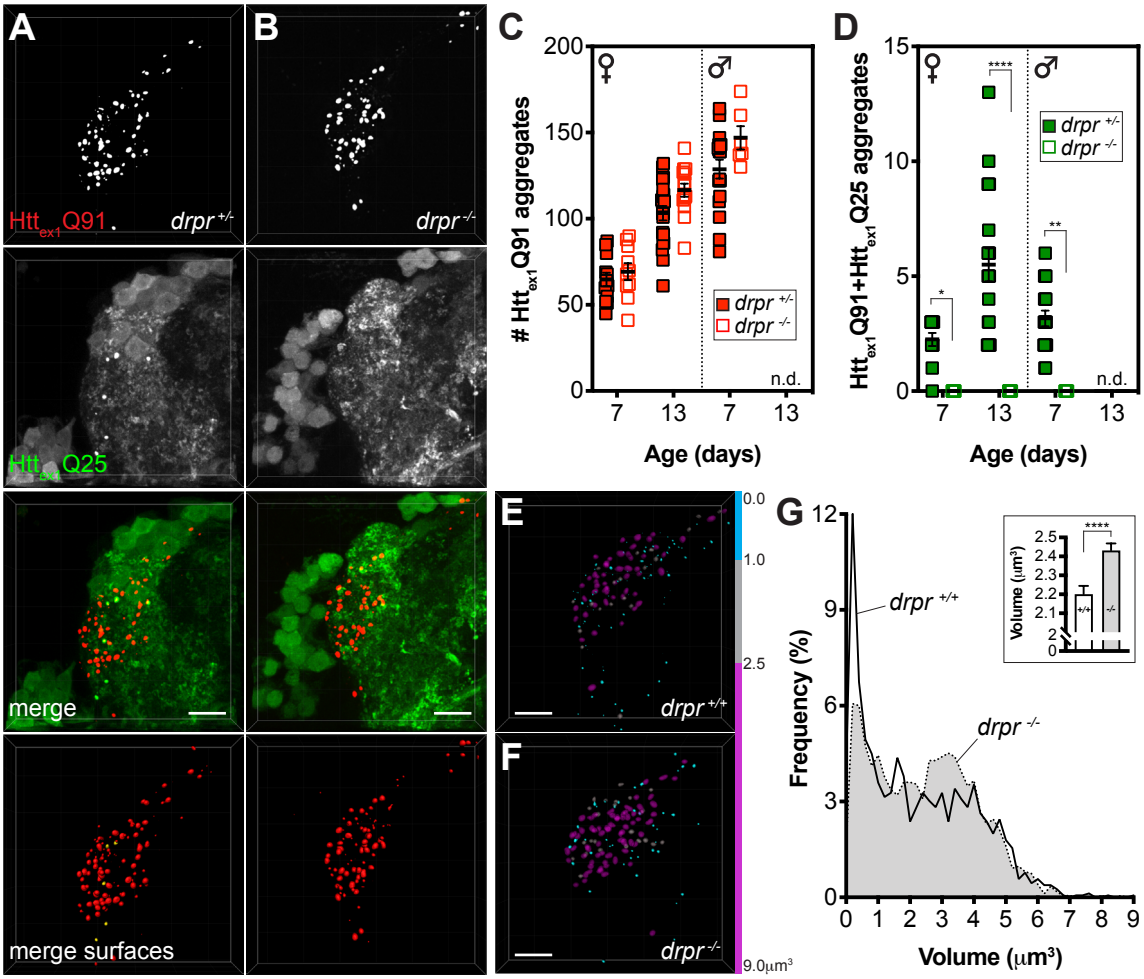

Figure 5. Draper mediates mHtt$_{ex1}$ aggregate transfer from presynaptic DA1 ORNs to postsynaptic PNs and regulates neuronal mHtt$_{ex1}$ aggregate size. (A and B) Confocal z-stacks of DA1 glomeruli from 13 day-old adult females expressing Htt$_{ex1}$Q91-mCherry in DA1 ORNs and Htt$_{ex1}$Q25-GFP in GH146+ PNs, either heterozygous (A; *drpr*$^{+/-}$) or homozygous (B; *drpr*$^{-/-}$) for the *drpr*$^{\Delta 5}$ null allele. mCherry+ surfaces identified by semi-automated image segmentation are shown in the last row, with Htt$_{ex1}$Q91-only surfaces in red and Htt$_{ex1}$Q91+Htt$_{ex1}$Q25 surfaces in yellow. Scale bars = 10 μm. (C and D) Quantification of Htt$_{ex1}$Q91 (C) and Htt$_{ex1}$Q91+Htt$_{ex1}$Q25 (D) aggregates in DA1 glomeruli from female or male *drpr*$^{+/-}$ or *drpr*$^{-/-}$ flies at the indicated ages. Data are shown as mean ± SEM; *p < 0.05, **p < 0.01, ****p < 0.0001 by two-way ANOVA with Sidak's multiple comparisons test for *drpr*$^{+/-}$ vs. *drpr*$^{-/-}$ flies at the same ages. "n.d." = not determined; 13 day-old *drpr*$^{-/-}$ males were not viable. (E and F) Htt$_{ex1}$Q91 surfaces identified in DA1 glomeruli from 7 day-old *drpr*$^{+/+}$ or *drpr*$^{-/-}$ females expressing Htt$_{ex1}$Q91-mCherry in DA1 ORNs. Htt$_{ex1}$Q91 aggregates are color-coded according to the following volume ranges: cyan = 0-1.0 μm^3; gray = 1.01-2.49 μm^3; magenta = 2.5-9.0 μm^3. Gray and magenta surfaces were set to 70% transparency to improve visibility of smaller cyan surfaces. Scale bars = 10 μm. (G) Relative frequency of volumes for all Htt$_{ex1}$Q91 aggregates identified in 7 day-old *drpr*$^{+/+}$ (*solid line*) or *drpr*$^{-/-}$ (*dotted line; gray shading*) males and females. The inset graph shows mean Htt$_{ex1}$Q91 aggregate volume ± SEM for the two genotypes. ****p < 0.0001 by unpaired Student's *t*-test.

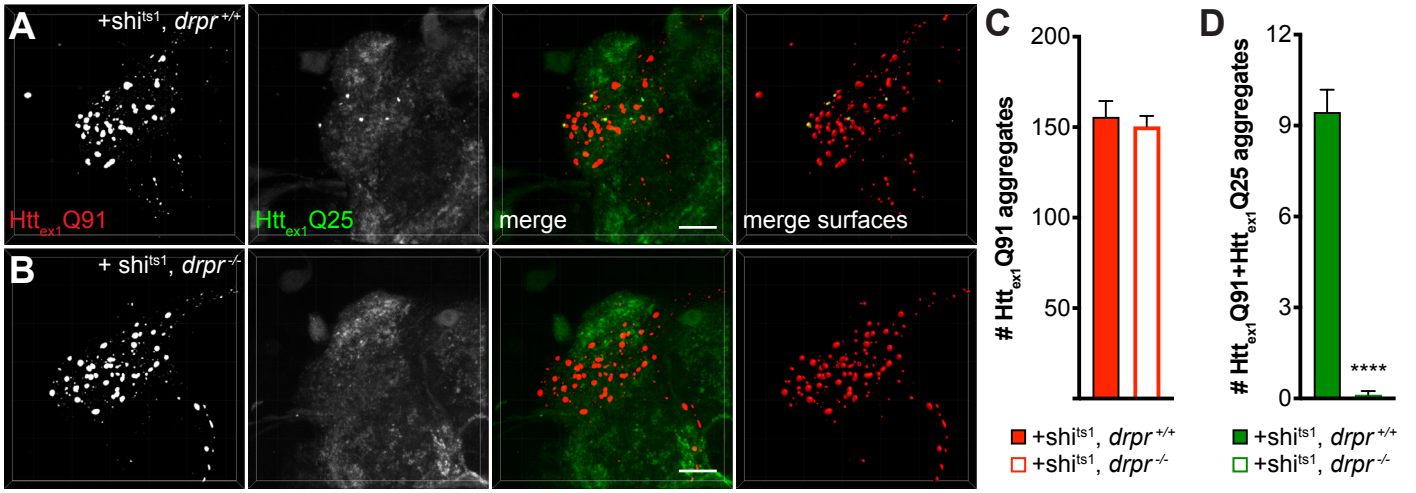

Figure 5 – figure supplement 1. Draper is required for enhanced transfer of mHtt$_{ex1}$ from shi^{ts1}-expressing DA1 ORNs to GH146+ PNs. (A and B) Confocal z-stacks of DA1 glomeruli from 7 day-old *drpr*$^{+/+}$ (A) or *drpr*$^{-/-}$ (B) adult females co-expressing Htt$_{ex1}$Q91-mCherry with shi^{ts1} in DA1 ORNs and Htt$_{ex1}$Q25-GFP in GH146+ PNs. Adult flies were shifted from 18°C to 31°C upon eclosion. mCherry+ surfaces identified by semi-automated image segmentation are shown in the last panels, with Htt$_{ex1}$Q91-only surfaces in red and Htt$_{ex1}$Q91+Htt$_{ex1}$Q25 surfaces in yellow. Scale bars = 10 μm. (C and D) Quantification of Htt$_{ex1}$Q91 (C) and Htt$_{ex1}$Q91+Htt$_{ex1}$Q25 (D) aggregates for the same genotypes shown in (A and B). Data are shown as mean ± SEM; ****$p < 0.0001$ by Student's *t*-test comparing *drpr*$^{+/+}$ vs *drpr*$^{-/-}$ flies.

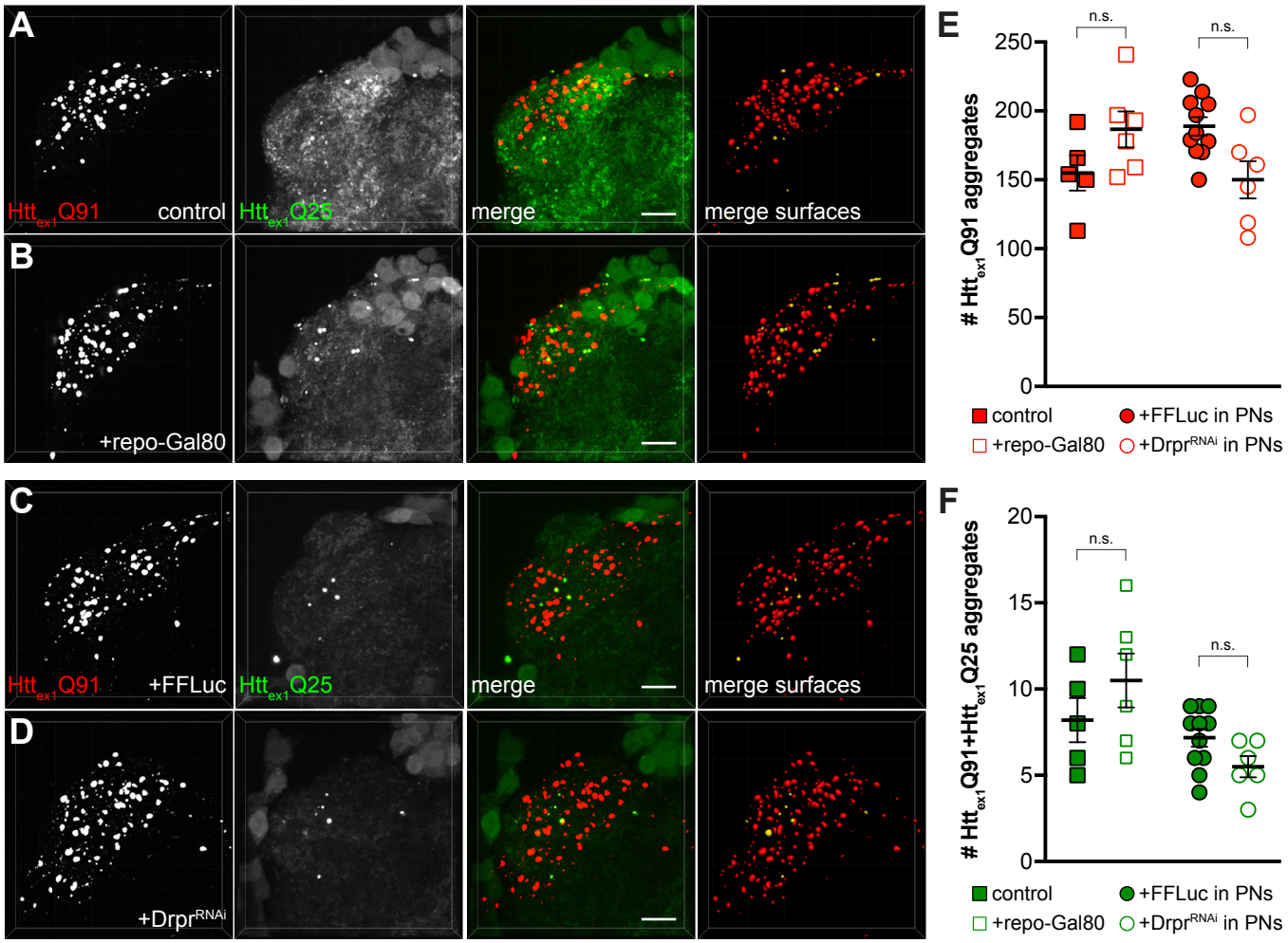

Figure 5 – figure supplement 2. Gal80-mediated repression of Gal4 in glia or RNAi knockdown of *drpr* in PNs do not alter ORN-to-PN prion-like transfer of mHtt$_{ex1}$ aggregates. (A and B) Confocal z-stacks of DA1 glomeruli from 10-14 day-old adult males expressing Htt$_{ex1}$Q91-mCherry in DA1 ORNs and Htt$_{ex1}$Q25-GFP in GH146+ PNs with (A) no additional transgenes ("control") or (B) *repo-Gal80* to inhibit *Gal4*-mediated expression of Htt$_{ex1}$Q25-GFP in glia. (C and D) Confocal z-stacks of DA1 glomeruli from 14 day-old adult males expressing Htt$_{ex1}$Q91-mCherry in DA1 ORNs and co-expressing Htt$_{ex1}$Q25-GFP together with firefly luciferase (FFLuc; C) or dsRNA targeting *draper* (Drpr^{RNAi}; D) in GH146+ PNs. In (A-D), mCherry+ surfaces identified by semi-automated image segmentation are shown in the last panels, with Htt$_{ex1}$Q91-only surfaces in red and Htt$_{ex1}$Q91+Htt$_{ex1}$Q25 surfaces in yellow. Scale bars = 10 μm. (E and F) Quantification of Htt$_{ex1}$Q91 (E) and Htt$_{ex1}$Q91+Htt$_{ex1}$Q25 (F) aggregates for genotypes shown in (A-D). Data are shown as mean ± SEM; n.s. = not significant by one-way ANOVA with Tukey's multiple comparisons tests.

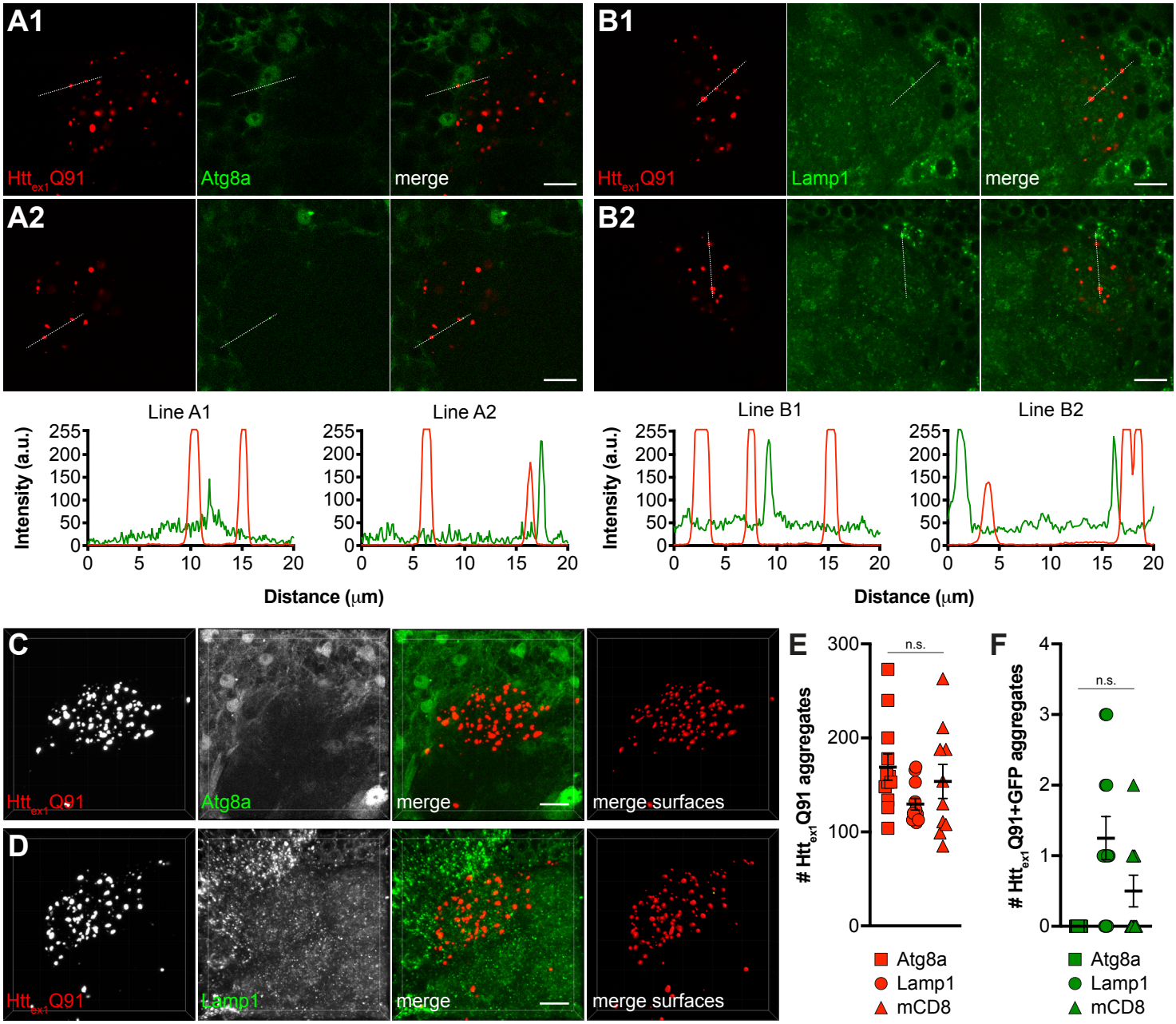

Figure 5 – figure supplement 3. mHtt$_{ex1}$ aggregates generated in ORNs do not co-localize with markers of lysosomes or autophagosomes in glia. (A1-2 and B1-2) Single confocal slices from DA1 glomeruli of 4-5 day-old adult males expressing Htt$_{ex1}$Q91-mCherry in DA1 ORNs and either the autophagosomal marker Atg8a-GFP (A1 and A2) or the lysosomal marker GFP-Lamp1 (B1 and B2) in repo+ glia. Scale bars = 10 μm. Htt$_{ex1}$Q91-mCherry (*red*) and Atg8a- or Lamp1-GFP (*green*) fluorescence intensity profiles for lines indicated in (A1-2 and B1-2) are shown below images; a.u. = arbitrary units. Lines were scanned from leftmost to rightmost point. (C and D) Confocal z-stacks of DA1 glomeruli from 4-5 day-old adult males expressing Htt$_{ex1}$Q91-mCherry in DA1 ORNs and either Atg8a-GFP (C) or GFP-Lamp1 (D) in repo+ glia. mCherry+ surfaces identified by semi-automated image segmentation are shown in the last panels, with Htt$_{ex1}$Q91-only surfaces in red and Htt$_{ex1}$Q91+GFP surfaces in yellow. Scale bars = 10 μm. (E and F) Quantification of Htt$_{ex1}$Q91 (E) and Htt$_{ex1}$Q91+GFP (F) surfaces for the same genotypes as in (C and D) and for control animals expressing mCD8-GFP in glia. Data are shown as mean ± SEM; n.s. = not significant by one-way ANOVA with Tukey's multiple comparisons test.

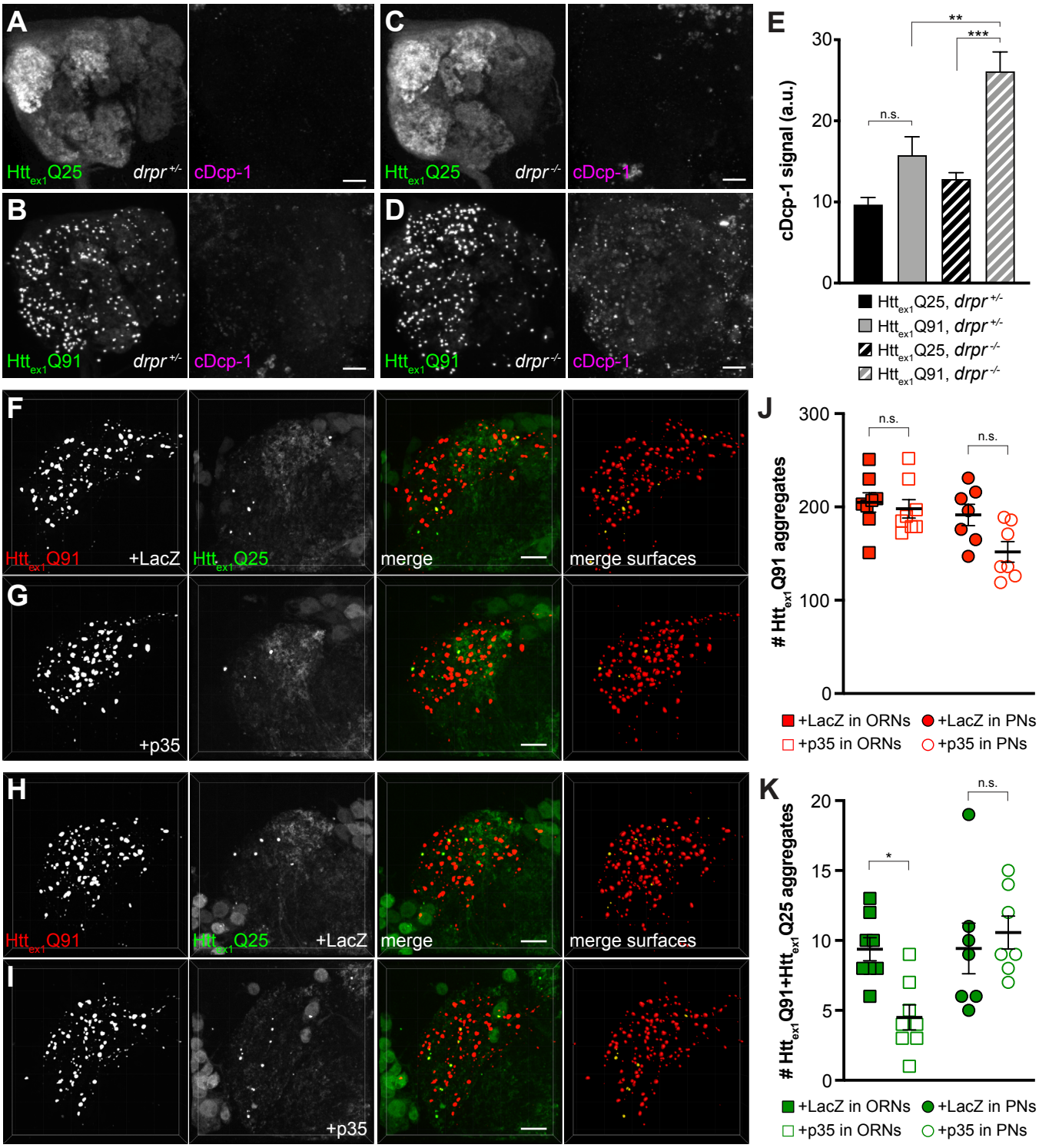
A
Htt$_{ex1}$Q25
drpr$^{+/-}$
cDcp-1
B
Htt$_{ex1}$Q91
drpr$^{+/-}$
cDcp-1
C
Htt$_{ex1}$Q25
drpr$^{-/-}$
cDcp-1
D
Htt$_{ex1}$Q91
drpr$^{-/-}$
cDcp-1
E
cDcp-1 signal (a.u.)
0
10
20
30
n.s.
**
***
Htt$_{ex1}$Q25, drpr$^{+/-}$
Htt$_{ex1}$Q91, drpr$^{+/-}$
Htt$_{ex1}$Q25, drpr$^{-/-}$
Htt$_{ex1}$Q91, drpr$^{-/-}$
F
Htt$_{ex1}$Q91
+LacZ
Htt$_{ex1}$Q25
merge
merge surfaces
G
+p35
J
Htt$_{ex1}$Q91 aggregates
0
100
200
300
n.s.
n.s.
+LacZ in ORNs
+LacZ in PNs
+p35 in ORNs
+p35 in PNs
H
Htt$_{ex1}$Q91
Htt$_{ex1}$Q25
+LacZ
merge
merge surfaces
I
+p35
K
Htt$_{ex1}$Q91+Htt$_{ex1}$Q25 aggregates
0
5
10
15
20
*
n.s.
+LacZ in ORNs
+LacZ in PNs
+p35 in ORNs
+p35 in PNs

Figure 6. Caspase activation in ORNs mediates mHtt$_{ex1}$ aggregate transfer from ORNs to PNs. (A-D) Maximum-intensity projections of antennal lobes from 8 day-old adult males expressing Htt$_{ex1}$Q25-GFP (A and C) or Htt$_{ex1}$Q91-GFP (B and D) in most ORNs using *Or83b-Gal4* in *drpr*$^{\Delta 5}$ heterozygotes (*drpr*$^{+/-}$; A and B) or homozygotes (*drpr*$^{-/-}$; C and D). Brains were immunostained for GFP (*left panels*) or cleaved Dcp-1 (*right panels*). Scale bars = 20 μm. (E) Quantification of cDcp-1 immunofluorescence from 8 day-old adult males with the same genotypes as in (A-D). Data are shown as mean ± SEM; **$p < 0.01$, ***$p < 0.001$, n.s. = not significant by one-way ANOVA with Tukey's multiple comparisons test. (F-I) Confocal z-stacks of DA1 glomeruli from 14 day-old males expressing Htt$_{ex1}$Q91-mCherry with LacZ (F) or p35 (G) in DA1 ORNs and Htt$_{ex1}$Q25-GFP in GH146+ PNs, or Htt$_{ex1}$Q91-mCherry in DA1 ORNs and Htt$_{ex1}$Q25-GFP with LacZ (H) or p35 (I) in GH146+ PNs. mCherry+ surfaces identified by 3D segmentation are shown in the last panels, with Htt$_{ex1}$Q91-only surfaces in red and Htt$_{ex1}$Q91+Htt$_{ex1}$Q25 surfaces in yellow. Scale bars = 10 μm. (J and K) Quantification of Htt$_{ex1}$Q91 (J) or Htt$_{ex1}$Q91+Htt$_{ex1}$Q25 (K) aggregates in DA1 glomeruli of flies with the same genotypes in (F and G) (*squares*) or (H and I) (*circles*). Numbers of aggregates in flies expressing LacZ or p35 are indicated by solid or open shapes, respectively. Data are shown as mean ± SEM; *$p < 0.05$, n.s. = not significant by one-way ANOVA with Tukey's multiple comparisons test.

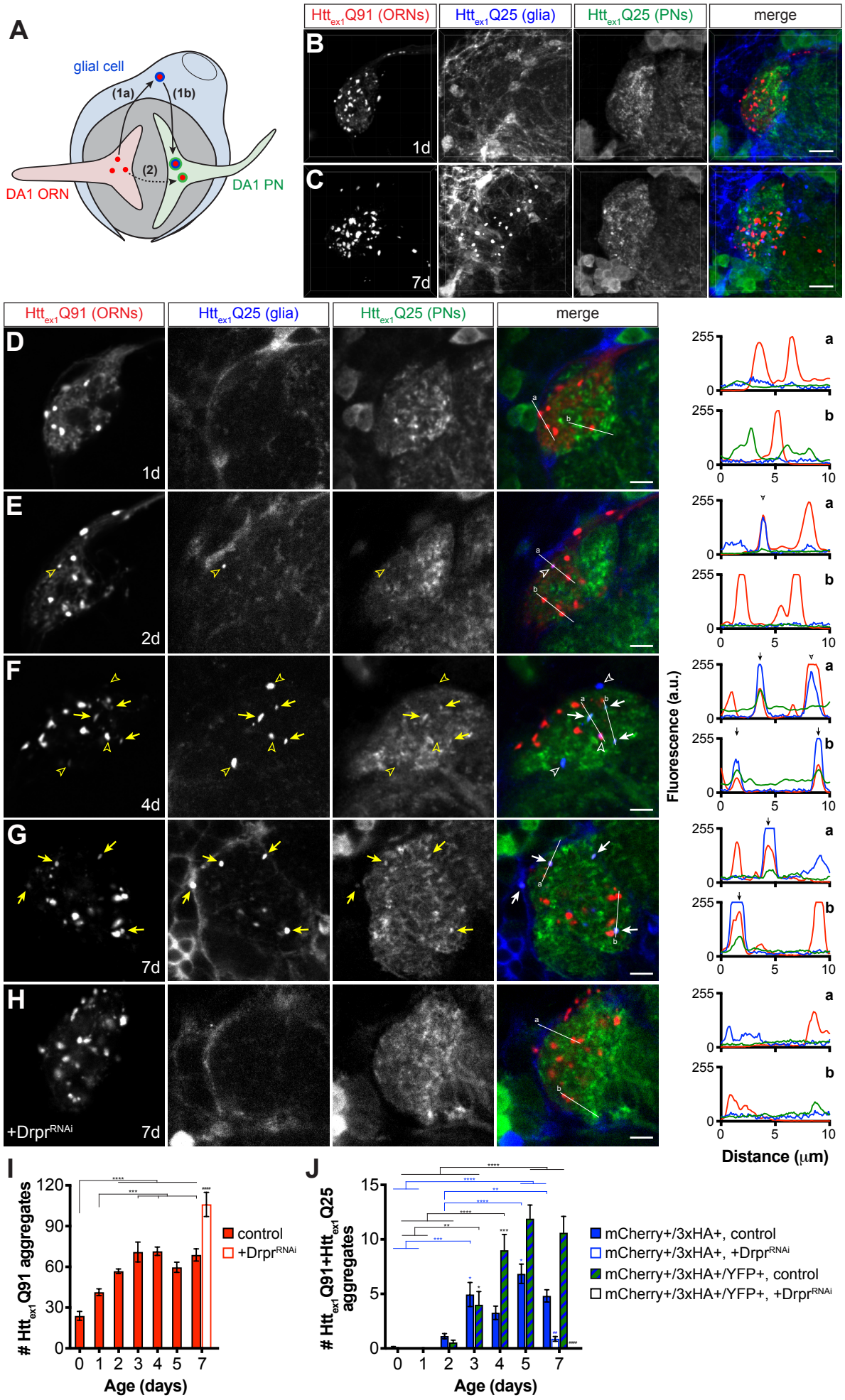
A
glial cell
(1a)
(1b)
(2)
DA1 ORN
DA1 PN
Htt$_{ex1}$Q91 (ORNs)
Htt$_{ex1}$Q25 (glia)
Htt$_{ex1}$Q25 (PNs)
merge
B
1d
C
7d
D
1d
E
2d
F
4d
G
7d
H
+Drpr^{RNAi}
7d
Fluorescence (a.u.)
Distance (μm)
I
Htt$_{ex1}$Q91 aggregates
control
+Drpr^{RNAi}
Age (days)
J
Htt$_{ex1}$Q91+Htt$_{ex1}$Q25 aggregates
mCherry+/3xHA+, control
mCherry+/3xHA+, +Drpr^{RNAi}
mCherry+/3xHA+/YFP+, control
mCherry+/3xHA+/YFP+, +Drpr^{RNAi}
Age (days)

Figure 7. $mHtt_{ex1}$ aggregates transfer from presynaptic ORNs to postsynaptic PNs via the cytoplasm of phagocytic glia. (A) Diagram illustrating our experimental approach for examining a role for Draper-expressing glia in $mHtt_{ex1}$ aggregate transfer from DA1 ORNs to DA1 PNs. Flies that combined *Or67d-QF*-, *repo-Gal4*-, and *GH146-LexA:GAD*-driven expression of Htt_{ex1}Q91-mCherry in DA1 ORNs, Htt_{ex1}Q25-3xHA in all glia, and Htt_{ex1}Q25-YFP in ~60% of PNs, respectively, were generated and analyzed by confocal microscopy of immunostained brains. If Htt_{ex1}Q91-mCherry aggregates travel to PNs via the glial cytoplasm (route 1), triple-labeled (mCherry+/3xHA+/YFP+) aggregates should be observed. By contrast, if Htt_{ex1}Q91-mCherry aggregates transfer directly to PNs without accessing the glial cytoplasm (route 2), then only double-labeled (mCherry+/3xHA+ and mCherry+/YFP+) aggregates would be detected. (B-C) Confocal z-stacks of DA1 glomeruli from adult females of the indicated ages expressing Htt_{ex1}Q91-mCherry in DA1 ORNs (*red*), Htt_{ex1}Q25-3xHA in glia (*blue*), and Htt_{ex1}Q25-YFP in PNs (*green*) at the indicated ages. Brains were immunostained with antibodies against the mCherry, 3xHA, and YFP tags unique to each Htt protein. Scale bars = 10 μm. (D-H) Single 0.35 μm confocal z-slices from females of the indicated ages with (D-G) the same genotype as in (B and C) or (H) also expressing dsRNA targeting *drpr* (+$Drpr^{RNAi}$). Colocalizing mCherry+/3xHA+ or mCherry+/3xHA+/YFP+ aggregates are indicated by open arrowheads or arrows, respectively, shown in yellow on grayscale and white on merged images for increased visibility. Scale bars = 5 μm. Htt_{ex1}Q91-mCherry (*red*), Htt_{ex1}Q25-3xHA (*blue*), and Htt_{ex1}Q25-YFP (*green*) fluorescence intensity profiles for lines “a” and “b” are shown to the right of each merged image. Lines were scanned from leftmost to rightmost point. Arrowheads and arrows on plots indicate peak mCherry fluorescence in colocalized mCherry+/3xHA+ and mCherry+/3xHA+/YFP+ aggregates, respectively. (I and J) Quantification of (I) mCherry-only or (J) mCherry+/3xHA+ and mCherry+/3xHA+/YFP+ aggregates identified in control (*solid bars*) or $Drpr^{RNAi}$-expressing (*open bars*) animals over time. +$Drpr^{RNAi}$ animals were only analyzed at 7 days-old. Data are shown as mean ± SEM; *$p < 0.05$, **$p < 0.01$, ***$p < 0.001$, or ****$p < 0.0001$ by one- or two-way ANOVA followed by Tukey’s multiple comparisons test. *s indicate statistical significance comparing control flies at different ages [black *s compare mCherry-only aggregates in (I) and mCherry+/3xHA+/YFP+ aggregates in (J), and blue *s compare mCherry+/3xHA+ aggregates in (J)], and blue and black #s indicate statistical significance comparing mCherry+/3xHA+ or mCherry+/3xHA+/YFP+ aggregates, respectively, in control vs $Drpr^{RNAi}$-expressing flies at the same age.

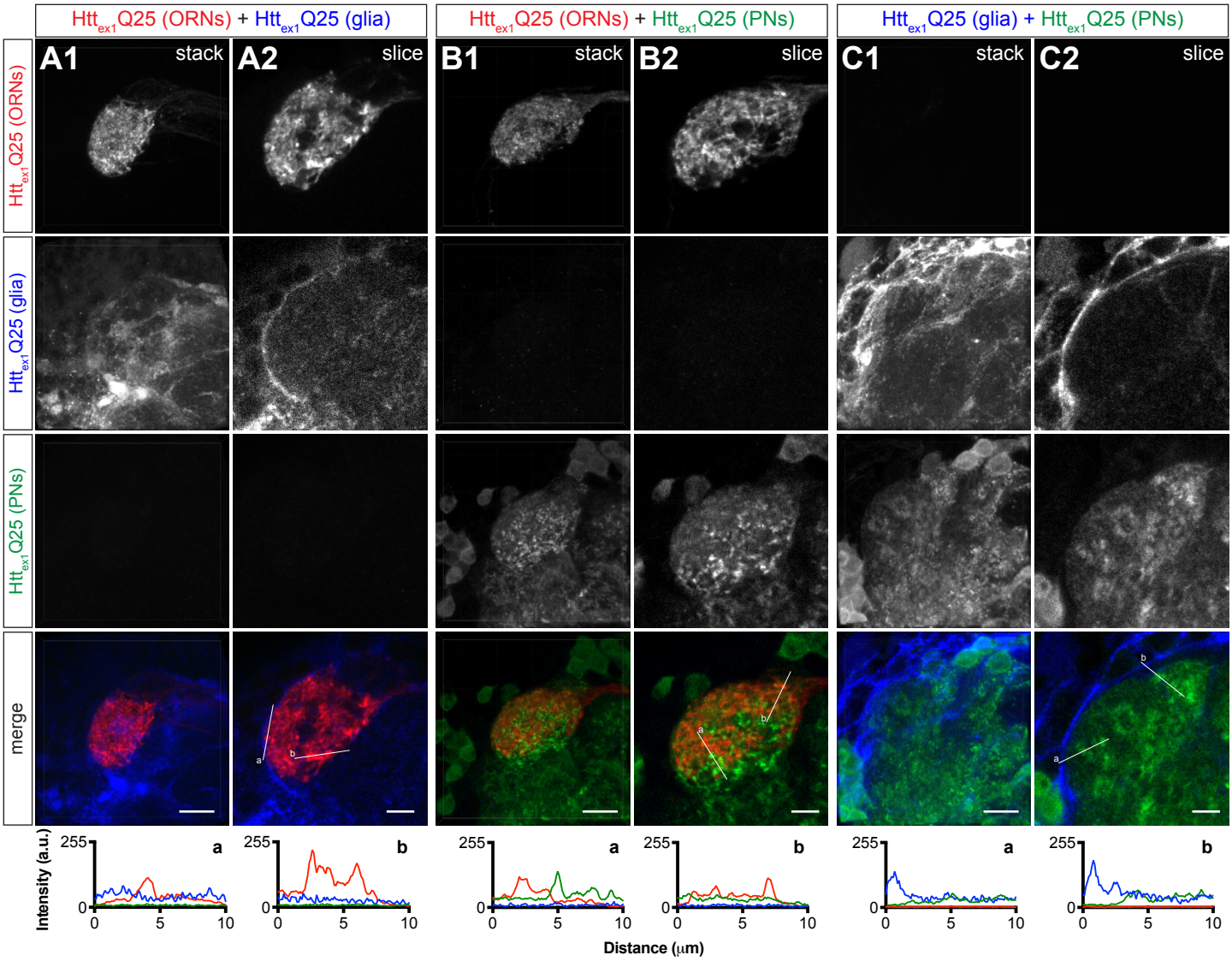

Figure 7 - figure supplement 1. Controls for monitoring transmission of mHtt$_{ex1}$ aggregates from presynaptic DA1 ORNs to postsynaptic PNs via a glial intermediate. (A-C) Confocal z-stacks (A1, B1, and C1) and single 0.35 μm z-slices (A2, B2, and C2) of DA1 glomeruli from 4-6 day-old adult females expressing (A1-2) Htt$_{ex1}$Q25-mCherry in DA1 ORNs and Htt$_{ex1}$Q25-3xHA in repo+ glia, (B1-2) Htt$_{ex1}$Q25-mCherry in DA1 ORNs and Htt$_{ex1}$Q25-YFP in GH146+ PNs, or (C1-2) Htt$_{ex1}$Q25-3xHA in repo+ glia and Htt$_{ex1}$Q25-YFP in GH146+ PNs. All brains were immunostained with antibodies against all three epitope tags (i.e., mCherry, YFP, and 3xHA) to show specific staining. Scale bars = 10 μm in (A1, B1, and C1) and 5 μm in (A2, B2, and C2). Htt$_{ex1}$Q25-mCherry (*red*), Htt$_{ex1}$Q25-3xHA (*blue*), and Htt$_{ex1}$Q25-YFP (*green*) fluorescence intensity profiles for lines “a” and “b” shown in merged slices (A2, B2, and C2) are shown below images. Lines were scanned from leftmost to rightmost point.

Table. Genotypes and sample sizes displayed in each figure

Figure	Genotype	Sample size (*n*) on graphs
Figure 1		
C	*Or67d-QF,UAS-Htt$_{ex1}$Q25-GFP^{attP3}/(+/Y) ; GH146-Gal4/QUAS-Htt$_{ex1}$Q25-mCherry^{attP24}*	
D	*Or67d-QF,UAS-Htt$_{ex1}$Q25-GFP^{attP3}/(+/Y) ; GH146-Gal4/QUAS-Htt$_{ex1}$Q91-mCherry^{attP24}*	
E,F,G,J,K	*Or67d-QF,UAS-Htt$_{ex1}$Q25-GFP^{attP3}/(+/Y) ; GH146-Gal4,QUAS-Htt$_{ex1}$Q91-mCherry^{attP24}/+*	J,K: Htt$_{ex1}$ males - 1d (*14*), 7d (*15*), 14d (*20*), 21d (*14*) J,K: Htt$_{ex1}$ females - 1d (*10*), 7d (*10*), 14d (*17*), 21d (*18*)
H,I,J,K	*Or67d-QF,UAS-Htt$_{ex1}$Q25-GFP^{attP3}/QUAS-RFP-Htt$_{ex1-12}$Q138^{attP3B} ; GH146-Gal4/+*	J,K: Htt$_{ex1-12}$ females - 1d (*10*), 7d (*12*), 14d (*14*), 21d (*20*)
Figure 1, figure supplement 1		
A,F	*elav[C155]-Gal4/UAS-Htt$_{ex1}$Q91-mCherry^{attP3}*	F: Htt$_{ex1}$Q91 - *8*
B,F	*elav[C155]-Gal4/+ ; UAS-Htt$_{ex1}$Q25-GFP^{attP24}/+*	F: Htt$_{ex1}$Q25 - *6*
C,F	*elav[C155]-Gal4/UAS-Htt$_{ex1}$Q91-mCherry^{attP3} ; UAS-Htt$_{ex1}$Q25-GFP^{attP24}/+*	F: Htt$_{ex1}$Q91 + Htt$_{ex1}$Q25 - *6*
D,F	*elav[C155]-Gal4/UAS-Htt$_{ex1}$Q91-mCherry^{attP3} ; UAS-mCD8-GFP/+*	F: Htt$_{ex1}$Q91 + mCD8 - *6*
E,F	*elav[C155]-Gal4/UAS-Htt$_{ex1}$Q91-mCherry^{attP3} ; UAS-GFP^{attP24}/+*	F: Htt$_{ex1}$Q91 + GFP - *7*
Figure 1, figure supplement 2		
A,B,C,D	*Or67d-QF,UAS-Htt$_{ex1}$Q25-GFP^{attP3}/Y ; GH146-Gal4,QUAS-Htt$_{ex1}$Q91-mCherry^{attP24}/+*	D - *14*
Figure 1, figure supplement 3		
A,E,F	*Or67d-QF,UAS-Htt$_{ex1}$Q25-GFP^{attP3}/+ ; GH146-Gal4/QUAS-Htt$_{ex1}$Q25-mCherry^{attP24}*	E,F - *6*
B,E,F	*Or67d-QF/Y ; GH146-Gal4,QUAS-Htt$_{ex1}$Q91-mCherry^{attP24}/UAS-mCD8-GFP*	E,F - *8*
C,E,F	*Or67d-QF,UAS-Htt$_{ex1}$Q25-GFP^{attP3}/QUAS-Gal80 ; GH146-Gal4/QUAS-Htt$_{ex1}$Q91-mCherry^{attP24}*	E,F: *6*
D,E,F	*Or67d-QF,UAS-Htt$_{ex1}$Q25-GFP^{attP3}/+ ; GH146-Gal4/QUAS-Htt$_{ex1}$Q91-mCherry^{attP24} ; UAS-QS/+*	E,F: *6*
Figure 1, figure supplement 4		
A1-4,B1-4,C,D	*pebbled-Gal4/QUAS-Htt$_{ex1}$Q91-mCherry^{attP3} ; UAS-Htt$_{ex1}$Q25-GFP^{attP24}/+ ; GH146-QF/+*	C,D - 7d (*5*), 14d (*5*)
Figure 2		
A,B,E,F,G	*Or67d-QF,UAS-Htt$_{ex1}$Q25-GFP^{attP3}/(+/Y) ; GH146-Gal4,QUAS-Htt$_{ex1}$Q91-mCherry^{attP24}/+*	E3 - *28* F: Htt$_{ex1}$Q91 - 1d (*1138*), 7d (*2235*), 14d (*4309*), 21d (*5435*) F: Htt$_{ex1}$Q91+Htt$_{ex1}$Q25 - 1d (*8*), 7d (*36*), 14d (*319*), 21d (*392*) G: Htt$_{ex1}$Q91 - *13,132* G: Htt$_{ex1}$Q91+Htt$_{ex1}$Q25 - *754*
C,D,F,H	*Or67d-QF,UAS-Htt$_{ex1}$Q25-GFP^{attP3}/QUAS-RFP-Htt$_{ex1-12}$Q138^{attP3B} ; GH146-Gal4/+*	F: Htt$_{ex1-12}$Q138 - 1d (*271*), 7d (*469*), 14d (*1196*), 21d (*1944*)

		F: $Htt_{ex1-12}Q138$+$Htt_{ex1}Q25$ - 1d (*1*), 7d (*16*), 14d (*73*), 21d (*175*) H: $Htt_{ex1-12}Q138$ - *3887* H: $Htt_{ex1-12}Q138$+$Htt_{ex1}Q25$ - *265*
Figure 3		
A,C,D	*Or67d-QF,UAS-$Htt_{ex1}Q25$-GFP^{attP3}/Y ; GH146-Gal4,QUAS-$Htt_{ex1}Q91$-$mCherry^{attP24}$/+ ; QUAS-nucLacZ/+*	C,D: +LacZ - 4d (*12*), 10d (*8*)
B,C,D	*Or67d-QF,UAS-$Htt_{ex1}Q25$-GFP^{attP3}/Y ; GH146-Gal4,QUAS-$Htt_{ex1}Q91$-$mCherry^{attP24}$/+; QUAS-$shibire^{ts1}$#5/+*	C,D: +shi^{ts1}#1 - 4d (*10*), 10d (*8*)
C,D	*Or67d-QF,UAS-$Htt_{ex1}Q25$-GFP^{attP3}/Y ; GH146-Gal4,QUAS-$Htt_{ex1}Q91$-$mCherry^{attP24}$/+; QUAS-$shibire^{ts1}$#7/+*	C,D: +shi^{ts1}#2 - 4d (*10*), 10d (*11*)
E,G,H	*Or67d-QF,UAS-$Htt_{ex1}Q25$-GFP^{attP3}/Y ; GH146-Gal4,QUAS-$Htt_{ex1}Q91$-$mCherry^{attP24}$/+ ; QUAS-nucLacZ/+*	G,H: +LacZ - 4d (*8*), 10d (*10*)
F,G,H	*Or67d-QF,UAS-$Htt_{ex1}Q25$-GFP^{attP3}/Y ; GH146-Gal4,QUAS-$Htt_{ex1}Q91$-$mCherry^{attP24}$/QUAS-TeTxLC#4c ; +/(Dh/Tm6b)*	G,H: +TeTxLC#1 - 4d (*10*), 10d (*9*)
G,H	*Or67d-QF,UAS-$Htt_{ex1}Q25$-GFP^{attP3}/Y ; GH146-Gal4,QUAS-$Htt_{ex1}Q91$-$mCherry^{attP24}$/Pin; QUAS-TeTxLC#9c/+*	G,H: +TeTxLC#2 - 4d (*10*), 10d (*6*)
I,K,L	*Or67d-QF,UAS-$Htt_{ex1}Q25$-GFP^{attP3}/+ ; GH146-Gal4,QUAS-$Htt_{ex1}Q91$-$mCherry^{attP24}$/+ ; QUAS-nucLacZ/+*	K,L: +LacZ - *10*
K,L	*Or67d-QF,UAS-$Htt_{ex1}Q25$-GFP^{attP3}/QUAS-dTrpA#5 ; GH146-Gal4,QUAS-$Htt_{ex1}Q91$-$mCherry^{attP24}$/+*	K,L: +TrpA#1 - *6*
J,K,L	*Or67d-QF,UAS-$Htt_{ex1}Q25$-GFP^{attP3}/+ ; GH146-Gal4,QUAS-$Htt_{ex1}Q91$-$mCherry^{attP24}$/+ ; QUAS-dTrpA#6/+*	K,L: +TrpA#2 - *11*
K,L	*Or67d-QF,UAS-$Htt_{ex1}Q25$-GFP^{attP3}/+ ; GH146-Gal4,QUAS-$Htt_{ex1}Q91$-$mCherry^{attP24}$/QUAS-dTrpA#7*	K,L: +TrpA#3 - *10*
Figure 4		
A,C	*Or67d-QF,QUAS-$Htt_{ex1}Q91$-$mCherry^{attP3}$/+ ; QUAS-mCD8-GFP/+ ; QUAS-nucLacZ/+*	C: +LacZ - *10*
B,C	*Or67d-QF,QUAS-$Htt_{ex1}Q91$-$mCherry^{attP3}$/+ ; QUAS-mCD8-GFP/+ ; QUAS-$shibire^{ts1}$#7/+*	C: +shi^{ts1} - *8*
D,F,G	*Or67d-QF,QUAS-$Htt_{ex1}Q91$-$mCherry^{attP3}$/Y ; UAS-$Htt_{ex1}Q25$-YFP^{attP24}/+ ; repo-Gal4/QUAS-nucLacZ*	F,G: +LacZ - *9*
E,F,G	*Or67d-QF,QUAS-$Htt_{ex1}Q91$-$mCherry^{attP3}$/Y ; UAS-$Htt_{ex1}Q25$-YFP^{attP24}/+ ; repo-Gal4/QUAS-$shibire^{ts1}$#7*	F,G: +shi^{ts1}#1 - *8*
F,G	*Or67d-QF,QUAS-$Htt_{ex1}Q91$-$mCherry^{attP3}$/Y ; UAS-$Htt_{ex1}Q25$-YFP^{attP24}/+ ; repo-Gal4/QUAS-$shibire^{ts1}$#5*	F,G: +shi^{ts1}#2 - *10*
Figure 5		
A,C,D	*Or67d-QF,UAS-$Htt_{ex1}Q25$-GFP^{attP3}/(+/Y) ; GH146-Gal4,QUAS-$Htt_{ex1}Q91$-$mCherry^{attP24}$/+ ; $drpr^{\Delta 5}$/+*	C,D: *$drpr^{+/-}$*, females - 7d (*12*), 13d (*20*) C,D: *$drpr^{+/-}$* males - 7d (*18*)
B,C,D	*Or67d-QF,UAS-$Htt_{ex1}Q25$-GFP^{attP3}/(+/Y) ; GH146-Gal4,QUAS-$Htt_{ex1}Q91$-$mCherry^{attP24}$/+ ; $drpr^{\Delta 5}$/$drpr^{\Delta 5}$*	C,D: *$drpr^{-/-}$* females - 7d (*10*), 13d (*13*) C,D: *$drpr^{-/-}$* males - 7d (*6*)
E,G	*Or67d-QF,QUAS-$Htt_{ex1}Q91$-$mCherry^{attP3}$/(+/Y)*	G: *$drpr^{+/+}$ - 1556*
F,G	*Or67d-QF,QUAS-$Htt_{ex1}Q91$-$mCherry^{attP3}$/(+/Y) ; ; $drpr^{\Delta 5}$/$drpr^{\Delta 5}$*	G: *$drpr^{-/-}$ - 1749*
Figure 5, figure supplement 1		
A,C,D	*Or67d-QF,UAS-$Htt_{ex1}Q25$-GFP^{attP3}/QUAS-$shibire^{ts1}$#2 ; GH146-Gal4,QUAS-$Htt_{ex1}Q91$-$mCherry^{attP24}$/+*	C,D: +shi^{ts1}, *$drpr^{+/+}$ - 11*
B,C,D	*Or67d-QF,UAS-$Htt_{ex1}Q25$-GFP^{attP3}/QUAS-$shibire^{ts1}$#2 ; GH146-Gal4,QUAS-$Htt_{ex1}Q91$-$mCherry^{attP24}$/+ ; $drpr^{\Delta 5}$/$drpr^{\Delta 5}$*	C,D: +shi^{ts1}, *$drpr^{-/-}$ - 8*

Figure 5, figure supplement 2		
A,E,F	*Or67d-QF,UAS-Htt$_{ex1}$Q25-GFP^{attP3}/Y ; GH146-Gal4,QUAS-Htt$_{ex1}$Q91-mCherry^{attP24}/+*	E,F: control - *5*
B,E,F	*Or67d-QF,UAS-Htt$_{ex1}$Q25-GFP^{attP3}/Y ; GH146-Gal4,QUAS-Htt$_{ex1}$Q91-mCherry^{attP24}/repo-Gal80*	E,F: +repo-Gal80 - *6*
C,E,F	*Or67d-QF,UAS-Htt$_{ex1}$Q25-GFP^{attP3}/Y ; GH146-Gal4,QUAS-Htt$_{ex1}$Q91-mCherry^{attP24}/+ ; UAS-FFLuc ^{attP2}/+*	E,F: +FFLuc - *11*
D,E,F	*Or67d-QF,UAS-Htt$_{ex1}$Q25-GFP^{attP3}/Y ; GH146-Gal4,QUAS-Htt$_{ex1}$Q91-mCherry^{attP24}/+ ; UAS-Draper$^{RNAi\#5}$/+*	E,F: +Drpr^{RNAi} - *6*
Figure 5, figure supplement 3		
A1-2,C,E,F	*Or67d-QF,QUAS-Htt$_{ex1}$Q91-mCherry^{attP3}/+ ; UAS-Atg8a-GFP/+ ; repo-Gal4/+*	E,F: Atg8a - *12*
B1-2,D,E,F	*Or67d-QF,QUAS-Htt$_{ex1}$Q91-mCherry^{attP3}/+ ; UAS-GFP-Lamp1/+ ; repo-Gal4/+*	E,F: Lamp1 - *12*
E,F	*Or67d-QF,QUAS-Htt$_{ex1}$Q91-mCherry^{attP3}/+ ; UAS-mCD8-GFP/+ ; repo-Gal4/+*	E,F: mCD8 - *10*
Figure 6		
A,E	*Or83b-Gal4,UAS-Htt$_{ex1}$Q25-GFP^{attP24}/+ ; drpr$^{\Delta 5}$/+*	E: Htt$_{ex1}$Q25, *drpr $^{+/-}$* - *6*
B,E	*Or83b-Gal4,UAS-Htt$_{ex1}$Q91-GFP^{attP24}/+ ; drpr$^{\Delta 5}$/+*	E: Htt$_{ex1}$Q91, *drpr $^{+/-}$* - *7*
C,E	*Or83b-Gal4,UAS-Htt$_{ex1}$Q25-GFP^{attP24}/+ ; drpr$^{\Delta 5}$/drpr$^{\Delta 5}$*	E: Htt$_{ex1}$Q25, *drpr $^{-/-}$* - *6*
D,E	*Or83b-Gal4,UAS-Htt$_{ex1}$Q91-GFP^{attP24}/+ ; drpr$^{\Delta 5}$/drpr$^{\Delta 5}$*	E: Htt$_{ex1}$Q91, *drpr $^{-/-}$* - *8*
F,J,K	*Or67d-QF,UAS-Htt$_{ex1}$Q25-GFP^{attP3}/Y ; GH146-Gal4,QUAS-Htt$_{ex1}$Q91-mCherry^{attP24}/+ ; QUAS-nucLacZ/+*	J,K: +LacZ in ORNs - *8*
G,J,K	*Or67d-QF,UAS-Htt$_{ex1}$Q25-GFP^{attP3}/Y ; GH146-Gal4,QUAS-Htt$_{ex1}$Q91-mCherry^{attP24}/+; QUAS-p35/+*	J,K: +p35 in ORNs - *8*
H,J,K	*Or67d-QF,UAS-Htt$_{ex1}$Q25-GFP^{attP3}/Y ; GH146-Gal4,QUAS-Htt$_{ex1}$Q91-mCherry^{attP24}/UAS-LacZ*	J,K: +LacZ in PNs - *7*
I,J,K	*Or67d-QF,UAS-Htt$_{ex1}$Q25-GFP^{attP3}/Y ; GH146-Gal4,QUAS-Htt$_{ex1}$Q91-mCherry^{attP24}/UAS-p35*	J,K: +p35 in PNs - *7*
Figure 7		
B,C,D,E,F, G,I,J	*Or67d-QF,QUAS-Htt$_{ex1}$Q91-mCherry^{attP3}/+ ; GH146-LexA::GAD,LexAop-Htt$_{ex1}$Q25-YFP^{attP24}/UAS-Htt$_{ex1}$Q25-3xHA^{attP24} ; repo-Gal4/+*	I,J: control - 0d (*12*), 1d (*10*), 2d (*12*), 3d (*10*), 4d (*11*), 5d (*10*), 7d (*14*), 14d (*11*)
H,I,J	*Or67d-QF,QUAS-Htt$_{ex1}$Q91-mCherry^{attP3}/+ ; GH146-LexA::GAD,LexAop-Htt$_{ex1}$Q25-YFP^{attP24}/UAS-Htt$_{ex1}$Q25-3xHA^{attP24} ; repo-Gal4/UAS-Draper$^{RNAi\#5}$*	I,J: +Drpr^{RNAi} - 7d (*8*), 14d (*7*)
Figure 7-figure supplement 1		
A1-2	*GH146-LexA::GAD,LexAop-Htt$_{ex1}$Q25-YFP^{attP24}/UAS-Htt$_{ex1}$Q25-3xHA^{attP24} ; repo-Gal4/+*	
B1-2	*Or67d-QF/+ ; GH146-LexA::GAD,LexAop-Htt$_{ex1}$Q25-YFP^{attP24}/QUAS-Htt$_{ex1}$Q25-mCherry^{attP24}*	
C1-2	*Or67d-QF/+ ; QUAS-Htt$_{ex1}$Q25-mCherry^{attP24}/UAS-Htt$_{ex1}$Q25-3xHA^{attP24} ; repo-Gal4/+*	
Video 1		
	Or67d-QF,UAS-Htt$_{ex1}$Q25-GFP^{attP3}/(+/Y) ; GH146-Gal4,QUAS-Htt$_{ex1}$Q91-mCherry^{attP24}/+	